



**HAL**  
open science

## Three-dimensional textures of Ryugu samples and their implications for the evolution of aqueous alteration in the Ryugu parent body

Akira Tsuchiyama, Megumi Matsumoto, Junya Matsuno, Masahiro Yasutake, Tomoki Nakamura, Takaaki Noguchi, Akira Miyake, Kentaro Uesugi, Akihisa Takeuchi, Shota Okumura, et al.

### ► To cite this version:

Akira Tsuchiyama, Megumi Matsumoto, Junya Matsuno, Masahiro Yasutake, Tomoki Nakamura, et al.. Three-dimensional textures of Ryugu samples and their implications for the evolution of aqueous alteration in the Ryugu parent body. *Geochimica et Cosmochimica Acta*, 2024, 375, pp.146-172. 10.1016/j.gca.2024.03.032 . insu-04858910

**HAL Id: insu-04858910**

**<https://insu.hal.science/insu-04858910v1>**

Submitted on 2 Jan 2025

**HAL** is a multi-disciplinary open access archive for the deposit and dissemination of scientific research documents, whether they are published or not. The documents may come from teaching and research institutions in France or abroad, or from public or private research centers.

L'archive ouverte pluridisciplinaire **HAL**, est destinée au dépôt et à la diffusion de documents scientifiques de niveau recherche, publiés ou non, émanant des établissements d'enseignement et de recherche français ou étrangers, des laboratoires publics ou privés.



Distributed under a Creative Commons Attribution 4.0 International License



## Three-dimensional textures of Ryugu samples and their implications for the evolution of aqueous alteration in the Ryugu parent body

Akira Tsuchiyama<sup>a,b,c,\*</sup>, Megumi Matsumoto<sup>d</sup>, Junya Matsuno<sup>e</sup>, Masahiro Yasutake<sup>f</sup>, Tomoki Nakamura<sup>d</sup>, Takaaki Noguchi<sup>g</sup>, Akira Miyake<sup>g</sup>, Kentaro Uesugi<sup>f</sup>, Akihisa Takeuchi<sup>f</sup>, Shota Okumura<sup>g</sup>, Yuri Fujioka<sup>d</sup>, Mingqi Sun<sup>b,d,h</sup>, Aki Takigawa<sup>i</sup>, Toru Matsumoto<sup>j</sup>, Satomi Enju<sup>k</sup>, Itaru Mitsukawa<sup>g</sup>, Yuma Enokido<sup>l</sup>, Tatsuhiro Kawamoto<sup>m</sup>, Takeshi Mikouchi<sup>i</sup>, Tatsuhiro Michikami<sup>n</sup>, Tomoyo Morita<sup>d</sup>, Mizuha Kikuri<sup>d</sup>, Kana Amano<sup>d</sup>, Eiichi Kagawa<sup>d</sup>, Stefano Rubino<sup>o</sup>, Zelia Dionnet<sup>p</sup>, Alice Aléon-Toppani<sup>p</sup>, Rosario Brunetto<sup>p</sup>, Michael E. Zolensky<sup>q</sup>, Tsukasa Nakano<sup>r</sup>, Naoto Nakano<sup>s</sup>, Hisayoshi Yurimoto<sup>t</sup>, Ryuji Okazaki<sup>u</sup>, Hikaru Yabuta<sup>v</sup>, Hiroshi Naraoka<sup>u</sup>, Kanako Sakamoto<sup>l</sup>, Toru Yada<sup>l</sup>, Masahiro Nishimura<sup>l</sup>, Aiko Nakato<sup>w</sup>, Akiko Miyazaki<sup>l</sup>, Kasumi Yogata<sup>l</sup>, Masanao Abe<sup>l</sup>, Tatsuaki Okada<sup>l</sup>, Tomohiro Usui<sup>l</sup>, Makoto Yoshikawa<sup>l</sup>, Takanao Saiki<sup>l</sup>, Satoshi Tanaka<sup>l</sup>, Satoru Nakazawa<sup>l</sup>, Fuyuto Terui<sup>x</sup>, Shogo Tachibana<sup>l,y</sup>, Sei-ichiro Watanabe<sup>z</sup>, Yuichi Tsuda<sup>l</sup>, The Hayabusa2-Initial-Analysis Stone and Sand teams

<sup>a</sup> CAS Key Laboratory of Mineralogy and Metallogeny/Guangdong Provincial Key Laboratory of Mineral Physics and Materials, Guangzhou Institute of Geochemistry, Chinese Academy of Sciences, Guangzhou 510640, China

<sup>b</sup> Research Organization of Science and Technology, Ritsumeikan University, Shiga 525-8577, Japan

<sup>c</sup> CAS Center for Excellence in Deep Earth Science, Guangzhou 510640, China

<sup>d</sup> Department of Earth and Planetary Materials Sciences, Tohoku University, Miyagi 980-8578, Japan

<sup>e</sup> Department of Chemical Systems and Engineering, Graduate School of Engineering, Kyushu University, 744 Motoooka, Nishi-ku, Fukuoka, 81900395, Japan

<sup>f</sup> Research and Utilization Division, Japan Synchrotron Radiation Research Institute (JASRI/SPring-8), Hyogo 679-5198, Japan

<sup>g</sup> Division of Earth and Planetary Sciences, Kyoto University, Kyoto 606-8502, Japan

<sup>h</sup> University of Chinese Academy of Science, Beijing 1000410, China

<sup>i</sup> Graduate School of Science, The University of Tokyo, Tokyo 113-0033, Japan

<sup>j</sup> The Hakubi Center for Advanced Research, Kyoto University, Kitashirakawa-Oiwakecho, Sakyo, Kyoto 606-8502, Japan

<sup>k</sup> Earth's Evolution and Environment Course, Department of Mathematics, Physics, and Earth Science, Ehime University, Ehime 790-8577, Japan

<sup>l</sup> Institute of Space and Astronautical Science (ISAS), Japan Aerospace Exploration Agency (JAXA), Sagamihara 252-5210, Japan

<sup>m</sup> Department of Geoscience, Faculty of Science, Shizuoka University, Shizuoka 422-8529, Japan

<sup>n</sup> Faculty of Engineering, Kindai University, Higashi-Hiroshima 739-2116, Japan

<sup>o</sup> Istituto di Astrofisica e Planetologia Spaziali, Istituto Nazionale di Astrofisica, Rome, Italy

<sup>p</sup> IAS, Université Paris-Saclay, CNRS, France

<sup>q</sup> ARES, NASA Johnson Space Center, Houston, TX 77058, USA

<sup>r</sup> The Institute of Geology and Geoinformation, National Institute of Advanced Industrial Science and Technology (AIST), Tsukuba 305-8567, Japan

<sup>s</sup> Graduate School of Advanced Mathematical Sciences, Meiji University, 164-8525, Japan

<sup>t</sup> Department of Earth and Planetary Sciences, Hokkaido University, Sapporo 060-0810, Japan

<sup>u</sup> Department of Earth and Planetary Sciences, Kyushu University, Fukuoka 819-0395, Japan

<sup>v</sup> Department of Earth and Planetary Systems Science, Hiroshima University, 1-3-1 Kagamiyama, Higashi-Hiroshima, 739-8526, Japan

<sup>w</sup> National Institute of Polar Research, 10-3 Midori-cho, Tachikawa, Tokyo, 190-8581, Japan

<sup>x</sup> Kanagawa Institute of Technology, Atsugi 243-0292, Japan

<sup>y</sup> UTokyo Organization for Planetary and Space Science, Department of Earth and Planetary Science, The University of Tokyo, Tokyo 113-0033, Japan

<sup>z</sup> Department of Earth and Environmental Sciences, Nagoya University, Nagoya 464-8601, Japan

\* Corresponding author.

E-mail address: [atsuchi@fc.ritsumei.ac.jp](mailto:atsuchi@fc.ritsumei.ac.jp) (A. Tsuchiyama).

## ARTICLE INFO

Associate editor: Pierre Beck

## Keywords:

Hayabusa2

X-ray nanotomography

CI chondrites

Three-dimensional morphology of minerals

Precipitation sequence

## ABSTRACT

Samples collected from the surface/subsurface of C-type asteroid 162173 Ryugu by the Hayabusa2 mission were nondestructively analyzed in three dimensions (3D). Seventy-three small particles (approximately 10–180  $\mu\text{m}$  in size) were observed using X-ray nanotomography, with an effective spatial resolution of approximately 200 nm. Detailed descriptions of these samples in terms of mineralogy, petrology, and variations among particles were reported. The 57 most common particles consisted of a phyllosilicate matrix containing mineral grains, mainly magnetite, pyrrhotite, dolomite and apatite. The remaining particles were mostly monomineralic particles (pyrrhotite, dolomite, breunnerite, apatite, and Mg-Na phosphate) with two unique particles (calcite in a  $\text{Al}_2\text{Si}_2\text{O}_5(\text{OH})_4$  matrix, and  $\text{CaCO}_3$ , phyllosilicate, and tochilinite-chronstedtite inclusions in a carbonaceous material matrix). The results confirmed that the samples correspond to Ivuna-type carbonaceous chondrites (CI chondrites) or related materials. Many small inclusions of voids and carbonaceous materials were detected in pyrrhotite, dolomite, breunnerite, and apatite. However, no fluid inclusions were observed, except for those in pyrrhotite that have already been reported. Magnetite exhibited a wide variety of morphologies, from irregular shapes (spherulites, framboids, plaquettes, and whiskers) to euhedral shapes (equants, rods, and cubes), along with transitional shapes. In contrast, the other minerals exhibit predominantly euhedral shapes (pyrrhotite: pseudo-hexagonal plates, dolomite: flattened rhombohedrons, breunnerite: largely flattened rhombohedrons, and apatite: hexagonal prisms) or aggregates of faceted crystals, except for Mg-Na phosphate. The matrices were heterogeneous with variable phyllosilicate particle sizes, Mg/Fe ratios, density ( $1.7 \pm 0.2 \text{ g/cm}^3$ ), nanoporosity ( $36 \pm 9 \%$ ), and abundances of nanograins of Fe(-Ni) sulfides. The macroporosity of the particles was estimated as  $12 \pm 4 \%$ .

The observed textural relationships among the minerals suggest a precipitation sequence of: magnetite (spherulite  $\rightarrow$  plaquette/framboid  $\rightarrow$  rod/equant)  $\rightarrow$  pyrrhotite (pentlandite  $\rightarrow$  pyrrhotite)  $\rightarrow$  apatite  $\rightarrow$  dolomite  $\rightarrow$  breunnerite  $\rightarrow$  coarse phyllosilicates. Fe-bearing olivine (or low-Ca pyroxene) might have precipitated later than dolomite, indicating a high Mg activity in the aqueous solution. This precipitation sequence corresponds to a transition from irregular crystal forms (as seen in some magnetite) to regular forms of euhedral crystals (observed in some magnetite and other minerals). Based on the precipitation sequence and mineral morphologies, together with previously reported observations, a model for aqueous alteration in the Ryugu parent body was proposed as follows:  $\text{CO}_2\text{-H}_2\text{O}$  ice, amorphous silicates (GEMS-like material), and some minerals (mostly metal, sulfides, and anhydrous silicates) accumulated to form the parent body of Ryugu. Amorphous silicates and Fe-Ni metal quickly dissolved into the melted ice to form a highly supersaturated aqueous solution. Poorly-crystallized phyllosilicate and spherulitic magnetite precipitated first, followed by plaquette/framboidal magnetites with decreasing degree of supersaturation due to precipitation. Pseudo-hexagonal pyrrhotite plates were formed by dissolution and reprecipitation under relatively low supersaturation. Subsequently, apatite, dolomite, and breunnerite precipitated in this order in response to decreasing supersaturation.

## 1. Introduction

Samples from the C-type asteroid 162173 Ryugu were successfully returned to Earth by the Hayabusa2 mission of Japan Aerospace Exploration Agency (JAXA) (e.g., Tachibana et al., 2022). The surface samples were collected from the first touchdown site and stored in Chamber A, and the surface and subsurface samples were collected from the second touchdown site close to the crater made by the small carry-on impactor (SCI) in Chamber C (Tachibana et al., 2022). Initial analysis of the samples revealed that the Ryugu samples correspond to CI chondrites or related materials in terms of mineralogy, petrology, and chemistry (e.g., Yada et al., 2022; Yokoyama et al., 2022; Nakamura et al., 2022; Ito et al., 2022; Nakato et al., 2022; Nakamura et al., 2023; Noguchi et al., 2023a), contain organic materials (e.g., Nakamura et al., 2022; Naraoka et al., 2023; Yabuta et al., 2023), and have the evidence of space weathering (e.g., Okazaki et al., 2023; Noguchi et al., 2023a). The formation and evolutionary processes of Ryugu and its parent body have been proposed based on chronology, aqueous alteration conditions, redox conditions, and dehydration state (e.g., Yokoyama et al., 2022; Nakamura et al., 2023). Fluid inclusions rich in  $\text{CO}_2$  discovered in pyrrhotite crystals indicate that the Ryugu parent body formed in the outer area of the primitive solar system beyond the orbit of Jupiter (Nakamura et al., 2023), consistent with the recent dynamic formation model of the solar system (e.g., Levison et al., 2009; Walsh et al., 2012a; Walsh et al., 2012b). The stable isotopic composition of Ryugu samples is also consistent with the location of Ryugu's formation (e.g., Yokoyama et al., 2022; Ito et al., 2022) based on the dichotomy or trichotomy of the isotopic composition of extraterrestrial materials (e.g., Warren, 2011; Kruijer et al., 2017; Marrocchi et al., 2023).

In contrast to the similarities between the Ryugu samples and CI

chondrites, several features differ from those of CI chondrites: Ryugu samples exhibit Mg-rich phyllosilicates, unlike those in the CIs (Nakamura et al., 2023; Noguchi et al., 2023b); they contain Fe(-Ni) sulfide nanograins in the matrix instead of ferrihydrite found in the CIs (Nakamura et al., 2023; Noguchi et al., 2023b; Matsumoto et al., 2024); they lack corroded pyrrhotite and sulfates such as gypsum, epsomite, and bloedite (e.g., Nakamura et al., 2023); they lack water but contain organics within the interlayer space of saponite (Yokoyama et al., 2022; Viennet et al., 2023); and they have lower water content than the CIs (Yokoyama et al., 2022). These differences were attributed to terrestrial weathering of CI chondrites, involving oxidation of Fe(-Ni) sulfides and ferric saponite by reaction with  $\text{H}_2\text{O}$  in liquid and/or vapor state and oxygen in the atmosphere and addition of terrestrial water to saponite. Some of these processes were previously proposed by Zolensky et al. (1993) and Gounelle and Zolensky (2001).

Non-destructive analysis of the samples in three-dimensions (3D) has been performed using X-ray nanotomography (XnCT) as a part of the Hayabusa2 initial analysis by “Stone” and “Sand” teams, and only limited results of the XnCT have been reported previously (Nakamura et al., 2023; Noguchi et al., 2023a,b). In this paper, comprehensive results of the XnCT analysis of Ryugu grains with detailed mineralogical and petrological discussions are reported.

In the XnCT analysis, 3D distributions of minerals, carbonaceous materials, and voids (3D texture) of small Ryugu particles ( $< \sim 200 \mu\text{m}$  in size) were obtained with high spatial resolution ( $\sim 200 \text{ nm}$ ) by applying a combined method of dual-energy tomography (DET) – scanning-imaging X-ray microscopy (SIXM) (e.g., Matsumoto et al., 2019, 2022). Some physical properties, such as 3D particle size and shape information, surface features, crack features, porosity, and density, were also obtained. In addition, detailed information regarding inclusions in

3D and the textural relationships between two or more phases can be examined. In this method, however, only small particles can be examined because low X-ray energies (7 to 8 keV) are used in the DET-SIXM method, where X-rays cannot pass through particles larger than ~ 200  $\mu\text{m}$  in size. Nevertheless, such 3D textural data contain information that is generally comparable to two-dimensional (2D) data obtained from a larger area, such as secondary electron microscope (SEM) observations (Supplementary Material, S1). Furthermore, if a large number of particles are picked up randomly, we can examine a variety of Ryugu particles, although a large volume cannot be observed using XnCT. Inclusions and small particles surrounded by large crystal grains are important for estimating the precipitation order of different mineral phases, and 3D observations are more effective than 2D observations. Another advantage of XnCT is its non-destructive nature, which enables the combination of different nondestructive methods such as Fourier transform infrared (FTIR) (e.g., Dionnet et al., 2020; 2023) and X-ray fluorescence (XRF) analyses (Nakamura et al., 2023), and later destructive analysis based on computed tomography (CT) results, such as transmission electron microscopy (TEM) and time-of-flight secondary mass spectroscopy (TOF-SIMS), where fluid inclusions were confirmed and characterized (Nakamura et al., 2023).

In this paper, detailed descriptions of 73 particles in 3D are presented in terms of mineralogy (e.g., crystal morphologies, chemical compositions, and inclusions), petrology (e.g., mineral assemblages and their textural relations, specific objects, and matrix features), and variation among particles (e.g., differences in lithology and unique particles). Based on these results, we examined the precipitation sequence and mineral morphologies, and discussed the details of the aqueous alteration processes in the Ryugu parent body.

## 2. Materials and methods

### 2.1. Samples

Seventy-three particles (10 ~ 180  $\mu\text{m}$  in apparent size) listed in Table 1 were examined in this study. The first letters of the sample names A and C correspond to the samples picked up from Chambers A ( $N = 39$ ) and C ( $N = 34$ ), respectively. They are (1) fine particles picked up from fine-grained aggregates in A0104 and C0105 dishes allocated to the Sand team (A0104-00000100 to -00002100 and C0105-04300100 to -04300900:  $N = 30$ ) and in C0103 dish to the Stone team (sample name stating with “FG”:  $N = 5$ ); (2) fine particles (<~200  $\mu\text{m}$ ) coexisting with coarse particles (>~1 mm) of A0064, C0046, and C0076 to Stone team (“FO”:  $N = 8$ ); (3) sub-particles removed from coarse particles of A0063, A0067, C0002, C0061, C0076, and C0103 to the Stone team (“FC”:  $N = 20$ ); and (4) box-shaped samples extracted from regions of interest (ROIs) of coarser particles using a focused ion beam (FIB) based on scanning electron microscope (SEM) observations ( $N = 10$ ). The particles in categories (1)–(3) were randomly picked up, except for some particles that were mainly composed of a single mineral. Their weights were too small to be measured.

These samples were categorized as typical particles with an abundant matrix ( $N = 57$ ), mostly monomineralic particles (pyrrhotite,  $N = 5$ ; carbonates,  $N = 6$ ; phosphates,  $N = 3$ ), and unique particles with mineralogical features distinct from those of typical particles ( $N = 2$ ). Four particles were examined by FTIR (Dionnet et al., 2023) prior to XnCT and some particles were examined by TEM (Matsumoto et al., 2024), TOF-SIMS (Nakamura et al., 2023), and XRF (Nakamura et al., 2023) after XnCT.

### 2.2. X-ray nanotomography (XnCT)

The samples were imaged using two different methods: dual-energy tomography (DET) (Tsuchiyama et al., 2011; Tsuchiyama et al., 2013) and scanning-imaging X-ray microscopy (SIXM) (Takeuchi et al., 2013) at the beamline BL47XU of SPring-8, a synchrotron facility in Japan

(Matsumoto et al., 2019). In DET, X-ray absorption contrast images were obtained as the spatial distribution of the linear attenuation coefficient (LAC) at X-ray energies of 7 and 7.35 keV, which are below and above the K-absorption edge energy of Fe (7.11 keV), respectively. The LAC images at 7 keV roughly correspond to the mean atomic number ( $Z$ ) contrasts, except for Fe (Fig. 1A), and those at 7.35 keV strongly depend on the Fe content (Fig. 1B). In SIXM, we obtained X-ray differential phase contrast images as the spatial distribution of the refractive index decrement (RID), which is the difference between the X-ray refractive index (RI) and unity ( $\text{RID} = 1 - \text{RI}$ ), at an X-ray energy of 8 keV. The RID image contrast is closely proportional to the density of the material (Fig. 1C). The density can be estimated from an empirical equation between the RID value,  $\delta$ , and the density,  $\rho$ , at 8 keV, which was determined for many simple substances and compounds (Supplementary Material, S2 and Fig. S1);

$$\delta [\times 10^{-6}] = 3.72 \times \rho [g/cm^3]^{0.871} \quad (1)$$

The voxel sizes are  $47.4 \times 47.4 \times 47.4$  or  $47.17 \times 47.17 \times 47.17 \text{ nm}^3$  for LAC 7 keV images,  $49.44 \times 49.44 \times 49.44$  or  $51.1 \times 51.1 \times 51.1 \text{ nm}^3$  for LAC 7.35 keV images, and  $111.1 \times 111.1 \times 108.1 \text{ nm}^3$  or  $111.1 \times 111.1 \times 109.2 \text{ nm}^3$  for RID images (the size of 148.08, 222.12, 308.5, or 555.3 nm was used instead of 111.1 nm for some large samples). The number of projections was 1800 at a  $180^\circ$  rotation for DET (offset CT was used for some large samples: 1800 in  $360^\circ$  rotations) and 180–450 projections/ $180^\circ$  rotation for SIXM. It took approximately 1 h for the two energies to be obtained by DET, and 1–2 h for SIXM. The CT images were reconstructed from the projection images using the back-projection method. Some of the Fe-rich samples mainly composed of pyrrhotite were imaged only at 7 keV with absorption contrasts (“ACT” in Table 1) because we could not obtain sufficient X-ray transmission above the Fe K-absorption energy (7.35 and 8 keV).

As the LAC and RID values obtained by reconstruction,  $\mu_{CT}$  and  $\delta_{CT}$ , respectively, are slightly smaller than the real value,  $\mu$  and  $\delta$ , respectively, we provide the correction factors of  $\gamma_\mu$  and  $\gamma_\delta$  as follows (Matsumoto et al., 2019)

$$\mu_{CT} = \gamma_\mu \times \mu \quad (2)$$

and

$$\delta_{CT} = \gamma_\delta \times \delta \quad (3)$$

We corrected the LAC and RID values using  $\gamma_\mu = 0.949$  for LAC 7 keV images,  $\gamma_\mu = 0.976$  for LAC 7.35 keV images, and  $\gamma_\delta = 0.873$  for RID images, and using  $\gamma_\mu = 0.964$  for LAC 7 keV images,  $\gamma_\mu = 0.977$  for LAC 7.35 keV images, and  $\gamma_\delta = 0.911$  for RID images, as obtained by calibration using standard materials in two different beamtimes of the imaging experiments, respectively.

For samples with specific ROIs based on the DET images, we performed ultra-high-resolution tomography, where only the ROIs were imaged by the absorption tomography at 7.35 keV with the voxel sizes of  $14.79 \times 14.79 \times 14.79$  or  $17.7 \times 17.7 \times 17.7 \text{ nm}^3$  as a local tomography (“LCT” in Table 1) to observe detailed textures of the ROIs in 3D with the higher resolution.

All samples were transferred using nitrogen-filled containers. CT imaging was performed in air, but exposure to air was minimized as much as possible.

### 2.3. SEM and FIB

The surfaces of coarse particles were observed using field-emission scanning electron microscopies (FE-SEMs) (Hitachi SU6600 at JAXA curation facility and JEOL JSM-7001F at Tohoku University). ROIs were selected based on SEM observations, and box-shaped blocks (10 ~ 25  $\mu\text{m}$  cubes) (A0067-CT001, A0067-CT003, and A0094-FIB001) were extracted from the ROIs by focused FIB using a  $\text{Ga}^+$  ion beam at 30 kV

**Table 1**

The list of Ryugu particles examined in the present study with their size, matrix density and nanoporosity.

sample name	category	shape	sample holder *	Imaging method **	further analysis ***	sphere equivalent diameter [ $\mu\text{m}$ ]	matrix density ( $\text{g}/\text{cm}^3$ )	nano porosity (vol/%)	remarks****
A0063-FC005	matrix	particle	Ti	DET, SIXM		62.3	1.38	47.6	
A0063-FC006	matrix	particle	Ti	DET, SIXM, LCT		68.4	1.90	27.7	
A0063-FC007	matrix	particle	Ti	DET, SIXM		43.8	1.81	31.3	
A0063-FC010	matrix	particle	Ti	DET, SIXM		102.7	1.51	42.7	
A0064-FO022	matrix	particle	W	DET, SIXM	IR	11.8	1.85	29.7	
A0064-FO023	matrix	particle	W	DET, SIXM	IR	12.0	1.42	45.9	
A0064-FO024	matrix	particle	Al	DET, SIXM	IR	34.9	1.48	43.7	
A0067-FC003	breunnerite	particle	C	DET, SIXM	Raman	n.d.	n.d.	n.d.	
A0067-FC004	breunnerite	particle	C	DET, SIXM	Raman	n.d.	n.d.	n.d.	
A0067-FC005	matrix	particle	C	DET, SIXM	XRF	31.2	1.40	46.9	
A0067-FC007	matrix	particle	C	DET, SIXM		47.8	1.34	49.0	c-PS layer ( $1.90 \text{ g}/\text{cm}^3$ )
A0067-CT003	matrix	box	Ti	DET, SIXM, LCT	TEM	11.2	1.38	47.5	
A0067-FIB006	matrix	box	Ti	DET, SIXM, LCT		17.9	1.41	46.5	
A0067-FIB005	matrix	box	Ti	DET, SIXM, LCT		26.9	1.60	39.3	c-PS layer ( $2.06 \text{ g}/\text{cm}^3$ ), glass ( $2.38 \text{ g}/\text{cm}^3$ )
A0067-CT001	matrix	box	Ti	DET, SIXM, LCT	TEM	36.5	1.48	43.6	glass ( $2.08 \text{ g}/\text{cm}^3$ )
A0094-FIB001	matrix	box	Ti	DET, SIXM, LCT	TEM	19.7	1.32	49.7	
A0094-FIB002	matrix	box	Ti	DET, SIXM		22.0	1.45	44.8	
A0067-CT002	matrix	box	Ti	DET, SIXM, LCT		n.d.	1.38	47.7	
A0104-00000100	matrix	particle	Ti	DET, SIXM, LCT		13.4	1.85	29.5	
A0104-00000200	matrix	particle	Ti	DET, SIXM		18.5	1.88	28.4	
A0104-00000300	matrix	particle	Ti	DET, SIXM		17.6	1.54	41.3	
A0104-00000400	matrix	particle	Ti	DET, SIXM		12.5	1.84	29.9	2nd peak
A0104-00000500	matrix	particle	Ti	DET, SIXM		18.9	1.77	32.8	
A0104-00000600	matrix	particle	Ti	DET, SIXM		14.3	1.88	28.5	
A0104-00000700	matrix	particle	Ti	DET, SIXM, LCT		12.6	2.07	21.5	
A0104-00000800	matrix	particle	Ti	DET, SIXM		11.9	1.93	26.8	
A0104-00000900	pyrrhotite	particle	Ti	DET, SIXM		n.d.	2.03	22.9	
A0104-00001000	matrix	particle	Ti	DET, SIXM		16.2	n.d.	n.d.	
A0104-00001100	matrix	particle	Ti	DET, SIXM, LCT		16.4	1.95	25.9	
A0104-00001200	matrix	particle	Ti	DET, SIXM		17.0	1.67	36.5	
A0104-00001300	matrix	particle	Ti	DET, SIXM		9.0	1.68	36.2	
A0104-00001400	matrix	particle	Ti	DET, SIXM, LCT		15.9	1.96	25.6	
A0104-00001500	unique	particle	Ti	DET, SIXM		n.d.	1.87	29.0	
A0104-00001600	dolomite	particle	Ti	DET, SIXM		n.d.	n.d.	n.d.	
A0104-00001700	matrix	particle	Ti	DET, SIXM		21.1	1.94	26.2	
A0104-00001800	matrix	particle	Ti	DET, SIXM		13.2	1.98	24.8	
A0104-00001900	matrix	particle	Ti	DET, SIXM		18.1	1.90	27.9	
A0104-00002000	matrix	particle	Ti	DET, SIXM		16.9	1.69	35.7	
A0104-00002100	matrix	particle	Ti	DET, SIXM		20.7	1.68	36.0	
C0002-FC001	breunnerite	particle	C	DET, SIXM		n.d.	n.d.	n.d.	
C0002-FC005	breunnerite	particle	C	DET, SIXM		n.d.	n.d.	n.d.	

(continued on next page)

Table 1 (continued)

sample name	category	shape	sample holder *	Imaging method **	further analysis ***	sphere equivalent diameter [μm]	matrix density (g/cm <sup>3</sup> )	nano porosity (vol/%)	remarks****
C0002-FC008	matrix	particle	Ti	DET		n.d.	n.d.	n.d.	
C0002-FC009_CT001	matrix	particle	Ti	DET, SIXM		39.2	2.06	21.5	
C0002-FC012	pyrrhotite	particle	Ti	ACT	TOF-SIMS	n.d.	n.d.	n.d.	
C0023-FC003	matrix	particle	C	DET, SIXM		25.7	1.71	35.1	
C0046-FO015	matrix	particle	Al	DET, SIXM, LCT	IR	48.9	1.58	39.9	
C0046-FO018	Mg-Na phosphate	particle	C	DET, SIXM		n.d.	n.d.	n.d.	Mg-Na phosphate (1.30 g/cm <sup>3</sup> )
C0046-FO019	pyrrhotite	particle	C			n.d.	n.d.	n.d.	
C0061-FC005	matrix	particle	C	DET, SIXM		27.0	1.27	51.8	
C0076-FC001	unique	particle	C	DET, SIXM, LCT		n.d.	n.d.	n.d.	tabular carbonaceous material (1.24 g/cm <sup>3</sup> ), matrix carbonaceous material (1.07 g/cm <sup>3</sup> )
C0076-FC004	matrix	particle	Al	SIXM		n.d.	1.52	42.2	
C0076-FC005	matrix	particle	Al	DET, SIXM		19.8	1.80	31.4	
C0076-FO006	dolomite	particle	C	DET, SIXM		53.8	n.d.	n.d.	
C0076-02-CT003	apatite	box	Ti	DET, SIXM		n.d.	n.d.	n.d.	apatite (3.07 g/cm <sup>3</sup> )
C0076-02-CT001	apatite	box	C	DET, SIXM		n.d.	n.d.	n.d.	apatite (3.09 g/cm <sup>3</sup> )
C0076-02-CT002	matrix	box	Ti	DET, SIXM, LCT		n.d.	1.56	40.5	chondrule relict (1.79 g/cm <sup>3</sup> )
C0103-FC003	matrix	particle	Ti	DET, SIXM		87.1	1.50	43.1	
C0103-FC005	matrix	particle	Ti	DET, SIXM		73.9	1.51	42.6	
C0103-FC007	matrix	particle	Ti	DET, SIXM, LCT		69.5	1.40	46.9	
C0107-FG014	pyrrhotite	particle	C	ACT		n.d.	n.d.	n.d.	
C0107-FG015	matrix	particle	C	DET, SIXM		60.7	1.86	29.2	
C0107-FG015b	matrix	particle	C			12.3	n.d.	n.d.	sub-particle from C0107-FG015
C0107-FG018	matrix	particle	C	DET, SIXM		16.9	2.09	20.3	
C0107-FG020	pyrrhotite	particle	C	ACT		n.d.	n.d.	n.d.	
C0105-04300100	matrix	particle	Ti	DET, SIXM, LCT		41.1	1.65	37.2	
C0105-04300200	matrix	particle	Ti	DET, SIXM		33.9	1.44	45.1	
C0105-04300300	matrix	particle	Ti	DET, SIXM		42.4	2.11	19.7	
C0105-04300400	matrix	particle	Ti	DET, SIXM, LCT		50.0	1.64	37.5	
C0105-04300500	matrix	particle	Ti	DET, SIXM		50.7	1.79	31.7	
C0105-04300600	matrix	particle	Ti	DET, SIXM		48.3	1.87	28.9	
C0105-04300700	matrix	particle	Ti/C	DET, SIXM		38.8	1.44	45.1	
C0105-04300800	matrix	particle	Ti	DET, SIXM		38.3	1.57	40.1	
C0105-04300900	matrix	particle	Ti	DET, SIXM, LCT		36.0	1.48	43.6	
Whole samples									
N						54	56	56	
Average						32.4	1.68	36.1	
Std						21.4	0.23	8.9	
Min						9.0	1.27	19.7	
Max						102.7	2.11	51.8	
Chamber A									
N						33	35	35	
Average						25.3	1.69	35.7	
Std						20.0	0.23	8.9	
Min						9.0	1.32	21.5	
Max						102.7	2.07	49.7	
Chamber C									

(continued on next page)

Table 1 (continued)

sample name	category	shape	sample holder *	imaging method **	further analysis ***	sphere equivalent diameter [μm]	matrix density (g/cm <sup>3</sup> )	nano porosity (vol/%)	remarks ****
N						21	21	21	
Average						43.6	1.66	36.8	
Std						18.9	0.24	9.0	
Min						12.3	1.27	19.7	
Max						87.1	2.11	51.8	

\*Sample holder: Ti; titanium needle, Al; aluminum needle, W; tungsten needle; C; amorphous carbon fiber.

\*\* DET: dual-energy tomography at 7 and 7.35 keV, SIXM: scanning-imaging X-ray tomography at 8 keV, AET: absorption tomography at 7 keV, LCT: ultra-high-resolution local tomography at 7.35 keV.

\*\*\* IR: Dionnet et al. (2023), Raman: this paper, XRF: Nakamura et al. (2023), TEM: Matsumoto et al. (2024), TOF-SIMS: Nakamura et al. (2023).

\*\*\*\* c-PS layer beneath the particle surface, glass: melt splash on the surface by impact (density calculated from the RID value is shown in the parentheses).

n.d.: not determined.

(Thermo Fisher Scientific Helios NanoLab G3 at Kyoto University and Thermo Fisher Scientific Versa3D and Quanta3D at Tohoku University). Details of the FIB sampling conditions are described by Matsumoto et al. (2024).

The particle samples and the box samples were attached on the tip of a cuspidate Ti or Al needle (0.5 or 0.44 mm in diameter, respectively) with Pt deposition by FIB at Kyoto or Tohoku University. Samples with the IR measurements were attached on Al or W needles (0.44 or 0.5 mm in diameter, respectively) with Pt deposition by the FIB at Paris-Saclay University (FEI ThermoFisher Helios Nanolab 660 SEM-FIB) or Lille University (FEI Strata DB 235 SEM-FIB microscope) (Dionnet et al., 2023). Some of the particles were attached to a C fiber (~5 μm in diameter) using a small amount of glue (glycol phthalate).

Some particles and box-shaped samples were sliced into electron-transparent sections for TEM analysis using FIB after XnCT imaging (Matsumoto et al., 2024). The sliced pieces were mounted on TEM grids and thinned to 100–200 nm using a Ga<sup>+</sup> ion beam at 30 kV. The damaged layers formed on the ultrathin sections were removed using a Ga<sup>+</sup> ion beam at 2 kV.

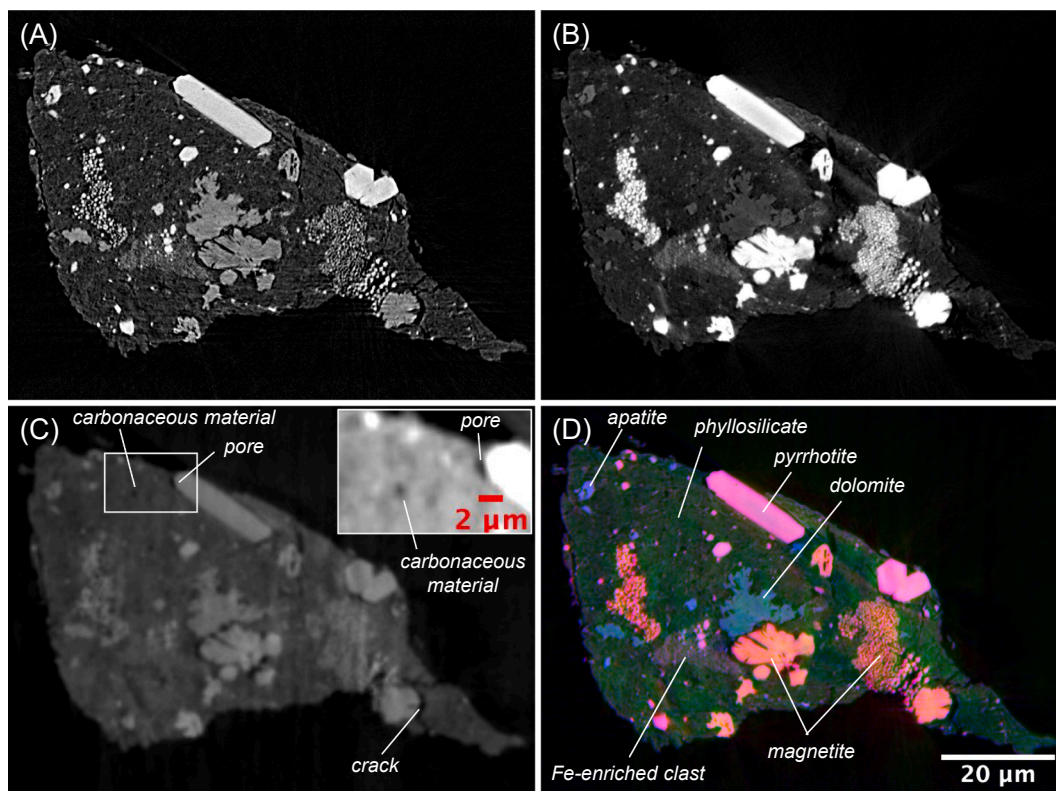
#### 2.4. TEM

Ultrathin sections were analyzed using a field-emission transmission electron microscope (JEOL JEM 2100F at Kyoto University and Tohoku University) with an energy-dispersive X-ray spectrometer (JEOL JED-2300 T) operated at 200 kV. TEM images were recorded using a charge-coupled device (CCD) camera (Gatan, Orius 200D) and analyzed using the Gatan Digital Micrograph software package. Crystal structure identification was based on selected area electron diffraction (SAED) patterns, which were analyzed using the software package ReciPro (Seto and Ohtsuka, 2022). We also acquired annular dark-field scanning transmission electron microscope (ADF-STEM) images and X-ray elemental maps using an STEM-energy dispersive spectroscopy (EDS) system. The details are described in Matsumoto et al. (2024).

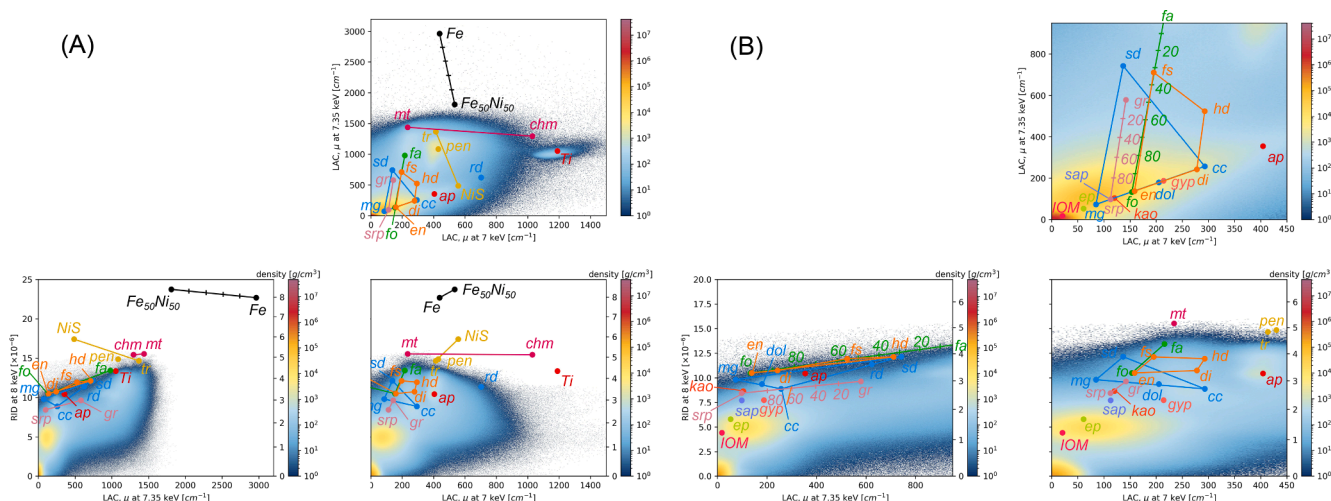
#### 2.5. Image processing and analysis

Image analysis was performed by combining ImageJ and the codes created using C (Nakano et al., 2006) and Python. For phase discrimination and analysis, we first registered the LAC 7 keV, LAC 7.35 keV, and RID images by Fijiyama in ImageJ (Fernandez and Moisy, 2020) using LAC 7 keV images as the reference image. Subsequently, combined red, green, and blue CT (RGB-CT) images were created by merging the LAC 7 keV (0–450 cm<sup>-1</sup>), LAC 7.35 keV (0–950 cm<sup>-1</sup>), and RID (0–20 × 10<sup>-6</sup>) images as blue, red, and green, respectively (Fig. 1D). Different phases, including carbonaceous materials, exhibit different colors in the RGB-CT images.

Phase discrimination was performed using histograms of corrected LAC 7 keV, LAC 7.35 keV, and RID values of the sample (e.g., Fig. 2) by comparing a histogram peak with those of known phases (e.g., magnetite, pyrrhotite, and the Ti needle are shown in Fig. 2A and phyllosilicate in matrix, apatite, and air (Fig. 2B)). Because the correction of the LAC and RID values using Eqs. (2) and (3) are not perfect, particularly for larger LAC and RID values, there is a slight discrepancy between the reconstructed and real values, but this does not affect phase discrimination. The LACs and RID values of the solid solution endmembers of a mineral can be used to constrain the element ratios, e.g., Mg# [Mg/(Mg + Fe) in moles] of serpentine [Mg<sub>3</sub>Si<sub>2</sub>O<sub>5</sub>(OH)<sub>4</sub> – Fe<sub>3</sub>Si<sub>2</sub>O<sub>5</sub>(OH)<sub>4</sub>] and olivine [Mg<sub>2</sub>SiO<sub>4</sub> – Fe<sub>2</sub>SiO<sub>4</sub>], as shown in Fig. 2B. We can extract the LAC and RID values of an object in the RCB-CT images to determine its phase and estimate its chemical composition using the LACs - RID histograms (Supplementary Material, S3 and Fig. S3). However, even with 3D histograms, some minerals exhibit overlapping LAC and RID values (e.g., Mg-serpentine and Mg-saponite, or forsterite and enstatite). In such cases, it is not possible to distinguish between these minerals using the present method. If necessary, the sample must be cut after CT imaging



**Fig. 1.** X-ray CT images of Ryugu sample (C0103-FC007) using different methods. (A) Absorption contrast image at 7 keV roughly corresponding to the mean atomic number (Z) contrast, except for Fe (LAC: 0–450 cm<sup>-1</sup>). (B) Absorption contrast image at 7.35 keV strongly proportional to the Fe content (LAC: 0–950 cm<sup>-1</sup>). (C) X-ray differential phase contrast images at 8 keV closely proportional to the density of the material (RID: 0–20 × 10<sup>-6</sup>). (D) Combined RGB-CT images obtained by merging the LAC 7 keV (0–450 cm<sup>-1</sup>), LAC 7.35 keV (0–950 cm<sup>-1</sup>), and RID (0–20 × 10<sup>-6</sup>) images as blue, red, and green, respectively. Many phases can be recognized using different colors. The figure inserted in the upper right corner of (C) is a magnified view of the area boxed in white. The contrast is enhanced to facilitate the distinguish the pore and what appears to be carbonaceous material (possibly insoluble organic matter).



**Fig. 2.** 3D histograms of the LAC 7 keV, LAC 7.35 keV, and RID values (sample: C0103-FC007) (A) over a wide range (LAC 7 keV: 0–1500 cm<sup>-1</sup>, LAC 7.35 keV: 0–3200 cm<sup>-1</sup>, and RID: 0–25 × 10<sup>-6</sup>) and (B) over a narrow range (LAC 7 keV: 0–450 cm<sup>-1</sup>, LAC 7.35 keV: 0–950 cm<sup>-1</sup>, and RID: 0–15 × 10<sup>-6</sup>). Each 3D histogram is expressed as a set of three 2D histograms: LAC 7 keV vs. LAC 7.35 keV (upper right), LAC 7 keV vs. RID (lower right), and LAC 7.35 keV vs. RID (lower left). The density calculated from the RID using Eq.(1) is shown in the LAC 7 keV vs. RID and LAC 7.35 keV vs. RID diagrams. The LAC and RID values of different minerals are plotted in the 2D histograms; *srp*: Mg-serpentine, *gr*: greenalite (Fe-serpentine), *sap*: saponite, *fo*: forsterite, *fa*: fayalite, *en*: enstatite, *fs*: ferrosilite, *di*: diopside, *hd*: hedenbergite, *mg*: magnesite, *cc*: calcite, *sd*: siderite, *dol*: dolomite, *rd*: rhodochrosite, *ap*: apatite, *mt*: magnetite, *chm*: chromite, *tr*: troilite, *pen*: pentlandite, *Ti*: Ti alloy (needle used as a sample holder), *IOM*: insoluble organic matter, *ep*: epsomite, and *kao*: kaolinite. There is a slight discrepancy between the reconstructed and real values of LAC and RID, particularly for larger values due to imperfect correction of the LAC and RID values, but this did not affect the phase discrimination. Because a Ti needle was not imaged by SIXM for RID images, the Ti peak was not observed in the histograms of LAC 7 keV vs. RID and LAC 7.35 keV vs. RID in (A).

for phase identification by SEM or TEM. In addition, we obtained the distributions of specific phases (phase maps) of Fe(-Ni) sulfides (pyrrhotite and pentlandite), magnetite, dolomite, and apatite by thresholding the LAC 7 keV, LAC 7.35 keV, and RID values of these phases, and their modes (volume fractions) were calculated (Table 2) although they were underestimated (Supplementary Material, S4).

The solid portion of the sample particle images was extracted from the LAC 7.35 keV image using the Chan-Vese segmentation method by considering active contours without edges (Chan and Vese, 2001), which is more optimal for extracting a particle with different minerals of different LAC values on the surface than segmentation by binarization. Then, shape characteristics such as volume, surface area, and 3-axial lengths were obtained. The porosities and densities estimated from the average RID values of the particles using Eq. (1) were also obtained. These data will be presented in a different paper. Only the sphere-equivalent diameters calculated from the volume and temporary porosity values used to calculate the mineral volume fractions are listed in Table 1.

### 3. Results

#### 3.1. Petrologic features of samples belonging to the “matrix” category

RGB-CT images (Fig. 1D) showed that typical sample particles (category “matrix” in Table 1) were mainly composed of Mg-rich phyllosilicates (dark to relatively bright green in Fig. 1D) as a matrix embedded with grains of Fe(-Ni) sulfides (pink or white-pink), magnetite (orange), dolomite (grayish-blue-green), and apatite (purple-blue) as the major phases. The mineral modes determined in this study are listed in Table 2. Breunnerite, CaCO<sub>3</sub> (calcite), Mg-Na phosphate, olivine (or low-Ca pyroxene), and carbonaceous materials were also recognized.

The RGB-CT images of the representative sample particles are shown in Fig. 3. We observed heterogeneities among sample particles with different mineral modes (Table 2) and matrix properties; the matrix of some particles was dark green (e.g., Fig. 3A and H), whereas some were bright green (e.g., Fig. 3E and G). The matrix of some small particles did not exhibit distinct heterogeneity (e.g., Fig. 3G and H), whereas relatively large particles showed heterogeneity with a spatial resolution of <~30 μm (Fig. 3A, B, D, E, and F). Larger-scale heterogeneity beyond the present particle size (up to >~1 mm) has also been observed (Nakamura et al., 2023).

The mean density of the matrix was estimated from the mean RID values of each sample by using Eq.(1) (Table 1) (Supplementary Material, S2). This density counts not only phyllosilicates but also nanopores, nanoparticles of carbonaceous materials, and Fe(-Ni) sulfide nanoparticles in the matrix below the spatial resolution of the RID images (a few hundred nm), as described later. The presence of organics trapped within the interlayer space of saponite layers (Viennet et al., 2023) may also affect the porosity. The density varies from 1.27 to 2.11 g/cm<sup>3</sup> (average: 1.68 ± 0.23 g/cm<sup>3</sup>) (Fig. S2), reflecting the heterogeneity of the matrix. The matrix density appears to have a bimodal distribution at ~1.5 and 1.9 g/cm<sup>3</sup>. The average matrix density is slightly smaller than the average bulk density of Ryugu particles of 1.79 ± 0.08 g/cm<sup>3</sup> (Nakamura et al., 2023) and 1.79 ± 0.31 g/cm<sup>3</sup> (Miyazaki et al., 2023), consistent with other mineral grains having larger densities than the matrix.

The nanoporosity of the matrix was roughly estimated by assuming that the solid portion of the matrix is only composed of serpentine with an average Mg# of 0.85 (Nakamura et al., 2023). Here, we adopted a density of 2.63 g/cm<sup>3</sup>, which was calculated from the densities of the Mg-end serpentine and Fe-end greenalite. The estimated porosity varies from 19.7 to 51.8 % (average: 36.1 ± 8.9 %) (Table 2). It should be noted that these values have some ambiguity because the matrix is composed not only of serpentine but also saponite as mentioned below and the Mg# of the phyllosilicate has a range roughly from 0.7 to 0.95

(Nakamura et al., 2023) corresponding to a density from 2.71 to 2.58 g/cm<sup>3</sup>. We also note that the nanoporosities were somewhat underestimated because Fe(-Ni) sulfide nanograins intimately mixed with phyllosilicates (Noguchi et al., 2023b; Matsumoto et al., 2024) were not considered. The estimated matrix densities for the individual samples are shown in Fig. 3. Generally, the bright-green matrix has a higher density than the dark-green matrix, indicating that the latter is more porous than the former, although the low-porosity matrix may have a higher Mg#.

#### 3.2. Mineralogy

##### 3.2.1. Mg-rich phyllosilicates (dark to relatively bright green in RGB-CT images)

These are the most abundant phases (mode:82.0 (56.5 ~ 92.9) vol. %; Table 2) and consist of serpentine, saponite, and mixed layer phases discriminated by TEM (e.g., Nakamura et al., 2023; Noguchi et al., 2023b; Matsumoto et al., 2024), but we could not distinguish between them using the DET-SIMX method because of their overlapping LAC and RID values (Fig. 2B). The LACs - RID histogram peaks suggest that the matrix is a mixture of Mg-rich phyllosilicates, voids, and carbonaceous material (as represented by IOM in Fig. 2B), and the mean Mg# of the phyllosilicates is roughly 0.8 ~ 0.9 (Fig. 2B), which is consistent with the mean Mg# (~0.85) obtained using TEM (e.g., Nakamura et al., 2023; Noguchi et al., 2023b). The Mg#s of the matrix measured by electron probe microanalyzer (EPMA) (e.g., ~0.63 to ~0.85; Nakato et al., 2022) are generally smaller than the mean Mg# of the phyllosilicates because the matrix measured by EPMA included many micron-sized grains of Fe(-Ni) sulfides, whereas the matrix measured by XnCT contained only nano-sized grains.

Two types of matrices that were mainly composed of relatively low-density materials (dark green) (e.g., a in Fig. 4A, f in Fig. 4C, and a in Fig. S4A: Supplementary Material, S5) and relatively high-density materials (bright green) (e.g., b in Fig. 4A, Fig. 4B, and g in Fig. 4C) were also recognized on a smaller scale. Very-fine pink grains corresponding to nanograins of Fe(-Ni) sulfides observed by TEM (e.g., Nakamura et al., 2023; Noguchi et al., 2023b; Matsumoto et al., 2024) were heterogeneously distributed in the matrix. Some regions in the dark green matrix were abundant in these grains (e.g., a in Fig. 4A, f in Fig. 4C, and a in Fig. S4A), but some were not. Some of the bright green areas are composed of aggregates of coarse fibrous phyllosilicates (b in Fig. 3B and g in Fig. 4C), and some have concentric structures with dark cores (c in Fig. 4A). Such aggregates were also present beneath the surfaces of the sample particles (c in Fig. S4B) and were identified as a saponite-rich layer (Nakamura et al., 2023) using TEM (Matsumoto et al., 2024). Occasionally, phyllosilicates exhibit specific objects without Fe(-Ni) sulfide nanograins (≥5 μm). These were high-density (bright green) subhedral objects (h in Fig. 4C), relatively high-density (relatively bright green) subhedral objects with concentric structures (d in Fig. S4C), spherical objects surrounded by pyrrhotite crystals (and sometimes dolomite) (b in Fig. S4A and Fig. 7A), and low-density (dark-green) objects with tube-shaped high-density inclusions (bright green) (e in Fig. S4D). Subhedral-shaped objects are likely pseudomorphs of phyllosilicates after olivine or low-Ca pyroxene with different Mg# values. For example, the TEM images of the high-density subhedral object (h in Fig. 4C) show an olivine pseudomorph replaced by relatively coarse serpentine (lizardite) (Supplementary Material, S6 and Fig. S5). Aggregates of fine dolomite grains were observed in the matrix together with phyllosilicates (Fig. S4E), and were identified by TEM (Supplementary Material, S7 and Fig. S6). Carbonaceous materials (possibly IOMs) and cracks were also observed in the matrix (Fig. 1C: d and e, respectively Fig. 4B).

##### 3.2.2. Pyrrhotite (pink in RGB-CT images)

The Fe(-Ni) sulfides were mostly pyrrhotite (Fig. 1D) (mode:1.4 (0.0 ~ 9.3) vol. % including pentlandite; Table 2), and the abundance of

**Table 2**  
Modal abundance (in vol.%) of Ryugu particles of matrix category.

sample name	Po/Pen	Mt	Dol	Bre	CaCO <sub>3</sub>	Ap	Phos	Ol/Px	Chm	Pore	Matrix
A0063-FC005	1.1	2.4	0.9	n.d.	n.d.	0.4	n.d.	n.d.	n.d.	18.0	76.5
A0063-FC007	0.7	1.9	1.1	n.d.	n.d.	0.5	n.d.	n.d.	n.d.	12.2	83.2
A0064-FO022	0.7	0.0	0.0	n.d.	n.d.	0.0	n.d.	n.d.	n.d.	11.1	87.6
A0064-FO023	1.4	0.6	18.1	n.d.	n.d.	0.0	n.d.	n.d.	n.d.	23.3	56.5
A0064-FO024	3.1	1.1	0.6	n.d.	n.d.	0.3	n.d.	n.d.	n.d.	15.5	78.3
A0067-FC005	0.4	1.8	0.0	n.d.	n.d.	0.1	n.d.	n.d.	n.d.	7.3	87.7
A0067-FC007	2.1	1.8	0.0	n.d.	n.d.	0.0	n.d.	n.d.	n.d.	8.8	84.8
A0104-00000100	0.4	1.5	0.0	n.d.	n.d.	0.0	n.d.	n.d.	n.d.	16.6	81.2
A0104-00000200	1.4	8.1	0.0	n.d.	n.d.	0.1	n.d.	n.d.	n.d.	12.4	77.6
A0104-00000300	0.5	0.1	0.1	n.d.	n.d.	0.1	n.d.	n.d.	n.d.	14.8	84.0
A0104-00000400	0.2	0.3	0.1	n.d.	n.d.	0.1	n.d.	n.d.	n.d.	17.5	81.7
A0104-00000500	0.7	7.6	0.5	n.d.	n.d.	0.2	n.d.	n.d.	n.d.	12.4	78.6
A0104-00000600	2.8	0.9	0.1	n.d.	n.d.	0.0	n.d.	n.d.	n.d.	9.8	86.3
A0104-00000700	4.1	0.7	0.0	n.d.	n.d.	0.6	n.d.	n.d.	n.d.	15.2	79.2
A0104-00000800	0.3	0.7	0.2	n.d.	n.d.	0.1	n.d.	n.d.	n.d.	17.5	81.1
A0104-00001000	0.3	2.6	0.0	n.d.	n.d.	0.0	n.d.	n.d.	n.d.	9.9	86.8
A0104-00001100	0.3	1.9	1.1	n.d.	n.d.	0.4	n.d.	n.d.	n.d.	17.6	78.5
A0104-00001200	1.6	1.8	0.2	n.d.	n.d.	0.0	n.d.	n.d.	n.d.	12.4	83.5
A0104-00001300	0.0	0.1	0.1	n.d.	n.d.	0.0	n.d.	n.d.	n.d.	10.0	89.9
A0104-00001400	9.3	1.5	0.1	n.d.	n.d.	0.7	n.d.	n.d.	n.d.	15.9	72.0
A0104-00001700	1.7	3.6	0.0	n.d.	n.d.	0.0	n.d.	n.d.	n.d.	8.9	85.4
A0104-00001800	0.1	0.1	0.0	n.d.	n.d.	0.0	n.d.	n.d.	n.d.	9.1	90.6
A0104-00001900	0.9	0.2	0.0	n.d.	n.d.	0.0	n.d.	n.d.	n.d.	5.5	92.9
A0104-00002000	2.0	0.9	0.0	n.d.	n.d.	0.0	n.d.	n.d.	n.d.	10.8	85.5
A0104-00002100	0.4	1.4	0.0	n.d.	n.d.	0.4	n.d.	n.d.	n.d.	5.6	90.9
C0002-FC009_CT001	0.7	6.6	1.0	n.d.	n.d.	0.1	n.d.	n.d.	n.d.	11.3	80.1
C0023-FC003	2.3	3.2	1.7	n.d.	n.d.	0.7	n.d.	n.d.	n.d.	15.9	76.0
C0046-FO015	1.1	4.6	0.5	n.d.	n.d.	0.1	n.d.	n.d.	n.d.	8.0	84.4
C0061-FC005	1.3	3.0	0.0	n.d.	n.d.	0.1	n.d.	n.d.	n.d.	11.6	82.4
C0076-FC005	3.1	0.3	0.1	n.d.	n.d.	0.0	n.d.	n.d.	n.d.	16.6	79.6
C0107-FG018	0.5	7.8	0.5	n.d.	n.d.	0.3	n.d.	n.d.	n.d.	3.9	86.9
C0105-04300100	0.8	4.6	0.0	n.d.	n.d.	0.0	n.d.	n.d.	n.d.	8.6	85.3
C0105-04300200	0.1	1.3	7.3	n.d.	n.d.	0.4	n.d.	n.d.	n.d.	16.0	73.8
C0105-04300300	1.2	3.8	0.2	n.d.	n.d.	0.0	n.d.	n.d.	n.d.	12.9	81.7
C0105-04300400	1.4	5.5	0.6	n.d.	n.d.	0.1	n.d.	n.d.	n.d.	8.2	82.8
C0105-04300500	1.6	2.8	0.4	n.d.	n.d.	0.0	n.d.	n.d.	n.d.	6.6	87.7
C0105-04300600	1.0	3.8	2.4	n.d.	n.d.	0.2	n.d.	n.d.	n.d.	10.6	81.3
C0105-04300700	0.3	2.4	0.1	n.d.	n.d.	0.0	n.d.	n.d.	n.d.	11.9	84.0
C0105-04300800	1.5	2.0	5.3	n.d.	n.d.	0.0	n.d.	n.d.	n.d.	10.2	79.3
C0105-04300900	0.4	4.1	5.9	n.d.	n.d.	0.2	n.d.	n.d.	n.d.	15.6	73.1
Whole samples											
N	40	40	40			40				40	40
Average	1.4	2.5	1.2			0.2				12.2	82.0
Std	1.6	2.2	3.2			0.2				4.2	6.4
Min	0.0	0.0	0.0			0.0				3.9	56.5
Max	9.3	8.1	18.1			0.7				23.3	92.9
Mode* (%)	1.2	3.2	1.2			0.2				11.6	81.7
Chamber A											
N	25	25	25			25				25	25
Average	1.5	1.7	0.9			0.2				12.7	82.4
Std	1.9	2.0	3.6			0.2				4.4	7.4
Min	0.0	0.0	0.0			0.0				5.5	56.5
Max	9.3	8.1	18.1			0.7				23.3	92.9
Mode* (%)	1.4	2.1	0.7			0.3				13.8	80.7
Chamber C											
N	15	15	15			15				15	15
Average	1.2	3.7	1.7			0.1				11.2	81.2
Std	0.8	2.0	2.4			0.2				3.8	4.4
Min	0.1	0.3	0.0			0.0				3.9	73.1
Max	3.1	7.8	7.3			0.7				16.6	87.7
Mode* (%)	1.1	3.9	1.5			0.1				10.1	82.3
Ryugu											
C0002 Plate5 [1]	5	6.2	1.8	0.93	0.01	0.13	0.12	0.09	0.09	n.d.	85.7
C0002 Plate6 [1]	3.3	5.2	2.9	1.5	0.02	0.14	0.15	0.06	0.04	n.d.	86.7
5 particles [2]	2.4–5.5	3.6–6.8	1.6–21.2			0.2–0.7	n.d.	0–0.5	n.d.	2–13.6	63.5–88.0
16 particles [3]	1.1–5.2	0.5–6.5	0.4–6.9			0.2–1.9		0–2.9	n.d.	19.2–53.8	83.7–94.0
CI [4]	6.5	9.0	2.0			n.d.		1.0	n.d.	n.d.	n.d.
CI [5]	3.9	5.1	0			n.d.		5.8	n.d.	n.d.	n.d.
CI [6]	1.06	4.3	0.48			0.05		0.1	n.d.	n.d.	94.0

Po: pyrrhotite, Pen: pentlandite, Dol: dolomite, Bre: breunnerite, Ap: apatite, Phos: Mg-Na phosphate, Ol: olivine, Px: low-Ca pyroxene, Chm: chromite.

\*Modal abundance weighted by the particle volume.

[1] Nakamura et al. (2023): 2D data by EPMA, carbonaceous material not measured, Pore excluded, Dominated as major lithology.

[2] Ito et al. (2022): A0029, A0037, C0009, C0014, C0068. 2D data by EPMA, carbonaceous material not measured, Pore excluded.

[3] Nakamura et al. (2023): A0022, A0033, A0035, A0048, A0073, A0078, A0085, C0008, C0019, C0027, C0039, C0047, C0053, C0079, C0081, C0082. 2D data by

EPMA, carbonaceous material not measured, Pore estimated separately.

[4] King et al. (2015): Average of Arais, Orgueil and Ivuna.

[5] Bland et al. (2004): Orgueil.

[6] Alfing et al. (2019): Average of Arais, Orgueil, Ivuna and Tonk. 2D data by EPMA for grains > 5 μm.

n.d.: not determined.

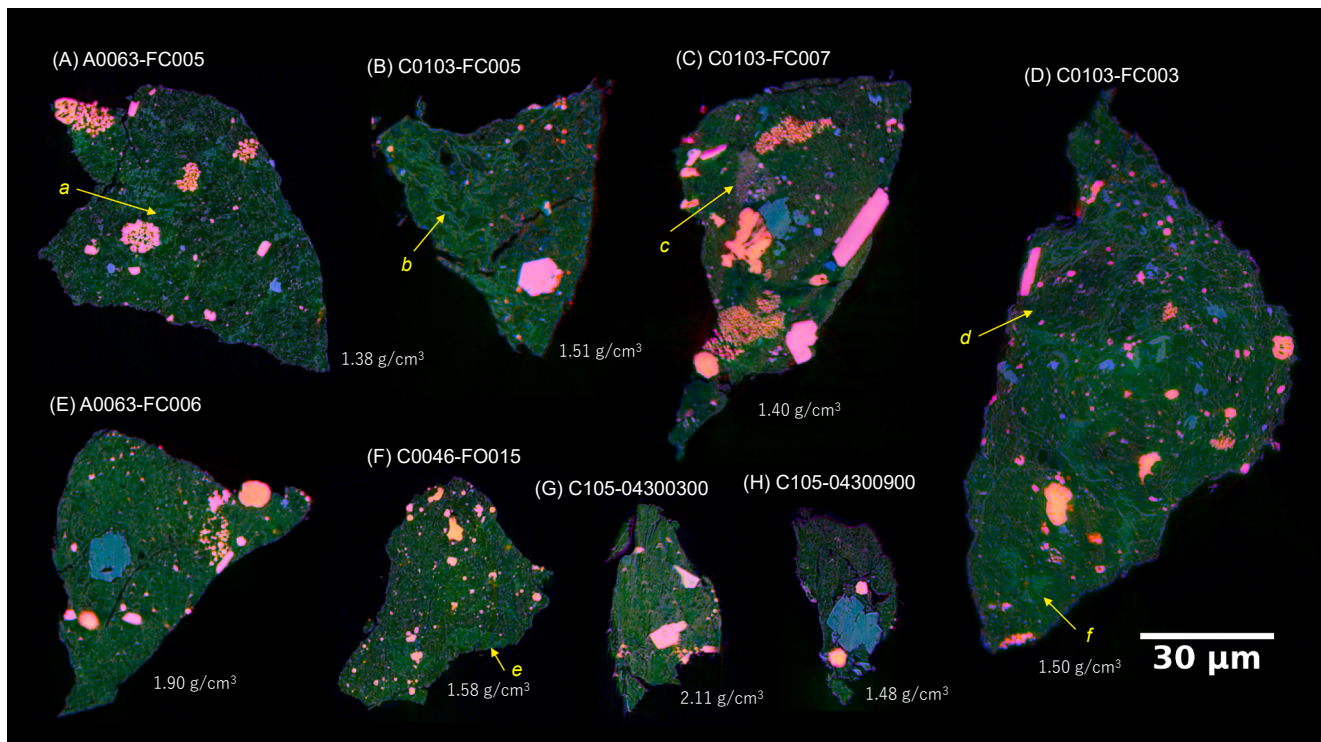


**Fig. 3.** RGB-CT images of representative sample particles. (A) A0063-FC005. (B) C0103-FC005. (C) C103-FC007. (D) C0103-FC003. (E) A0063-FC006. (F) C0046-FO015. (G) C105-04300300. (H) C105-04300900. The estimated matrix densities are presented in the figure. a, b, and f: Aggregates of coarse fibrous phyllosilicates. c, d, and e: Objects with sharp boundaries as clasts. The scale bar is the same for all particles.

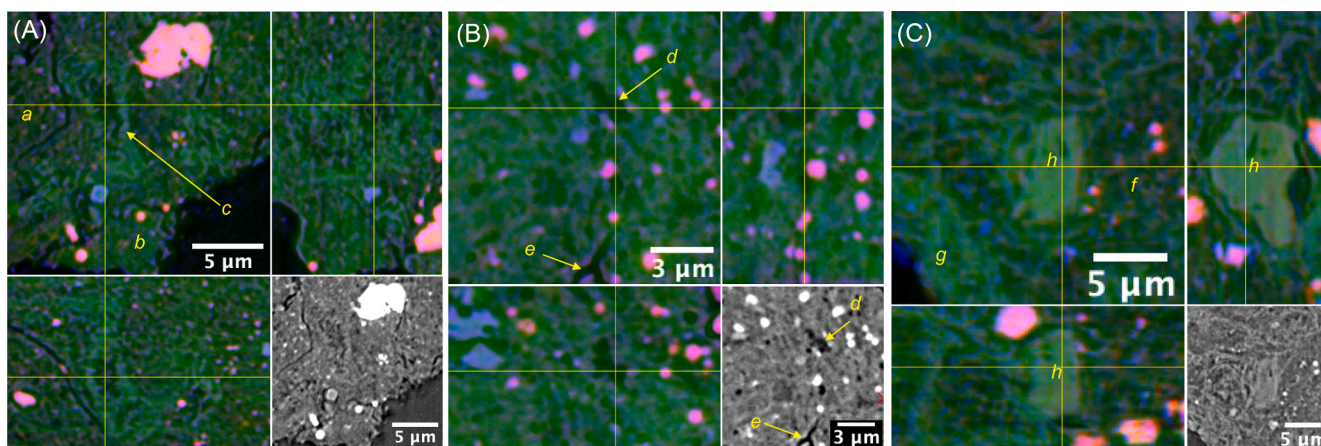


**Fig. 4.** RGB-CT images of the matrix and related objects shown as orthogonal views, where the XY slice is on the upper left, the YZ slice on the upper right, and the XZ slice on the lower left. The yellow lines indicate the slicing positions of each image. The LAC 7 image ( $-150\text{--}400\text{ cm}^{-1}$ ) in (C) and the LAC 7.35 images ( $-150\text{--}500\text{ cm}^{-1}$ ) in (A, B, and D-H) of the XY slices are also shown on the lower right. (A) C0046-FO015. a: dark-green matrix with Fe(-Ni) sulfide nanograins. b: bright green matrix. c: coarse fibrous phyllosilicate with a dark core. (B) C0002-FC009. d: carbonaceous material. e: crack. (C) C0103-FC005. f: dark green matrix with Fe(-Ni) sulfide nanograins. g: bright green matrix without Fe(-Ni) sulfide nanograins. h: bright green subhedral object. TEM images of the XZ slice are shown in Figure S5.

pentlandite was low. Troilite could not be distinguished from pyrrhotite by the DET-SIXM method, but it was identified as pyrrhotite by TEM (e.g., Nakamura et al., 2023; Noguchi et al., 2023a). Pyrrhotite was observed in almost all sample particles with different sizes of  $< \sim 60\text{ }\mu\text{m}$ ; c.f.  $10\text{--}100\text{ }\mu\text{m}$  in the CI chondrites (Brearley and Jones, 1998),

generally  $> 100\text{ }\mu\text{m}$  in Alais and Tonk, and always  $< 100\text{ }\mu\text{m}$  in Orgueil and Ivuna (Endreß and Bischoff, 1996). Any corroded structures observed in CI chondrites (e.g., Brearley and Jones, 1998) were not observed. As previously mentioned, small pyrrhotite (and sometimes dolomite) grains surrounded spherical objects composed of fine

phyllosilicate aggregates (b in Fig. S4A). Nanograins of Fe(-Ni) sulfides observed by TEM were also present in the matrix (a in Fig. 4A, f in Fig. 4C, and a in Fig. 4A), although those under XnCT spatial resolution were not recognized. Except for the nanograins, most sulfides were present as pseudo-hexagonal platelets with a combination of probably  $\{100\}$  and  $\{001\}$  faces in the pseudo-hexagonal setting. We measured the longest length,  $A$ , and shortest length,  $B$ , of the hexagon and the width,  $C$ , for 204 crystal grains (Supplementary Material, S8 and Fig. S7). The aspect ratio,  $R$ , defined as  $C/(A \times B)^{1/2}$ , ranged from 0.061 to 0.980, with an average of  $0.431 \pm 0.198$  (Fig. S7A), indicating the formation of thin to thick crystals. The degree of the ideal hexagon,  $H$ , defined by  $(B/A)/(B/A)_{id}$ , where  $(B/A)_{id} = 0.866$  for the ideal hexagon, has a skewed distribution (0.405–0.997; Ave. =  $0.865 \pm 0.093$ ) (Fig. S7B). There was no correlation between  $R$  and  $H$ . We did not detect any correlations of  $R$  and  $H$  with the crystal grain size and matrix feature (density or Mg#), and no difference between Chambers A and C. Some sulfides are aggregates of pseudo-hexagonal platelets. Rarely, there is a pseudo-hexagonal plate with a missing portion (c in Fig. 5B), or a fragment from a pseudo-hexagonal plate (Fig. 5C). Such fragmented crystal grains were abundant in one particular grain (C0023-FC003).

### 3.2.3. Pentlandite (white–pink in RGB-CT images)

Pentlandite occurs as small individual grains with facets. These were partially fractured (Fig. 5D). Pentlandite inclusions in pyrrhotite (Fig. 5A) and pyrrhotite overgrowths on pentlandite (Fig. 5E) were also observed. Based on TEM observations, nanograins of pentlandite and pyrrhotite are usually present in the matrix (Noguchi et al., 2023b; Matsumoto et al., 2024).

### 3.2.4. Magnetite (orange in RGB-CT images)

Magnetite was present in almost all the sample particles (mode:2.5 (0.0 ~ 8.1) vol. %; Table 2) as individual grains or aggregates showing a wide variety of morphologies with different sizes ( $< \sim$  a few tens of  $\mu\text{m}$ ) (e.g., Fig. 1D). Spherulites and spherical fan-shaped aggregates were commonly present as single objects ( $< 5 \mu\text{m}$ ) (Fig. 6A and B) or aggregates of several spherulites ( $\sim 10 \mu\text{m}$ ) (Fig. 6C). Some spherulites had external shapes with euhedral morphologies (Fig. 6B). Voids were occasionally observed in the interior (Fig. 6B and C). The size of the constituent crystals is usually very small compared to the XnCT spatial resolution; therefore, they were not individually recognized in the CT images, although the crystals could be recognized near the spherulite surfaces as growth fronts (Fig. 6A, B, and C). The shapes of the constituent crystals ranged from needle-like (bottom right panel of Fig. 6B)

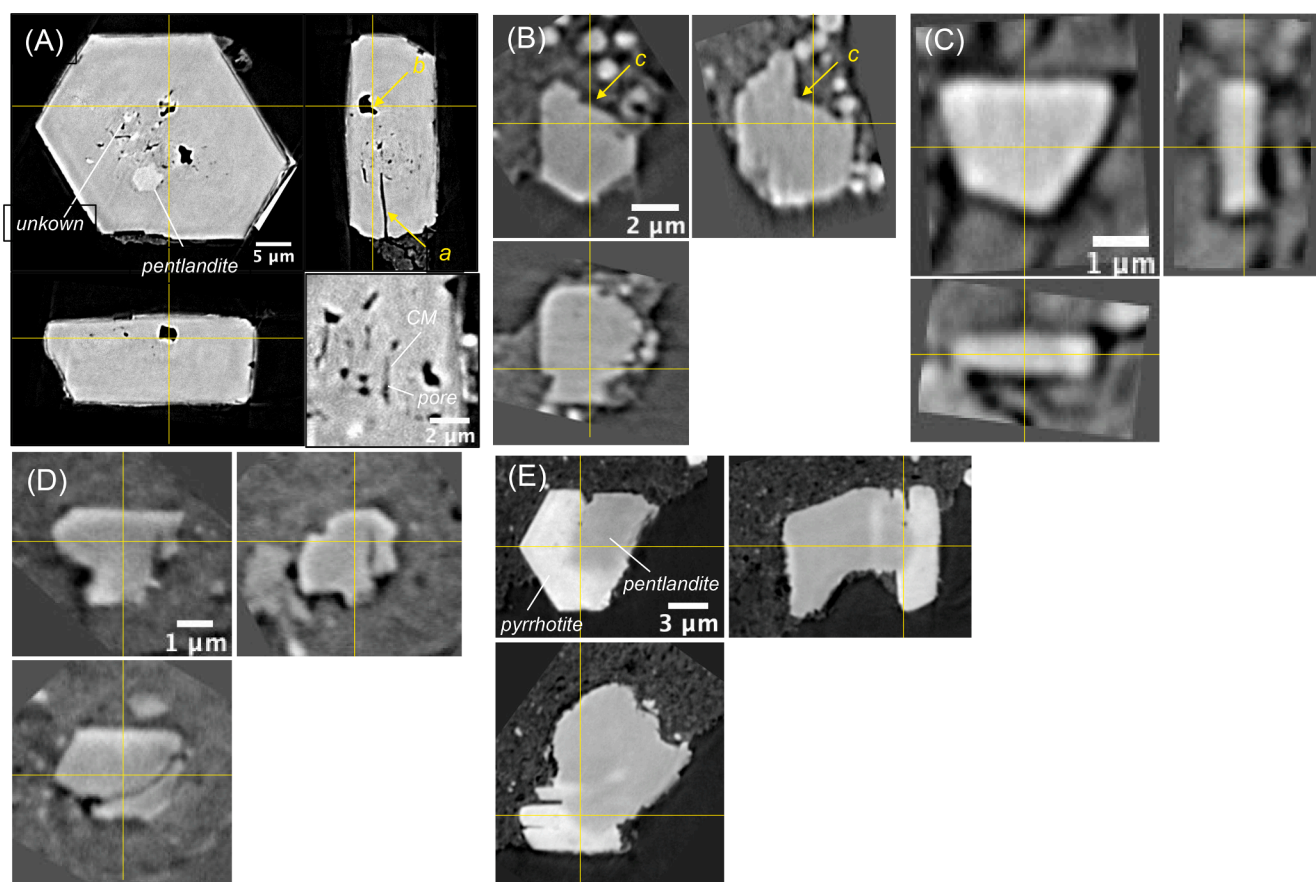


**Fig. 5.** Absorption CT images of Fe(-Ni) sulfide minerals shown as orthogonal views, where the XY slice is on the upper left, the YZ slice on the upper right, and the XZ slice on the lower left. The yellow lines indicate the slicing positions of each image. (A) Pseudo-hexagonal plate of pyrrhotite with pentlandite inclusions (LAC 7 keV: 0–500  $\text{cm}^{-1}$ , C0002-FC012). b: CO<sub>2</sub>-bearing aqueous fluid inclusion reported by Nakamura et al. (2023). The image on the lower right is an enlarged image of different YZ slice showing inclusions composed of carbonaceous materials (possibly IOMs) and pores. CM: carbonaceous material. (B) Hexagonal plate of pyrrhotite with a missing portion indicated by c (LAC 7 keV: 300–900  $\text{cm}^{-1}$ , C0023-FC003). (C) Pyrrhotite grain not showing a pseudo-hexagonal plate shape, probably a fragment of an originally pseudo-hexagonal plate (LAC 7 keV: 300–900  $\text{cm}^{-1}$ , C0023-FC003). (D) Pentlandite grain with facets (LAC 7 keV: 300–900  $\text{cm}^{-1}$ , C105-04300400). (E) Pentlandite overgrown by pyrrhotite (LAC 7.35 keV by ultra-high-resolution local tomography: 150–1400  $\text{cm}^{-1}$ , A0064-FO024). This may have been a fragment of a pseudo-hexagonal plate of pyrrhotite with a pentlandite core. Note that since the K-edge energies of Fe and Ni are 7.111 and 8.332 keV, respectively, pyrrhotite without Ni is slightly brighter than pentlandite with Ni in the 7 keV image (LAC values; pyrrhotite: 413.9  $\text{cm}^{-1}$  and pentlandite: 430.0  $\text{cm}^{-1}$ ), whereas pentlandite appears darker than pyrrhotite in the 7.35 keV image (LAC values; pyrrhotite: 1289.2  $\text{cm}^{-1}$ , pentlandite: 1084.2  $\text{cm}^{-1}$ ). In other words, the contrast between pyrrhotite and pentlandite is reversed in (A) and (E).

to blade-like (bottom right panel of Fig. 6C). TEM observations have shown that at least some of these are composed of single crystals or have domain structures with many nanopores and dislocations (Dobrică et al., 2023).

Plaquettes ( $< \sim 5 \mu\text{m}$ ), stacking of platy crystals, were observed (Fig. 6D); however, this was not very common ( $\sim 1/4$  of the particles belonging to the “matrix” category contained one or a few plaquettes). A transitional morphology from plaquette to irregular shape was also observed (Fig. 6E). Each plate was circular to irregular in shape in its cross section and usually contained thin voids. Some voids were faceted (e in Fig. 6D and g in Fig. 6E), whereas others were not (h in Fig. 6E). Some were filled with low-density material (i in Fig. 6E). Chan et al. (2016) reported that the plates of the plaquettes in carbonaceous chondrites including the CIs have  $\{100\}$  surfaces.

Framboidal aggregates, composed of submicron grains, typically  $\sim 10 \mu\text{m}$  in whole size were also common (Fig. 6F–H) (c.f., the largest framboid reported in the CI chondrites is  $165 \mu\text{m}$ ; Alfing et al., 2019). The constituent grains were almost homogeneous in size

(monodispersive), but their average grain sizes differed from a few  $100 \text{ nm}$  (Fig. 6F) to a few  $\mu\text{m}$  (Fig. 6H). Some of these were compact aggregates (Fig. 6G) and some resembled colloidal crystals with defects, regularly surrounded by individual crystals, although no clear periodic arrangement was observed (Fig. 6F). Facets can be seen for the constituent grains of at least coarse-grained aggregates, even with the XnCT resolution (Fig. 6H). We observed small void inclusions in a limited number of coarse grains (n in Fig. 6H). Many framboidal magnetite grains form trapezohedral crystals,  $\{311\}$ , in the Orgueil meteorite (CI) (Hua and Buseck, 1998). Nozawa et al. (2011) reported that the crystallographic surfaces were different for colloidal crystals of different sizes in the Tagish Lake meteorite (C2-ungr): fine ( $\sim 100 \text{ nm}$ ):  $\{111\}$ , medium ( $\sim$  a few  $100 \text{ nm}$ ):  $\{110\}$ , and coarse ( $\sim 1 \mu\text{m}$ ):  $\{311\} > \{110\} > \{100\}$ . The face indices could not be determined from CT images. Sometimes, we observed fine grains that were concentrated but not aggregated as framboids or were separately dispersed in the matrix. Fine grains are also present as veins. Hexagonal plate-shaped framboid aggregates, which would have suggested pyrrhotite plates breaking

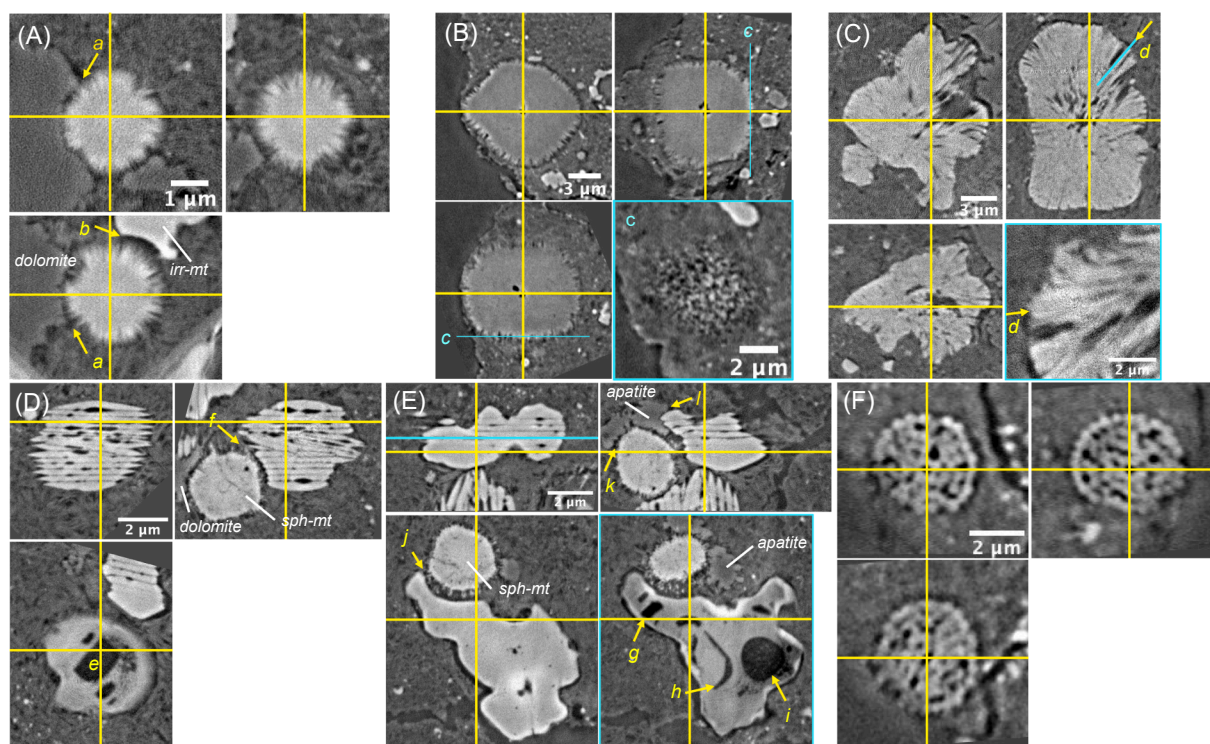


**Fig. 6.** Absorption CT images of magnetite shown as orthogonal views, where the XY slice is on the upper left, the YZ slice on the upper right, and the XZ slice on the lower left. The yellow lines indicate the slicing positions of each image. (A) Spherulite of near-true spherical shape (LAC 7.35 keV by ultra-high-resolution local tomography:  $800\text{--}2000 \text{ cm}^{-1}$ , A0094-FIB001). a: Surrounded by dolomite. b: Surrounded by irregularly-shaped magnetite (irr-mt). (B) Polyhedral shaped spherulite with pores at the center (LAC 7 keV:  $-200\text{--}600 \text{ cm}^{-1}$ , C105-04300100). The image on the lower right is the XY slice at different position indicated by cyan lines (c), indicating that the spherulite is composed of needle-like crystals. (C) Aggregate of several spherulites (LAC 7.35 keV by ultra-high-resolution local tomography:  $800\text{--}2000 \text{ cm}^{-1}$ , C0103-FC007). The image on the lower right is the slice indicated by the cyan line (d), indicating that the spherulite is composed of blade-like crystals. (D) Plaquette (LAC 7.35 keV by ultra-high-resolution local tomography:  $800\text{--}2000 \text{ cm}^{-1}$ , A0067-FIB006). e: Faceted void in a platy crystal. f: Spherulitic magnetite (sph-mt) surrounded by plaquette. (E) Transitional morphology from plaquette to irregular shape (LAC 7.35 keV by ultra-high-resolution local tomography:  $800\text{--}2000 \text{ cm}^{-1}$ , A0067-FIB006). The image on the lower right is the slice by the cyan line, indicating that a platy crystal has different types of inclusions. g: Faceted void in a platy crystal. h: Irregularly-shaped void. i: Inclusion filled with a low-density material. j: Spherulitic magnetite (sph-mt) surrounded by plaquette. k: Spherulitic magnetite surrounded by apatite. l: Plaquette magnetite surrounded by apatite. (F) Framboid resembling a colloidal crystal with defects (LAC 7 keV:  $-200\text{--}600 \text{ cm}^{-1}$ , C105-04300100). (G) Framboid as a compact aggregate (LAC 7.35 keV by ultra-high-resolution local tomography:  $800\text{--}2000 \text{ cm}^{-1}$ , A0067-CT001). m: Pyrrhotite surrounded by framboid. (H) Framboid as a loose aggregate (LAC 7.35 keV by ultra-high-resolution local tomography:  $800\text{--}2000 \text{ cm}^{-1}$ , A0067-CT001). n: Very small void inclusions. (I) Coarse and euhedral grain (LAC 7 keV:  $-200\text{--}600 \text{ cm}^{-1}$ , C0002-FC009). Four large and four small angles ( $\alpha$  and  $\beta$ , respectively) between the two edges are positioned with respect to each other. The angles measured by the CT image ( $142\text{--}144^\circ$  and  $126\text{--}130^\circ$ ) are consistent with  $\{311\}$  ( $143.1^\circ$  and  $126.9^\circ$ ), as shown in the illustration on the bottom right. (J) Rod-shaped elongated grain with facets (LAC 7.35 keV by ultra-high-resolution local tomography:  $800\text{--}2000 \text{ cm}^{-1}$ , C105-04300900). If we assume that this rod is elongated in the  $\langle 100 \rangle$  direction, the measured angles between the side faces in the CT image ( $\alpha \sim \beta \sim 135^\circ$ ) appear to be explained by  $\{100\}$  and  $\{110\}$ , as shown in the illustration on the bottom right. (K) Irregularly-shaped elongated grain with voids (LAC 7.35 keV by ultra-high-resolution local tomography:  $800\text{--}2000 \text{ cm}^{-1}$ , A0094-FIB001). o: This grain surrounded by dolomite. (L) Irregularly-shaped grain with spherulitic

features (LAC 7.35 keV by ultra-high-resolution local tomography:  $800\text{--}2000\text{ cm}^{-1}$ , C105-04300100). (M) Cube probably composed of  $\{100\}$  faces (LAC 7 keV:  $-200\text{--}800\text{ cm}^{-1}$ , C0076-FC005). mt cube: magnetite cube.

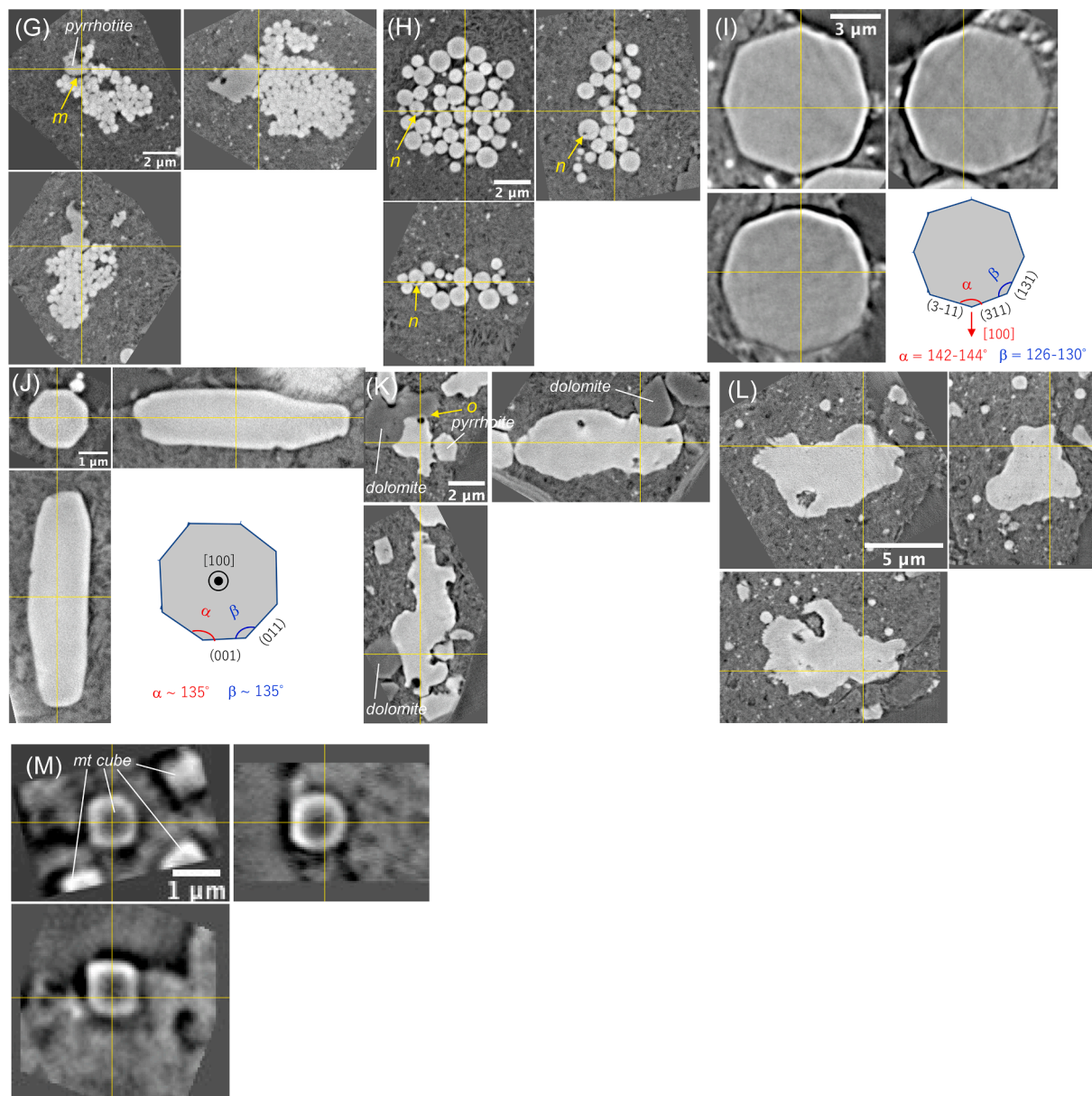


Fig. 6. (continued).

down into framboids, were not observed.

Some samples had coarse and euhedral grains ( $< \sim 10\ \mu\text{m}$ ) (Fig. 6I). The facets were composed of  $\{311\}$  planes, which were estimated from the angles between the facets in the ultra-high-resolution CT (LCT) images. Rod-shaped elongated grains with facets ( $\sim < 2\ \mu\text{m}$  in width and  $\sim 10\ \mu\text{m}$  in length) (Fig. 6J) were also observed. The elongation was along  $\langle 100 \rangle$  with the side faces of  $\{100\}$  and  $\{110\}$ , deduced from the angles between the facets. Coarse, irregularly shaped elongated grains were also present ( $\sim 10\ \mu\text{m}$ ) (Fig. 6K) (c.f. up to  $27\ \mu\text{m}$  in CI chondrites; Alfing et al., 2019). They usually have voids inside and appear to be transitional from spherical aggregates (Fig. 6L). Rod- and irregularly shaped grains were abundant in one grain (C0105-04300400).

In addition to the above morphologies, we also observed fine cubic grains (Fig. 6M). They are almost  $\sim 1\ \mu\text{m}$  in size and may be composed of  $\{100\}$  faces. Numerous cubes were present in the veins in one sample (C0076-FC005), and some were observed in others (e.g., C0002-FC009, C0076-02-CT002, and C105-04300200). A whisker  $4.1\ \mu\text{m}$  in length and

$0.2\ \mu\text{m}$  in width was observed in A0104-0000700 (Fig. 7). We extracted a section containing this whisker and observed it using TEM. This was elongated in the  $\langle 100 \rangle$  direction, and no dislocations were observed. Four more whiskers (mostly  $0.2\ \sim 0.4\ \mu\text{m}$  in width with the aspect ratio of  $5\ \sim 17$ ) were observed in A063-FC010, A0104-0001000, C105-04300400, and C105-04300900, but their phases were not determined by the DET-SIXM method for these thin needles.

### 3.2.5. Dolomite (grayish-blue-green in RGB-CT images)

Dolomite grains of different sizes ( $< \sim 60\ \mu\text{m}$ ) and abundances (mode: 1.2 (0.0  $\sim$  18.1) vol.%; Table 2) were present in the matrix (Fig. 1D, 6 K, and 8). One sample is composed of two large dolomite grains (Fig. 8A). Dolomite contains some Mn and Fe (e.g., Nakamura et al., 2023; Nakato et al., 2022), which are shown in the LACs-RID histogram (Fig. S3). Chemical zoning from an Fe- and Mn-poor core to Fe- and Mn-rich rim can be seen (the rim is brighter than the core in the left crystal: right bottom panel of Fig. 8A). Corroded structures rimmed

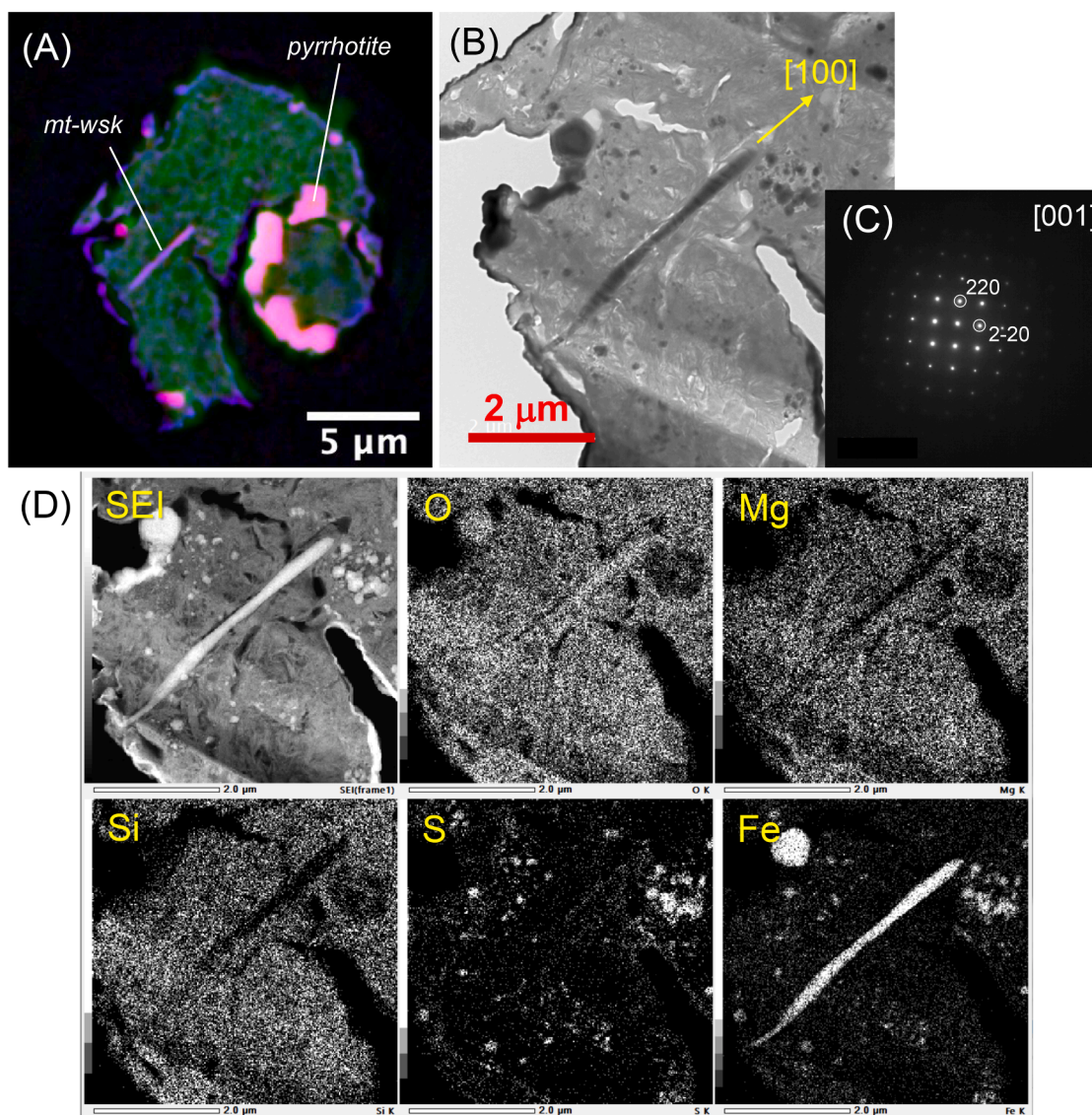


**Fig. 7.** Magnetite whisker (mt-wsk) in A0104-00000700 (~4.1  $\mu\text{m}$  long and ~0.2  $\mu\text{m}$  wide). (A) RGB-CT image corresponding to (B) the bright-field TEM image. (C) SAED pattern of the whisker indexed to magnetite. (D) Elemental maps obtained using TEM-EDS. A spherical phyllosilicate object surrounded by small pyrrhotite grains is also observed in (A).

by gypsum, which are usually seen in CI chondrites (Morlok et al., 2006), were not observed. Dolomite occurs mostly as euhedral or subhedral grains or as aggregates. Some had large pores inside the aggregates (Fig. 8B). Simple euhedral grains were rare but present and showed flattened rhombohedrons (Fig. 8C) with an aspect ratio of ~0.85, suggesting that the crystal is composed of  $\{104\}$  faces. This corresponds to the equilibrium form of calcite, which is composed mainly of  $\{104\}$  faces (Bruno et al., 2013). Aggregates of fine dolomite grains were also present in the matrix (Fig. S4E and Fig. S6).

### 3.2.6. Apatite (purple-blue in RGB-CT images)

Apatite was present in the matrix as small grains (<~10  $\mu\text{m}$ ) less abundant than dolomite (mode: 0.2 (0.0 ~ 0.7) vol.%; Table 2). This is hydroxyapatite identified by EPMA and TEM (Nakamura et al., 2023; Nakato et al., 2022; Noguchi et al., 2023b) (c.f. largest “phosphate” in CI chondrites is 10 ~ 20  $\mu\text{m}$ : Alfing et al., 2019). Apatite is usually an aggregate of smaller subhedral to euhedral crystals (Fig. 1D, 6E, and 9). Some grains had many voids and were partially dendrite-like (e.g., a and b in Fig. 9A). A hexagonal prism (3.0  $\mu\text{m}$  in length and 2.8  $\mu\text{m}$  in height) was observed (Fig. 9B). This is probably composed of  $\{100\}$  and  $\{001\}$

faces and might correspond to the equilibrium form (c.f., the equilibrium form of monoclinic hydrous apatite is composed of  $\{100\}$  and  $\{001\}$  faces in the hexagonal setting; Aquilano et al., 2014).

### 3.2.7. Brunnerite (Fe-bearing magnesite; yellowish-green in RGB-CT images)

Brunnerite was found as relatively large grains (<~1 mm) in coarse sample particles (Nakamura et al., 2023) (c.f. largest brunnerite in CI chondrites is ~3 mm; Fredriksson and Kerridge, 1988). In fact, it was found as independent particles (30–100  $\mu\text{m}$ ) (Fig. 10A), but small grains (<~10  $\mu\text{m}$ ) were also observed in two particles of the “matrix” category (A0067-FIB005 and A0067-CT001). The two independent grains examined (A0067-FC003 and A0067-FC004) had nearly euhedral rhombohedral shapes that were more flattened than dolomite crystals. The chemical composition of  $(\text{Mg}_{0.6-0.7}\text{Fe}_{0.4-0.3})\text{CO}_3$  obtained from the LACs-RID histogram is consistent with the EPMA analysis (Nakamura et al., 2023) and exhibits zoning with an Fe-rich rim (yellowish in the RGB-CT images) (Fig. 10A).

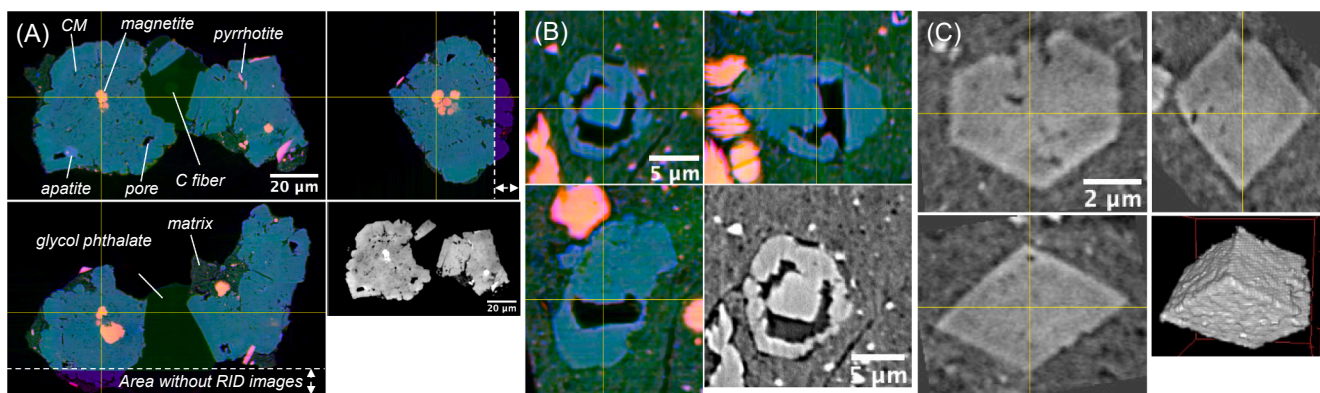


**Fig. 8.** CT images of dolomite shown as orthogonal views, where the XY slice is on the upper left, the YZ slice on the upper right, and the XZ slice on the lower left. The yellow lines indicate the slicing positions of each image. (A) RGB CT image of a sample particle containing two large grains (C0076-FO006). The XY slice of the RID image ( $5\text{--}9.25 \times 10^6$ ) is also shown on the lower right. Magnetite, pyrrhotite, apatite, carbonaceous material (possibly IOM), and void inclusions are present. The sample is held using an amorphous carbon fiber (C fiber) with glue (glycol phthalate). The CT slices where the RID images were not taken are shown in different colors from the RGB images. CM: carbonaceous material. (B) RGB CT image of a grain with a large void connected to the outside (A0063-FC006). The XY slice of the LAC 7 keV image ( $-150\text{--}400 \text{ cm}^{-1}$ ) is also shown on the lower right. (C) LAC 7 keV image ( $-200\text{--}600 \text{ cm}^{-1}$ ) of a flattened rhombohedral grain (C105-04300400). A bird's-eye view of this grain is shown on the lower right.

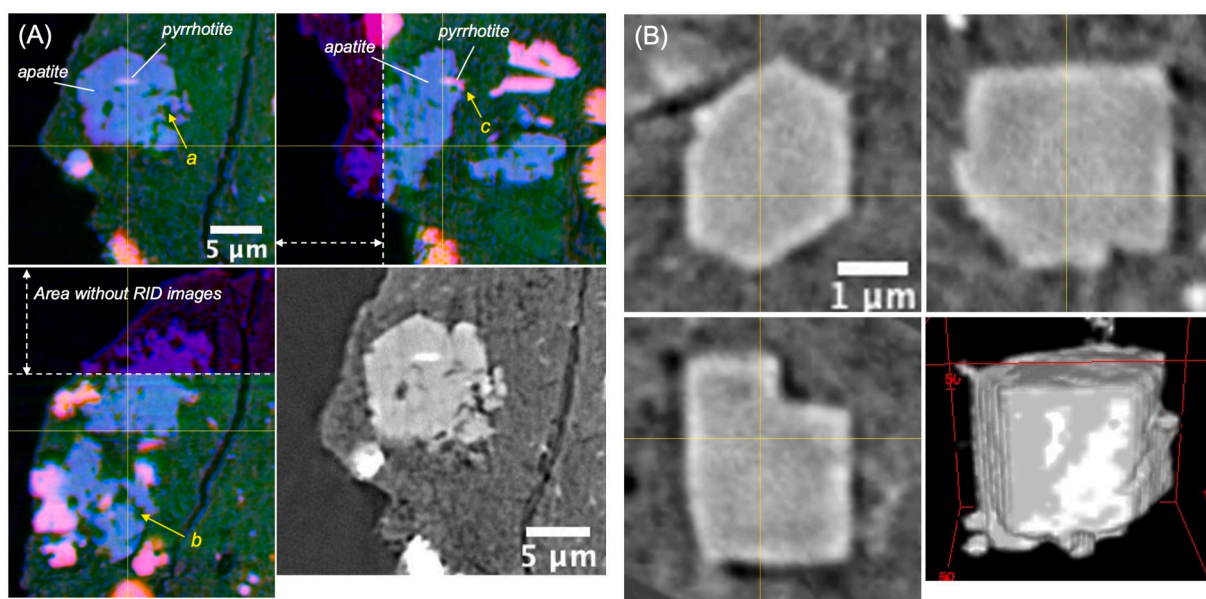


**Fig. 9.** CT images of apatite shown as orthogonal views, where the XY slice is on the upper left, the YZ slice on the upper right, and the XZ slice on the lower left. The yellow lines indicate the slicing positions of each image. (A) RGB CT image of coarse dendrite-like grains with many inclusions (voids or IOMs) (A0063-FC006). The XY slice of the LAC 7.35 keV image ( $-150\text{--}500 \text{ cm}^{-1}$ ) is also shown on the lower right. Hexagonal facets are observed in the XY slice. Some portions resemble coarse dendritic aggregates, as indicated by a and b. Pyrrhotite is surrounded by apatite, as indicated by c. The CT slices where the RID images were not taken are shown in different colors from the RGB images. (B) LAC 7 keV image ( $-200\text{--}600 \text{ cm}^{-1}$ ) of a hexagonal prism grain (C105-04300400). A bird's-eye view of this crystal is shown on the lower right.

### 3.2.8. Mg-Na phosphate phase (dark green in RGB-CT images)

This phase, recognized by Nakamura et al. (2023) using SEM and EPMA, was observed as an independent particle ( $\sim 30 \times 30 \times 100 \mu\text{m}$ : C0046-FO018) in this study (Fig. 10B). This irregularly shaped particle has a shriveled structure with large cracks running along nearly two perpendicular directions and many small cracks surrounded by large cracks. The mean RID value indicates a low density of  $\sim 1.3 \text{ g/cm}^3$  (Table 1). This may be a pseudomorph of the  $\text{H}_2\text{O}$ -bearing precursor phase, in which cracks are formed by dehydration (Nakamura et al., 2023).

### 3.2.9. Minor phases

Two grains of olivine or low-Ca pyroxene (emerald-green in RGB-CT images) were present as minor phases, although we could not

discriminate olivine from low-Ca pyroxene using the DET-SIXM method. One is a small anhedral grain of forsterite or enstatite of almost  $\text{Fo}_{100}$  or  $\text{En}_{100}$  ( $1.5 \times 2 \times 3 \mu\text{m}$  in size) (Fig. 11A). The other is a relatively coarse grain ( $9 \times 18 \times 18 \mu\text{m}$  in size; *c.f.* the largest olivine/pyroxene in CI chondrites is  $25 \mu\text{m}$  (Alfing et al., 2019); largest olivines in CIs and Ryugu are  $\sim 30$  and  $20 \mu\text{m}$ , respectively (Kawasaki et al., 2023)). This grain is relatively rich in Fe ( $\text{Fo}_{85}$  or  $\text{En}_{75}$  based on the LAC values) and has a euhedral shape with facets and macro growth steps (Fig. 11B). Sulfates (gypsum and epsomite) and ferrihydrite, which are usually found in CI chondrites (e.g., Tomeoka and Buseck, 1988; Brearley and Jones, 1998), were not identified. This was expected since these phases were long ago suggested to have formed on Earth (Gounelle and Zolensky, 2001).

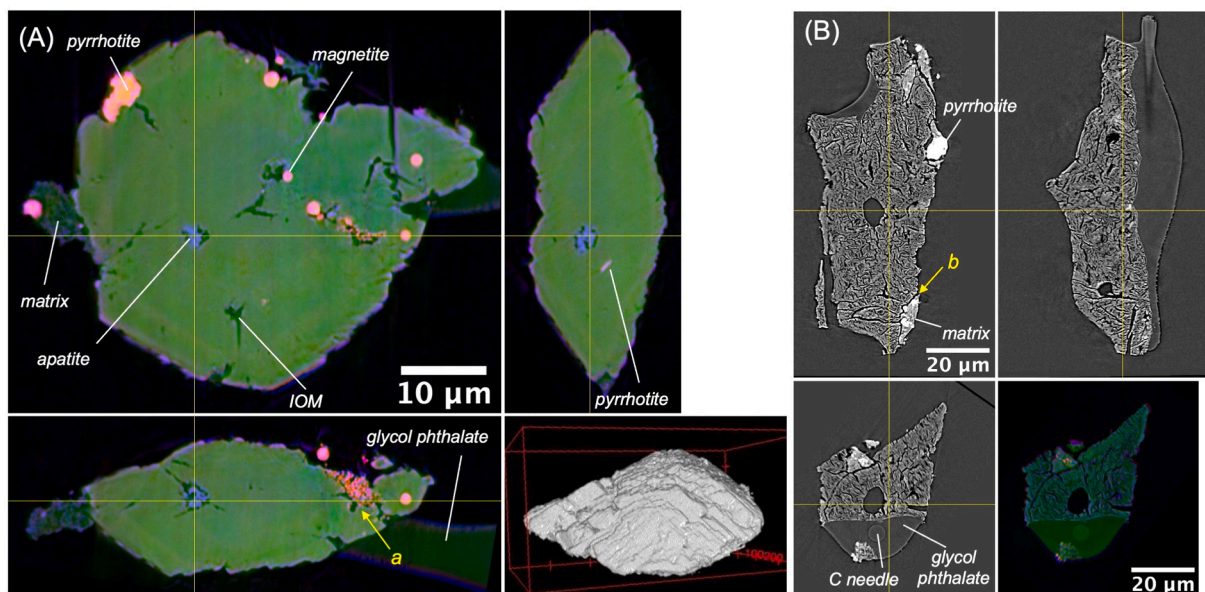


**Fig. 10.** CT images of minor minerals shown as orthogonal views, where the XY slice is on the upper left, the YZ slice on the upper right, and the XZ slice on the lower left. The yellow lines indicate the slicing positions of each image. (A) RGB CT image of breunnerite grain with a flattened rhombohedral shape (A0067-FC003). A bird's-eye view of this grain is shown on the lower right. Magnetite, pyrrhotite, apatite, carbonaceous materials, and void inclusions are present. The carbonaceous material was identified as IOM using micro-Raman measurements (Supplementary Material, S10 and Fig. S9). Framboidal magnetite is surrounded by breunnerite, as indicated by a. (B) LAC 7.35 keV image ( $\sim 100\text{--}300\text{ cm}^{-1}$ ) of an Mg-Na phosphate grain, which may be a pseudomorph of the  $\text{H}_2\text{O}$ -bearing precursor phase (Nakamura et al., 2023) (C0046-FO018). The XZ slice of the RGB CT image is shown on the lower right. Pyrrhotite is not surrounded by the Mg-Na phosphate but the matrix containing pyrrhotite grain is simply attached to the phosphate crystals. A crack between Mg-Na phosphate and matrix is indicated by b.

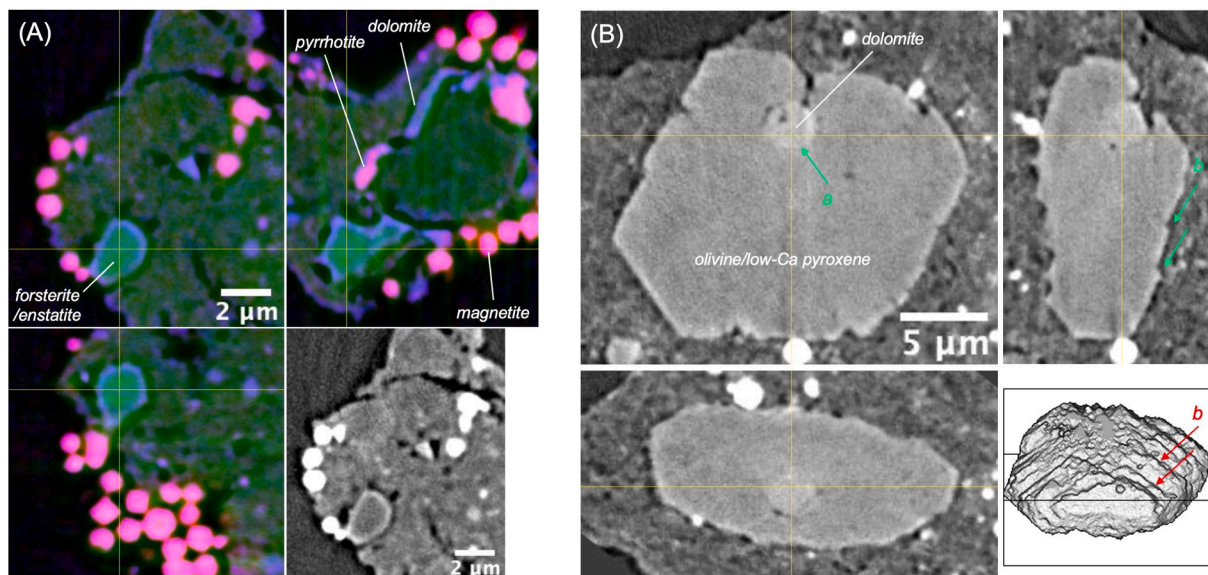


**Fig. 11.** CT images of olivine or low-Ca pyroxene shown as orthogonal views, where the XY slice is on the upper left, the YZ slice on the upper right, and the XZ slice on the lower left. The yellow lines indicate the slicing positions of each image. (A) RGB CT image of forsterite or enstatite (A0104-00000500) with irregular shape. This is probably forsterite estimated from the LAC-RID histograms, but the possibility of enstatite cannot be excluded. A spherical phyllosilicate object surrounded by small pyrrhotite and dolomite grains is also observed in the YZ slice. The XY slice of the LAC 7.35 image ( $\sim 150\text{--}500\text{ cm}^{-1}$ ) is also shown on the lower right. (B) The LAC 7.35 image ( $\sim 150\text{--}500\text{ cm}^{-1}$ ) of olivine ( $\text{Fo}_{85}$ ) (A0063-FC010) with facets. This is probably olivine, but the possibility of low-Ca pyroxene ( $\text{En}_{75}$ ) cannot be excluded. A small dolomite grain is surrounded by olivine (or low-Ca pyroxene), as indicated by a. Mineral phases and their chemical compositions were determined using their LAC-RID values. A bird's-eye view of this grain is shown on the lower right. The crystal is faceted and exhibits a euhedral shape near the hexagonal plate. Macro growth steps were also observed, as indicated by b.

### 3.2.10. Carbonaceous materials (dark green in RGB-CT images)

Carbonaceous materials were observed as small, isolated objects (sub-micron to a few  $\mu\text{m}$ ) in the matrix of almost all the sample particles (Fig. 1C and 4B(d)). Many of these particles may correspond to insoluble organic matters (IOMs) as reported in the Ryugu samples (Yabuta et al.,

2023), but we would not be able to distinguish them from soluble organic matters (SOMs) if they are large enough to be observed by XnCT. In addition, small IOMs were not easily distinguished from voids due to the poor spatial resolution of the RID images and refraction artifacts in the LAC images. Therefore, the abundance of carbonaceous materials

was not determined. They were also present as inclusions in some minerals (e.g., pyrrhotite and breunnerite), and IOM inclusions in breunnerite were confirmed by micro-Raman spectroscopy, as described later.

### 3.3. Specific objects

We occasionally observed dark pink objects in RGB-CT images with irregular shapes ( $\sim 10 \mu\text{m}$ ) in the matrix (Fig. 1D, 3C (c), and 12A). These objects consisted of fine-grained materials, which were suggested to be a mixture of relatively Fe-enriched anhydrous silicates based on their LAC and RID values. Alternatively, they might be composed of dehydrated phyllosilicates and fine grains of Fe(-Ni) sulfides. Relatively coarse grains of Fe(-Ni) sulfides are sometimes accompanied. We refer to this clast as an Fe-enriched clast.

Very porous objects (VPO) with irregular shapes ( $\sim 5 \mu\text{m}$  in size) were occasionally observed in the matrix (Fig. 12B). Similar objects were observed in the ultra-porous lithology (UPL) of the primitive carbonaceous chondrite of Acfer 094 (C-ungrouped), where its matrix experienced only a limited degree of aqueous alteration (Matsumoto et al., 2019). The UPL is a mixture of fine grains of the Acfer 094 matrix itself and pores with sizes ranging from 100 nm to a few  $\mu\text{m}$ , and it was proposed that ice used to be present in the pores. By contrast, VPO contains low-density materials with pores. They might have originally been objects similar to UPLs that experienced aqueous alteration.

A relict of a barred olivine chondrule ( $\sim 30 \mu\text{m}$  in diameter) that underwent aqueous alteration was also observed in 3D (C0076-02-CT002). Details have been reported by Nakamura et al. (2023).

Fe-rich glass with vesicles was observed on the surfaces of some sample particles (e.g., Fig. 12C). This glass corresponds to melt splashes on the particle surface caused by meteoroid impacts (Noguchi et al., 2023a; Matsumoto et al., 2024; Matsumoto et al., 2023). Their density, estimated from the RID values in Eq.(1), is from 2.1 to 2.4  $\text{g}/\text{cm}^3$  (Table 1).

### 3.4. Pores and cracks

Pores and cracks were identified in the CT images. Thick cracks (maximum width of  $\sim 2 \mu\text{m}$ ) were observed in some particles (e.g., Fig. 3A, B, G, and H), whereas no cracks are observed in the other samples.

Three flaky particles (A0104-00000400 with  $S/L = 0.278$  and  $I/L = 0.646$ , A0104-00000800 with  $S/L = 0.239$  and  $I/L = 0.589$ , and C0076-FC005 with  $S/L = 0.233$  and  $I/L = 0.444$ , where  $S$ ,  $I$ , and  $L$  are the

shortest, intermediate, and longest lengths of the bounding box for a particle, respectively) had cracks running almost parallel to their flat shapes (Fig. 13A). A similar structure has been reported for larger particles ( $>1 \text{ mm}$ ) owing to impact (Nakamura et al., 2023). Similar morphological features have also been reported for flying particles during touchdown operations in Ryugu (Tachibana et al., 2022). All the cracks and most of the pores were connected outwards, and the porosity, including these cracks and pores (some of them might be filled with carbonaceous materials), was roughly estimated for individual sample particles using LAC images at 7.35 keV (3.0  $\sim$  23.3 vol% and  $12.2 \pm 4.2$  vol% on average) (Table 2). These values are smaller than the nanoporosity of 19.7 to 51.8 % (average:  $36.1 \pm 8.9$  %) estimated from the mean matrix density using RID images and the assumed density of phyllosilicate. This difference is primarily because the porosity was obtained from cracks and pores larger than the effective spatial resolution of the LAC images ( $\sim 200 \text{ nm}$ ), whereas the nanoporosity includes nanopores smaller than this resolution.

In addition to impacts, another possible cause of crack formation is the volumetric shrinkage of the water-containing matrix during drying. There is also a significant possibility that the cracks were enlarged due to thermal fatigue (Delbo et al., 2014) caused by thermal cycling on the surface of the object.

### 3.5. Unique sample particles

Two unique sample particles were observed. One is composed of fragmented calcite grains  $< \sim$  a few  $\mu\text{m}$  in size (blue in RGB-CT images) and phyllosilicates embedded in a matrix mainly of  $\text{Al}_2\text{Si}_2\text{O}_5(\text{OH})_4$  (kaolinite, nacrite, or dickite) (green in RGB-CT images) (A0104-00001500: Fig. 13B). Calcite and  $\text{Al}_2\text{Si}_2\text{O}_5(\text{OH})_4$  were determined by TEM/EDS, but we could not discriminate kaolinite, nacrite, and dickite, even by SAED (Supplementary Material, S9 and Fig. S8). Phyllosilicates appear to be serpentine and/or saponite, but we did not determine the phase(s) by SAED.

The other unique sample was composed of  $\text{CaCO}_3$  (calcite or aragonite), phyllosilicate (probably serpentine and/or saponite), and tochilinite-cronstedtite intergrowth (TCI) embedded in the matrix of carbonaceous material (C0076-FO001, Fig. 13C).  $\text{CaCO}_3$  grains (blue in RGB-CT images)  $< \sim 20 \mu\text{m}$  in size were euhedral to subhedral in shape. The phyllosilicate (light green) was Mg-rich and formed subhedral to euhedral grains  $< \sim 10 \mu\text{m}$  in size. Some were banded. These are likely pseudomorphs of Mg-rich silicates. TCI-like objects  $\sim 10 \mu\text{m}$  in size (brownish-orange) were irregular in shape and not very abundant. A large tabular grain of carbonaceous material ( $\sim 50 \times 40 \times 6 \mu\text{m}$ ) with

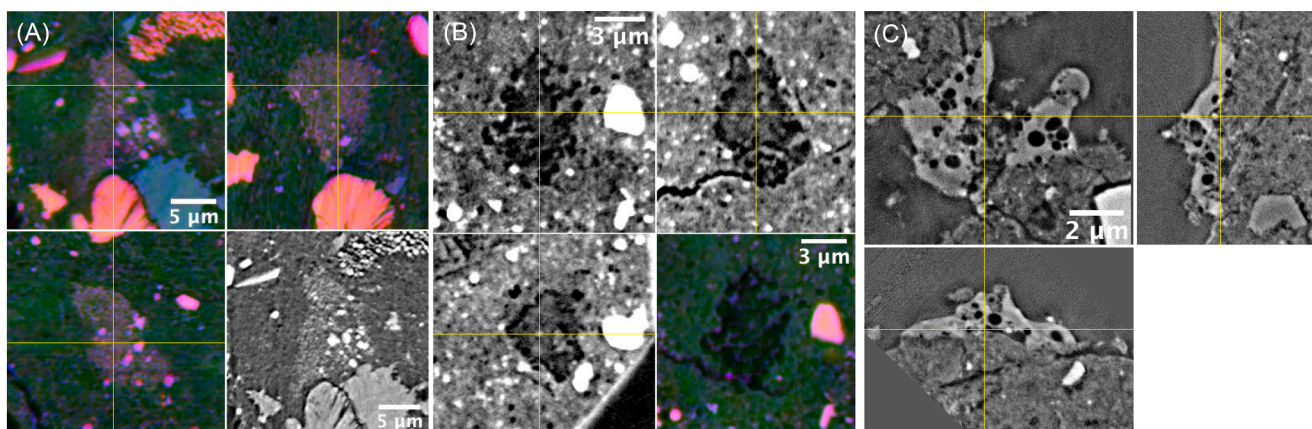


**Fig. 12.** CT images of different objects shown as orthogonal views, where the XY slice is on the upper left, the YZ slice on the upper right, and the XZ slice on the lower left. The yellow lines indicate the slicing positions of each image. (A) RGB CT image of Fe-enriched clast (C0103-FC007). The XY slice of the LAC 7 keV image ( $-150$ – $400 \text{ cm}^{-1}$ ) is also shown on the lower right. (B) LAC 7.35 keV image ( $0$ – $300 \text{ cm}^{-1}$ ) of very porous object (VPO) with an irregular shape ( $4 \times 5 \times 7 \mu\text{m}$  in size) (C0076-02-CT002). The RGB CT image of the XY slices is also shown on the lower right. (C) LAC 7.35 keV image ( $-600$ – $1600 \text{ cm}^{-1}$ ) of melt splash obtained by ultra-high-resolution local tomography (C105-04300900). Glass with many spherical voids is attached to the sample surface.

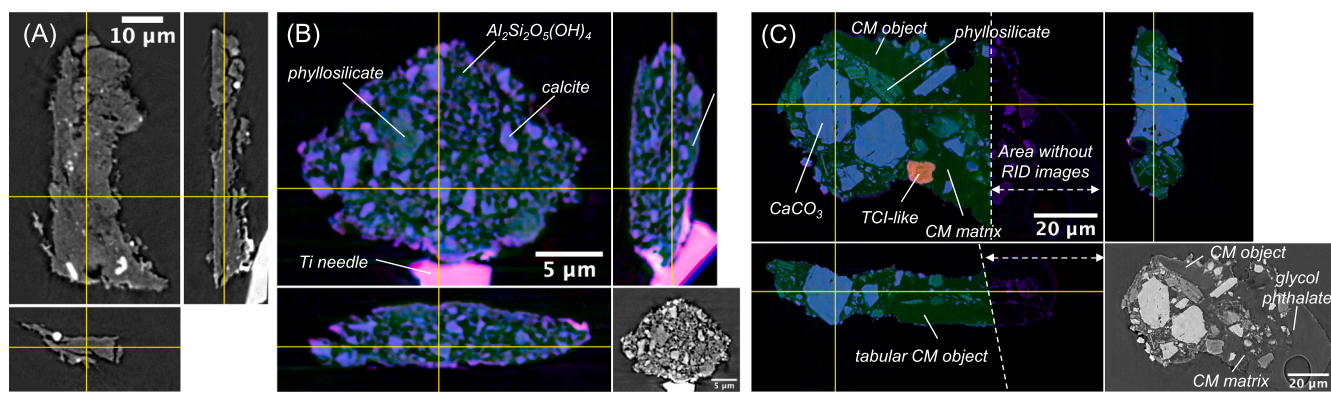


**Fig. 13.** CT images of a particle with a specific shape and unique particles shown as orthogonal views, where the XY slice is on the upper left, the YZ slice on the upper right, and the XZ slice on the lower left. The yellow lines indicate the slicing positions of each image. (A) LAC 7.35 keV image ( $-200$ – $100$   $\text{cm}^{-1}$ ) of thin particle with cracks running almost parallel to the flat shape (A0104-00000800). (B) RGB CT image of a unique particle with calcite and phyllosilicate embedded in  $\text{Al}_2\text{Si}_2\text{O}_5(\text{OH})_4$  (kaolinite, nacrite, or dickite) matrix (A0104-00001500). The XY slice of the LAC 7 keV image ( $-150$ – $400$   $\text{cm}^{-1}$ ) is also shown on the lower right. The TEM images are shown in Figure S8. (C) RGB CT image of a unique particle composed of  $\text{CaCO}_3$  (calcite or aragonite), phyllosilicate, and tochilinite-cronstedtite intergrowth embedded in a carbonaceous material matrix (C0076-FC001). Different carbonaceous material objects ( $\sim 1.2$   $\text{g}/\text{cm}^3$ ) are also present in the IOM matrix ( $\sim 1.1$   $\text{g}/\text{cm}^3$ ). The XY slice of the LAC 7 keV image ( $-150$ – $400$   $\text{cm}^{-1}$ ) is also shown on the lower right. TCI: tochilinite-cronstedtite intergrowth and CM: carbonaceous material.

small vesicles inside was also present in the matrix of carbonaceous material. The mean RID values of carbonaceous material matrix and tabular object indicate densities of  $\sim 0.91$   $\text{g}/\text{cm}^3$  and  $\sim 1.06$   $\text{g}/\text{cm}^3$ , respectively (Table 1), clearly showing that they are not graphite.

### 3.6. Inclusions in minerals

Pyrrhotite crystals sometimes contained pentlandite inclusions (Fig. 5A). Additional small bright inclusions were also observed; however, we could not discriminate the phase (unknown in Fig. 5A) because they were observed only at 7 keV. These crystals usually have low-density inclusions, probably of pores, carbonaceous materials, or fluid inclusions. Most were small ( $< 1$   $\mu\text{m}$ ) and irregular in shape. Elongated inclusions or tubes connected to the outside, nearly parallel to the pseudo-hexagonal flat face, were also observed (a in Fig. 5A). Some have two different contrasts in an inclusion (lower right panel of Fig. 5A); brighter and darker contrasts correspond to carbonaceous materials (possibly IOMs) and pores, respectively. We found  $\text{CO}_2$ -bearing fluid in a relatively large inclusion (a few  $\mu\text{m}$ ) (b in Fig. 5A) by TOF-SIMS in C0002-FC012 (Nakamura et al., 2023). Many inclusions with darker contrast might be empty, even if they used to be occupied by fluid.

Mineral inclusions were not observed in the magnetite crystals. Only inclusions observed in some spherulites (Fig. 6B), plaquettes (Fig. 6D and E), framboid resembling colloidal crystals (Fig. 6F), relatively large crystals in framboids (n in Fig. 6H), and complex crystals (Fig. 6C, K, and L) have low contrast and are likely pores. One magnetite plaquette contained inclusions filled with low-density materials (i in Fig. 6E). No pore inclusions were observed in coarse equant grains (Fig. 6I). Dobricá et al. (2023) found abundant nanopores with facets and dislocations in a spherulite using TEM. These nanopores were too small to be identified by XnCT.

Dolomite crystals usually contain mineral inclusions of magnetite (spherulite, framboidal, and plaquette), pyrrhotite, and apatite (Fig. 8A). Abundant low-density inclusions were also observed (Fig. 8A and C). These are probably pores and/or carbonaceous materials and not fluid inclusions. Yabuta et al. (2023) reported organic matter in carbonate grains based on STEM-electron energy loss spectroscopy (EELS)–EDS analysis. A large pore space with facets open to the crystal surface is also observed (Fig. 8B).

Small mineral grains appear to be included in apatite in 2D, but they connect to the crystal surface in 3D (e.g., pyrrhotite, c in Fig. 9A). Low-density inclusions, probably pores and/or carbonaceous materials, were

also observed in apatite (Fig. 9A).

Brunnerite contains inclusions of magnetite (spherulite and framboid), pyrrhotite, and apatite (Fig. 10A), and low-contrast inclusions. Relatively large inclusions in A0067-FC003 and A0067-FC004 were examined using micro-Raman spectroscopy. These inclusions were IOMs and pores, and no fluid was detected (Supplementary Material, S10 and Fig. S9). No inclusions were observed in the Mg-Na phosphate phase.

The observed inclusions were primary, and no secondary inclusions distributed in a planar pattern were observed. The included relation among minerals is summarized in Table 3.

### 3.7. Specific textural relationships among minerals and magnetite morphologies

We examined specific textural relationships among mineral phases in 3D, where a convex grain of a mineral is surrounded by a concave surface of another mineral grain, suggesting that the convex grain grew earlier than the grain with a concave surface. These relationships are summarized in Table 3, along with the relationship between inclusions. The other mineral grains were not surrounded by magnetite. Among magnetite grains with different morphologies, spherulites were surrounded by plaquettes (f in Fig. 6D), framboids (a in Fig. 14A), irregular magnetite (b in Fig. 6A), and dolomite (a in Fig. 6A and c in Fig. 14C). A pre-existing spherulite appears to restrict the growth of a rod-shaped magnetite (b in Fig. 14B). The framboids were surrounded by pyrrhotite (e in Fig. 14D), dolomite (d in Fig. 14C), and brunnerite (a in Fig. 10A). Exceptionally, a small grain of pyrrhotite appears to be surrounded by framboids (m in Fig. 6G). Rods are surrounded by irregularly shaped magnetite, and the irregulars are surrounded by dolomite (o in Fig. 6K). The equants were surrounded by dolomite.

The pyrrhotite grains were surrounded by apatite (c in Fig. 9A), and the growth of dolomite appeared to be restricted by pre-existing pyrrhotite (f in Fig. 14E). The apatite grains are surrounded by dolomite (g in Fig. 14F). Dolomite grains were surrounded by coarse phyllosilicate aggregates (h in Fig. 14G) and brunnerite. A small dolomite grain with facets was also surrounded by Fe-bearing olivine or low-Ca pyroxene ( $\text{Fo}_{85}$  or  $\text{En}_{75}$ ) (a in Fig. 11B). Based on the detailed observation of the CT images in 3D, we can rule out the possibility that small grains of olivine or low-Ca pyroxene were reassembled to surround the dolomite grain and that the dolomite replaced part of the olivine or low-Ca pyroxene grains. The euhedral shape with macro growth steps of the grain (Fig. 11B) strongly suggests that it precipitated from the aqueous

**Table 3**  
Textural relationships among minerals and magnetite morphologies.

	Sph	Plaq	Frm	Rod	Irg	Eq	Pen	Po	Ap	Dol	Brn	c-PS	Ol/Px
Magnetite													
Spherulite (Sph)	—	Sur*	Sur	Sur	Sur			Sur		Inc**	Inc/Sur		
Plaquette (Plq)		—								Inc			
Framboidal (Frm)			—					Sur		Inc/Sur	Inc/Sur		
Rod (Rod)				—	Sur								
Irregular (Irg)					—					Sur			
Equant (Eq)						—				Inc/Sur			
Pentlandite (Pen)							—	Inc					
Pyrrhotite (Po) (pseudo-hexagonal)								—	Inc/Sur	Sur	Inc		
Apatite (Ap)									—	Sur	Inc		
Dolomite (Dol)										—	Sur	Sur	Sur
Breunnerite (Brn)											—		
Coarse phyllosilicate (c-PS)												—	
Olivine (Fo85) or pyroxene (En75) (Ol/Px)													—
Carbonaceous material									Inc	Inc			
Void									Inc	Inc			

\*Spherulite is surrounded by plaquette.

\*\* Spherulite is included in dolomite.

Abbreviations of magnetite morphologies and minerals (e.g., Sph) in the first line are given in the first column.

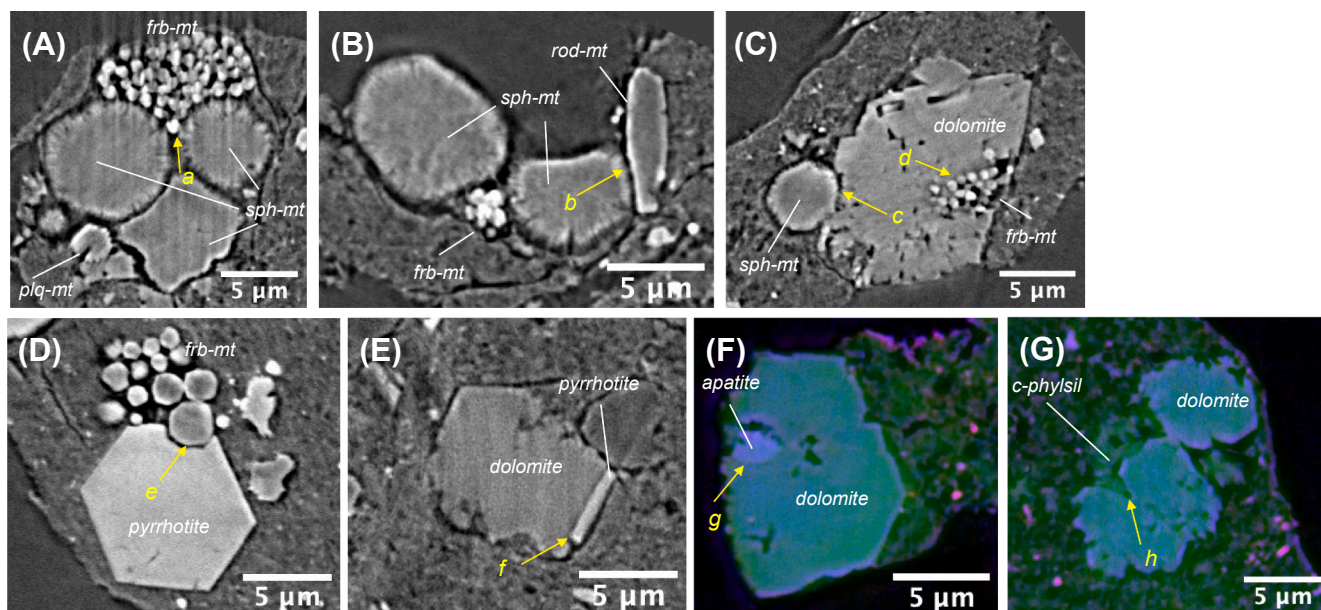


**Fig. 14.** CT images showing textural relationships among the minerals. (A) LAC 7 keV image ( $-200\text{--}600\text{ cm}^{-1}$ ) of C105-04300900. a: Spherulitic magnetites (sph-mt) surrounded by framboidal magnetites (frb-mt). (B) LAC 7 keV image ( $-200\text{--}600\text{ cm}^{-1}$ ) of C105-04300900. b: The growth of rod-shaped magnetite (rod-mt) appears to be restricted by pre-existing spherulitic magnetite (sph-mt). (C) LAC 7 keV image ( $-200\text{--}600\text{ cm}^{-1}$ ) of C105-04300900. c and d: Spherulitic magnetite (sph-mt) and framboidal magnetites (frb-mt) surrounded by dolomite, respectively. (D) LAC 7 keV image ( $-200\text{--}600\text{ cm}^{-1}$ ) of C105-04300400. e: Framboidal magnetites (frb-mt) surrounded by pyrrhotite. (E) LAC 7 keV image ( $-200\text{--}600\text{ cm}^{-1}$ ) of C105-04300500. f: The growth of dolomite appears to be restricted by pre-existing pyrrhotite. (F) RGB CT image of C105-04300200. g: Apatite surrounded by dolomite. (G) RGB CT image of A0063-FC0005. h: Dolomite surrounded by coarse phyllosilicates (c-phylsil).

solution after dolomite precipitation.

### 3.8. Foliation and lineation

Some mineral grains have elongated shapes (magnetite rods and whiskers) or plate-like shapes (mostly pyrrhotite). Some fine magnetite grains were present in the veins. We examined foliation or lineation due to these mineral grains or magnetite veins in 3D, but no such structures were observed. The distribution of these mineral grains and magnetite veins was also unrelated to cracks parallel to the flaky particles.

## 4. Discussion

### 4.1. Ryugu samples

The present results on mineralogy and 3D texture are consistent with previous studies where the Ryugu samples correspond to CI chondrites or CI-related materials and features without terrestrial weathering (such as Mg-rich phyllosilicates, the presence of Fe(-Ni) sulfide nanograins, and the absence of corroded pyrrhotite, sulfates, and ferrihydrite). Space weathering products were also observed, including melt splashes on the particle surfaces.

The microporosity of the particles and nanoporosity of the matrix were estimated to be approximately 12 % and 36 %, respectively. Nakamura et al. (2022) estimated the macroporosity of the Ryugu

sample to be about 41 %, which is larger than the present value. However, the volume and particle density used for their estimation had large errors and may have been overestimated. On the other hand, the present value would be underestimated because large cracks and voids were not taken into consideration for the small particles ( $\leq 100 \mu\text{m}$ ) used in this study. The CI porosity ranges from 35.0 % (Consolmagno and Britt, 1998) to 23.6 % (Hildebrand et al., 2006). Because these were measured by He pycnometry, they can be considered the sum of the macroporosity and nanoporosity. Since the nanoporosity in this study is limited to the matrix (considering the mode of the matrix as 82 %; Table 1), the corresponding value for porosity measured by He pycnometry should be approximately 40 %, which is slightly larger than the CI values. However, as CIs are subject to terrestrial weathering, direct comparison is not possible. The porosities in the present study had large errors, and more precise measurements are required in the future.

Nakamura et al. (2023) classified the lithologies of the Ryugu samples based on their mineral assemblages in relation to the aqueous alteration degree as follows: least-altered, less-altered, and highly-altered major lithologies. They found amorphous silicate objects that contained abundant nanograins of Fe sulfides in the least-altered lithology. These textures and compositions are similar to those of glass with embedded metal sulfides (GEMS) in anhydrous chondritic interplanetary dust particles (IDPs) (e.g., Bradley, 1994), but do not contain nanograins of Fe-Ni metal, and thus are called GEMS-like objects. More abundant olivine and low-Ca pyroxene grains and Fe-Ni phosphide were also observed in the least-altered lithology than in the other lithologies, and such features were not observed in the CI chondrites. CI chondrites before terrestrial weathering would correspond to the highly altered major lithology.

Other primitive materials that were not observed or were rare in the CIs were also found in the Ryugu samples. Chondrules are apparently absent in the CIs (Nakashima et al., 2023). Only a single CAI has been reported in a CI chondrite (in Ivuna by Frank et al., 2023). In contrast, chondrule-like objects and multiple CAIs have been found in Ryugu samples (Nakamura et al., 2023; Nakashima et al., 2023). We found magnetite whiskers, which were not observed in the CIs, in the highly-altered major lithology. This may have been formed by direct precipitation from the aqueous solution under specific conditions or by the replacement of whisker crystals formed by gas condensation, such as enstatite whiskers observed in anhydrous chondritic IDPs (Bradley et al., 1983).

The Ryugu samples contained two unique particles. One is calcite and phyllosilicate grains embedded in a matrix composed of  $\text{Al}_2\text{Si}_2\text{O}_5(\text{OH})_4$  (kaolinite, nacrite, or dickite) (A0104-00001500; Fig. 13B). Calcite and the kaolinite group mineral were determined using TEM (Fig. S8). Calcite and kaolinite are stable phases in a chemical equilibrium calculation model that attempts to reproduce the observed aqueous alteration assemblage of the Ryugu samples (Nakamura et al., 2023) although the stable ranges of the water/rock ratio are different: 0.12 ~ 0.3 for calcite and  $> \sim 1$  for kaolinite. The calcite and  $\text{Al}_2\text{Si}_2\text{O}_5(\text{OH})_4$  assemblage might be explained by the reaction of Ca-, Al-, and Si-rich minerals (e.g., anorthite, gehlenite, and kushiroite) with  $\text{CO}_2\text{-H}_2\text{O}$  liquid (or fluid) during aqueous alteration.

The other was an aggregate of  $\text{CaCO}_3$  (calcite or aragonite), phyllosilicate, TCI, and carbonaceous material (possibly IOM) (C0076-FC001; Fig. 13C). This mineral assemblage is not consistent with the equilibrium model for Ryugu but is similar to that of the majority of Migheitype carbonaceous chondrites (CM chondrites). However, the two types of carbonaceous materials (matrix and tabular materials with slightly different densities;  $\sim 0.91$  and  $\sim 1.06 \text{ g/cm}^3$ , respectively) and their large abundance are unique, even for CMs. Tochilinite was observed in the least-altered lithology (Nakamura et al., 2023), indicating that the aqueous alteration of Ryugu samples begun under CM-like conditions. However, the origin of the CM-like materials is unknown, and further analysis is required.

We cannot completely exclude the possibility of contamination for

these unique samples. However, many minerals and objects (calcite, phyllosilicate, pseudomorphs of Mg-rich silicates, tochilinite, and carbonaceous materials) were found in Ryugu samples. Furthermore, we do not know of any other materials that are similar to these unique samples. Kaolinite has been reported in aqueously-altered CAIs in the Allende meteorite (CV3) (Che and Brearley, 2021) and a chondritic porous interplanetary dust particle (Rietmeijer and Mackinnon, 1985).

#### 4.2. Lithology and its heterogeneity of the present samples

The mineral assemblages and textures are essentially the same among the samples belonging to the “matrix” category and correspond to the highly-altered major lithology of Nakamura et al. (2023). We obtained two particles containing olivine or low-Ca pyroxene grains. The one containing Mg olivine or low-Ca pyroxene (A0104-00000500; Fig. 11A) may belong to the less-altered lithology, but the olivine or pyroxene abundance is very small, and the matrix is similar to that of the major lithology. Fo<sub>85</sub> olivine (or En<sub>75</sub> pyroxene) in the other particle could be an aqueous alteration product as already mentioned (A0063-FC010; Fig. 11B). Therefore, we did not observe the least- and less-altered lithologies in this study.

The sample had heterogeneities among the particles and in single particles on the scale of  $< \sim 30 \mu\text{m}$ , as shown in Figs. 3, 4, and S-2 and A0104-00000300 in Table 1, even though they belong to the major lithology. Some of the boundaries between objects with different colors in the RGB-CT images (e.g., c, d, and e in Fig. 3) may indicate clasts, but most of the boundaries are ambiguous, indicating that such heterogeneity with different porosities and chemical compositions (e.g., Mg#) was originally present before aqueous alteration.

It is expected that surface materials contain a higher number of space-weathered particles than subsurface materials from Chamber C (Noguchi et al., 2023a). Melt splashes can be observed on the surfaces of space-weathered particles, provided that they are large enough for XnCT resolution (Fig. 12A). However, the number of particles that have melt splashes (or their candidates) from Chambers A and C exhibited the opposite trend: three from Chamber A (A0104-00001200, A0104-00001900, and A0104-00002100) and eight from Chamber C (C0046-FO015, C0061-FC005, C0105-04300100, C0105-04300500, C0105-04300500, C0105-04300600, C0105-04300800, and C0105-04300900). This was likely due to a sampling bias. No clear difference was observed in the internal textures of the samples from Chambers A and C.

#### 4.3. Precipitation sequence

The major minerals in the matrix (pyrrhotite, magnetite, dolomite, apatite, and breunnerite) have crystal shapes with facets and should have precipitated from aqueous solutions together with phyllosilicates during aqueous alteration (e.g., Nakamura et al., 2023). The precipitation sequence was obtained from the textural relationships between these minerals. For example, magnetite spherulites were included in dolomite grains (Fig. 8A), indicating that the spherulites precipitated prior to dolomite precipitation. The textural relationships are essentially common among minerals and magnetite morphologies (Table 3) with exceptions (e.g., pyrrhotite surrounded by framboidal magnetite; m in Fig. 6G). This suggests that the precipitation sequence was basically magnetite (spherulite  $\rightarrow$  plaquette/framboid  $\rightarrow$  rod/equant)  $\rightarrow$  pyrrhotite (pentlandite  $\rightarrow$  pyrrhotite)  $\rightarrow$  apatite  $\rightarrow$  dolomite  $\rightarrow$  breunnerite (Fig. 15) although precipitation at overlapping times occasionally occurred. Coarse phyllosilicates and Fe-bearing olivine/low-Ca pyroxene probably formed later than dolomite. The Mg-Na phosphate phases showed no inclusions and may have precipitated earlier. However, the grain shapes of this phase were irregular, and cracks were consistently present between the matrix attached to this phase (b in Fig. 10B). Cracks were also observed between the phosphate grains and matrix in the SEM image of a larger particle cross-section, with the grains (20–50  $\mu\text{m}$  wide

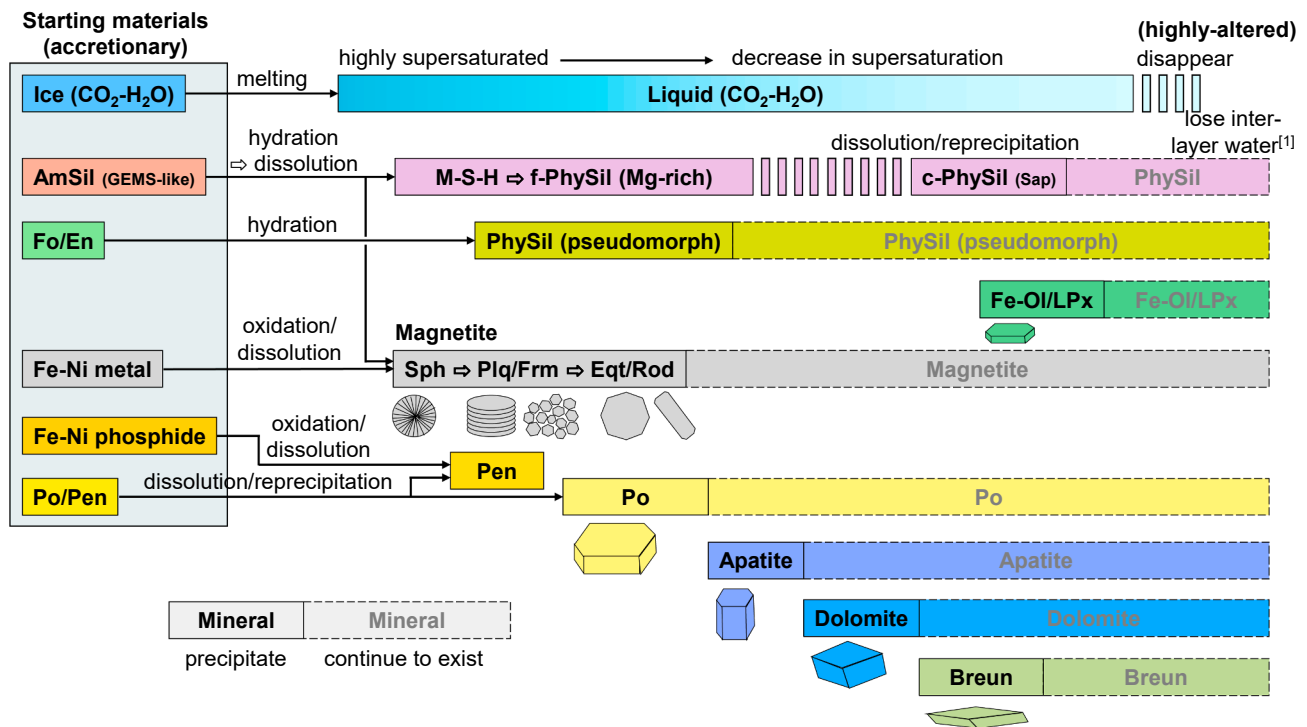


**Fig. 15.** Schematic illustration of the aqueous alteration model, including starting materials and precipitation sequence. In this illustration, only the starting materials as accretionary materials and the final products as the highly-altered lithology are shown. CO<sub>2</sub> in dolomite and breunnerite is from ice, Ca in apatite and dolomite from amorphous silicates, Mg in dolomite and breunnerite from amorphous silicates, forsterite, and enstatite, and P in apatite from Fe-Ni metal and Fe-Ni phosphide. AmSil: amorphous silicates, Fo, forsterite, En: enstatite, Po: pyrrhotite, Pen: pentlandite, M-S-H: Mg silicate hydrate, PhySil: phyllosilicates (f: fine, c: coarse), Sap: saponite, Fe-Ol: Fe-bearing olivine, LPx: low-Ca pyroxene, Sph: spherulitic magnetite, Plq: plaquette magnetite, Frm: framboidal magnetite, Eqt: equant magnetite, Rod: rod magnetite, Breun: breunnerite. [1] Yokoyama et al. (2022) and Nakamura et al. (2023).

and 50–150  $\mu\text{m}$  long) appearing to be distributed along the cracks present throughout the entire particle (Fig. S9 in Nakamura et al., 2023). Therefore, it could be the last phase to precipitate in the relatively large voids, and the timing of the precipitation is uncertain.

Carbonaceous materials, most likely including IOMs, were present before pyrrhotite precipitation. This is consistent with the proposal that the organic matter (IOMs) in Ryugu likely comprises primordial materials that formed during (or before) the early stages of the Solar System formation, which were subsequently modified by heterogeneous aqueous alteration on the Ryugu parent body (Yabuta et al., 2023).

Magnetites from CI chondrites have been considered as early phases in aqueous alteration based on their high  $\Delta^{17}\text{O}$  values (Rowe et al., 1994; Leshin et al., 1997). For the Ryugu samples, the precipitation sequence of magnetite and carbonates was estimated based on their  $\Delta^{17}\text{O}$  values as magnetite  $\sim$  calcite  $\rightarrow$  dolomite  $\rightarrow$  breunnerite (Fujiya et al., 2023; Kita et al., 2024). Higher  $\Delta^{17}\text{O}$  values of spherulitic magnetites than those of equant magnetites suggest that the spherulites formed earlier than the equants (Kita et al., 2024). The  $\Delta^{17}\text{O}$  values of magnetites with different morphologies from hydrated fine-grained Antarctic micrometeorites (AMMs) suggest a precipitation sequence of spherulite  $\rightarrow$  framboid/subhedral  $\rightarrow$  plaquette (Dobrică et al., 2019). These sequences for both Ryugu and CIs are consistent with those proposed in this study, suggesting that the model for oxygen isotopic evolution assuming Rayleigh-type fractionation is correct.

Aggregates of fine magnetite grains with a shape resembling that of pseudo-hexagonal pyrrhotite have been reported in the CIs (Alfing et al., 2019), suggesting the subsequent oxidation of pyrrhotite to form magnetite. However, their observations were made only in 2D and their hexagonal shape in 3D was not verified. We did not observe such aggregates in this 3D observation. It is likely that these were aggregates of framboidal magnetite, such as framboids resembling colloidal crystals (e.g., Fig. 6F), which were incidentally observed as hexagonal

pseudomorphs in 2D. However, this alteration assemblage has been observed in C1 lithologies in the Kaidun meteorite (M. Zolensky, personal communication). Fe-(Ni) sulfides were replaced by ferrihydrite and proposed that these are aqueous alteration products (Tomeoka and Buseck, 1988; Bullock et al., 2005). However, we did not observe any objects composed of ferrihydrite, which is a terrestrial weathering product.

Mg-rich olivine and low-Ca pyroxene observed in the less-altered lithology were considered to be the primary minerals that survived aqueous alteration (Nakamura et al., 2023). Kawasaki et al. (2023) found that primary olivine (and low-Ca pyroxene) in the Ryugu samples and CIs, are divided into <sup>16</sup>O-rich ( $\Delta^{17}\text{O} \sim -23\text{‰}$ ) and <sup>16</sup>O-poor ( $\Delta^{17}\text{O} = -7 \sim 0\text{‰}$ ), and claimed that they originate from ameboidal olivine aggregates (AOAs) and chondrules, respectively. Most of these are rich in Mg (Mg# > 0.97), except for some of the <sup>16</sup>O-poor ones (Mg#  $\sim$  0.6–0.9). The Mg olivine (or low-Ca pyroxene) found in the present study corresponds to the primary olivine. On the other hand, the Fe-bearing olivine (or low-Ca pyroxene) (Fo<sub>85</sub> or En<sub>75</sub>) should be a secondary mineral formed by aqueous alteration (Fig. 11B) based on the 3D texture, as mentioned earlier. Therefore, not only primary olivine (and low-Ca pyroxene), but also secondary olivine would exist in the aqueously-altered lithologies, although their abundance is low. While fayalite (Fa<sub>95-98</sub>) produced by aqueous alteration is known for CO3 and CV3 chondrites (Krot et al., 2000, 2022), Mg-rich olivine produced by aqueous alteration has not yet been reported. Aqueous alteration in Ryugu and possibly in the CIs would have produced Mg-rich olivine, suggesting high Mg activity in the fluid. To confirm this, the oxygen isotopic composition should be measured.

#### 4.4. Formation and evolution of the main lithology of the Ryugu sample: a model for aqueous alteration in Ryugu parent body

Here, we propose a model for the aqueous alteration in the Ryugu parent body based on our observations, the mineralogy in the least-altered lithology (Nakamura et al., 2023) as the starting materials, and the mineralogy and precipitation sequence for the alteration processes (Table 3). A schematic illustration of this model, discussed in detail below, is shown in Fig. 15.

GEMS-like materials composed of amorphous silicates and Fe sulfide nanograins, Fe-Ni metal, Fe-Ni phosphide, olivine, and low-Ca pyroxene were observed in the least-altered lithology (Nakamura et al., 2023). The CO<sub>2</sub>-bearing fluid inclusions observed in pyrrhotite are aqueous fluids incorporated into growing pyrrhotite crystals during their growth (Nakamura et al., 2023). Brunetto et al. (2023) show that the least-altered lithologies have infrared spectra similar to the D-type asteroid Hektor (a Jupiter Trojan), to comet Hale-Bopp, and to some anhydrous chondritic interplanetary dust particles of probable cometary origin. Therefore, we assume that the Ryugu parent body formed beyond Jupiter's orbit by accretion of CO<sub>2</sub>-H<sub>2</sub>O ice, GEMS-like materials, Fe-Ni metal, Fe(-Ni) sulfide, Fe-Ni phosphide, olivine, low-Ca pyroxene, and organic materials (e.g., IOMs). Amorphous silicates in GEMS-like materials serve as sources not only for the major elements Mg, Fe, and Si but also for less abundant lithophile elements like Ca. P-bearing Fe-Ni metal (with P originally condensed into the metal) and Fe, Ni phosphides were the sources of P, which underwent oxidation through reactions with water.

Aqueous alteration started with the melting of CO<sub>2</sub>-H<sub>2</sub>O ice (Fig. 15), which might have been caused by radiogenic or impact heating. The temperature of the aqueous alteration was proposed to be ~40°C based on the oxygen isotope compositions of dolomite-magnetite pairs (Yokoyama et al., 2022). The estimated diameter of the Ryugu parent body of <~100 km (Nakamura et al., 2023) indicates a pressure of <~50 bar. CO<sub>2</sub>-bearing H<sub>2</sub>O (e.g., CO<sub>2</sub>/H<sub>2</sub>O = 0.08 by Nakamura et al., 2023) under these conditions are not “fluid” above the critical point but “liquid” based on the phase diagram of CO<sub>2</sub>-H<sub>2</sub>O (Longhi, 2005).

Amorphous silicates in GEMS-like materials easily react with the liquid to form an aqueous solution (Fig. 15), which is highly supersaturated with hydrous Mg-rich phyllosilicates (serpentine and saponite) and Mg silicate hydrate (M–S–H), which is a semi-amorphous Mg-silicate phase with characteristic broad peaks observed by XRD but without specific Mg/Si ratio and structure (e.g., Roesz et al., 2015) because amorphous silicates have high reactivity owing to their higher free energy than crystalline phyllosilicates and M–S–H (e.g., Bernard et al., 2017; Igami et al., 2021). A poorly crystallized, phyllosilicate-like phase, M–S–H, with two weak rings of *d* spacings of ~0.15 and ~0.25 nm in SAED pattern is reported in the matrix of a primitive carbonaceous chondrite (Acfer 094) (Matsumoto et al., 2019) and a similar phase is also reported in the GEMS-like material in the Ryugu sample (Nakamura et al., 2023). In natural samples, such an M–S–H-like phase would contain some Fe replacing some of the Mg. This aqueous solution should also have become highly supersaturated with Fe oxide minerals such as magnetite because of the Fe component in the amorphous silicate (e.g., Mg/(Mg + Fe) = Mg# = 0.65 ~ 0.9, for GEMS-like material in the Ryugu samples; Nakamura et al., 2023) and the reaction with metal and probably some Fe(-Ni) sulfides (in particular, nanograins in GEMS-like material). Mg-rich phyllosilicates (as M–S–H and poorly crystallized phyllosilicates) and magnetite (in the form of spherulites) were formed from a highly supersaturated solution generated by the reaction of slightly Fe-rich amorphous silicates and metallic iron (possibly with some iron sulfide) with water. This process can be explained by chemical equilibrium calculations considering the aqueous alteration of materials with CI compositions. In these calculations, Mg-rich serpentine and magnetite are stable at water/rock ratios (W/R) of approximately 0.2 to 0.9, which corresponds to the conditions observed in the Ryugu samples. As the W/R ratio increases, serpentine becomes Fe-rich and magnetite disappears (Nakamura et al., 2023).

TEM observations indicate that the matrix in the highly altered major lithology is mainly composed of two materials: (1) poorly-crystallized fine phyllosilicates (fine matrix), and (2) coarse phyllosilicates (coarse matrix) (Matsumoto et al., 2024). The fine matrix contained Fe(-Ni) sulfide nanograins, whereas the coarse matrix was not abundant in the Fe(-Ni) sulfide nanograins. Both types of matrices were porous with different porosities, and there appeared to be no clear porosity difference between the fine and coarse matrices. Because the spatial resolution of TEM and XnCT images is different, the fine and coarse matrices observed in TEM are probably not clearly distinguishable in XnCT, except for the coarse phyllosilicate veins (e.g., b in Fig. 3B). However, because the dark and bright green matrices in XnCT have low and high densities, respectively, if both are composed of solid materials with approximately the same density, the former is more porous, and the latter is less porous. Taking this into account, together with the distribution of Fe(-Ni) sulfide nanograins, where the nanograins tend to be abundant in the dark green matrix and fine matrix, some of the dark green matrix would correspond to fine matrix, while whereas the bright green matrix would correspond to fine and coarse matrices. M–S–H and poorly crystallized fine phyllosilicates formed first from the highly supersaturated solution (Fig. 15). This process occurred because the dissolution of amorphous silicates (GEMS-like material) was rapidly followed by the precipitation of M–S–H and fine phyllosilicates, as observed in the in-situ aqueous alteration experiments by Igami et al. (2021). Coarse phyllosilicates were later formed, as discussed below.

Magnetite crystals of very fine-grained aggregates (spherulites, plaquettes, and framboids) were first precipitated from a highly supersaturated solution. These crystals have high surface area/volume ratios and thus high surface/bulk energy ratios and are considered to crystallize under high degrees of supersaturation or conditions of high Péclet number ( $Pe = LR/D$ , where  $L$  is the characteristic length of the system,  $R$  is the growth rate, and  $D$  is the diffusion coefficient) for growing crystals, resulting in the morphological instability of Mullins-Sekerka (Mullins and Sekerka, 2004). Hereafter, we refer to crystals of such morphologies as “irregularly-shaped crystals” and relatively coarse crystals with facets and low surface area/volume ratios as “regularly-shaped crystals.” In fact, spherulites were the first magnetite aggregates to precipitate based on XnCT observations (Table 3 and Fig. 15). TEM studies of some spherulites, including abundant nanosized pore inclusions, have also revealed non-equilibrium crystallization products (Dobricá et al., 2023). The dissolution of relatively Fe-rich amorphous silicate in the GEMS-like material (Mg# = 0.65 ~ 0.9) and precipitation of relatively Mg-rich fine silicates (Mg# ~ 0.85; Nakamura et al., 2023; Noguchi et al., 2023b) made the aqueous solution more supersaturated with respect to magnetite. Based on the XnCT observations (Table 3), plaquettes and framboids were the next magnetite aggregates to precipitate (Fig. 15). This is consistent with the surface area/volume ratios of plaquettes and framboids, which should be smaller than spherulites.

The degrees of supersaturation for phyllosilicates and magnetite in the aqueous solution were decreased by the precipitation of fine phyllosilicates (and M–S–H) and irregularly-shaped crystals of magnetite, respectively. Similarly, the degrees of supersaturations for apatite, dolomite, and breunnerite were lowered by the precipitation of phyllosilicates and magnetite. This reduction occurred because the amounts of Ca for apatite and dolomite, and Mg in dolomite and breunnerite in the aqueous solution, were decreased by phyllosilicate precipitation, while the amount of Fe for breunnerite was decreased by magnetite precipitation. Mineral grains of regularly-shaped crystals (equant and rod magnetite, pyrrhotite, apatite, dolomite, and breunnerite) precipitated under low degrees of supersaturation from the aqueous solution or under conditions of low  $Pe$  without morphological instability. If water escapes during aqueous alteration, such as through evaporation, the degree of supersaturation increases. The present findings, where the crystal shape of the mineral that precipitated later corresponds to a lower supersaturation, suggest that water escaped after the aqueous alteration was almost complete.

For magnetite, the morphological change to equant and/or rod would be sequential because there are transitional morphologies between the irregular and euhedral morphologies (e.g., Fig. 6C, E, K, and L). It is likely that the dissolution of magnetite crystals with higher surface energy and the reprecipitation of those with lower surface energy occurred during aqueous alteration (Ostwald ripening). However, we still do not know the detailed conditions for the different morphologies, including the fine cubes (Fig. 6M) and whiskers (Fig. 7), such as the minor elemental composition, pH, and/or temperature of the aqueous solution, interaction with phyllosilicates and/or organic materials, and magnetic field. Magnetite grains with different morphologies sometimes coexisted (Fig. 6D and 6E, 14A, and 14B). This may suggest that conditional changes occurred at the same location.

In contrast to magnetite, pyrrhotite appears almost exclusively as pseudo-hexagonal plates of different sizes (Fig. 5A and Fig. S7), except for the Fe(-Ni) sulfide nanograins in the matrix. The key difference from magnetite is the existence of pyrrhotite as Fe(-Ni) sulfide nanograins at the onset of aqueous alteration. Nucleation of pyrrhotite was not necessary since it grew from pre-existing nanograins. The growth of a pseudo-hexagonal plate with relatively low surface energy does not require large supersaturation, owing to the dissolution and reprecipitation of pyrrhotite crystals via Ostwald ripening. This is consistent with the later precipitation of newly-formed pseudo-hexagonal crystals of pyrrhotite than that of irregularly shaped crystals of magnetite (Fig. 15). The precipitation order among regularly-shaped crystals of magnetite and hexagonal-shaped pyrrhotite is not known because we do not know any textural relationship between them (Table 3). Pentlandite occurs as an anhedral inclusion in pyrrhotite and as small, fragmented particles that are sometimes overgrown by pyrrhotite (Fig. 5A, D, and E, respectively). At least, the separated pentlandite grains may have been formed by replacing some Ni-bearing minerals, such as schreibersite ((Fe,Ni)P<sub>3</sub>), present before aqueous alteration, and some of them were later overgrown by pyrrhotite. We cannot exclude the possibility that some pentlandite inclusions in pyrrhotite could have been formed by exsolution from pyrrhotite.

Apatite typically appears as aggregates of faceted crystals. Some resembled coarse dendritic aggregates (a and b in Fig. 9A). Simple euhedral crystals with hexagonal prisms (Fig. 9B), probably the equilibrium form, are rare. This suggests that many apatite crystals precipitated at relatively high supersaturation. Dolomite also appeared as aggregates of faceted crystals (Fig. 8A and B). However, euhedral crystals of flattened rhombohedra (Fig. 8C), probably as the equilibrium form, are not rare. Therefore, the degree of supersaturation of these dolomite crystals may be slightly lower than that of apatite crystals. Aggregates of fine dolomite grains in the matrix (Fig. S4E and S6) may have been an early product of precipitation. Breunnerite occurred as relatively large euhedral crystals with flattened rhombohedra (Fig. 10). This may suggest late crystallization under low-supersaturation conditions. The later precipitation of apatite, dolomite, and breunnerite than that of pyrrhotite can be explained by the nucleation needed for apatite, dolomite, and breunnerite rather than pyrrhotite. The precipitation order of these newly-formed phases appears to correspond to the difference in the degree of supersaturation, where the earlier phase (apatite) generally precipitated under higher supersaturation than the later phase (breunnerite) under lower supersaturation.

Coarse fibrous phyllosilicates in the coarse matrix (a, b, and f in Figs. 3A, B, and D, c in Fig. 4A, and h in Fig. 14G) were formed by the dissolution of fine phyllosilicates and their reprecipitation under low supersaturation conditions (Fig. 15), where the (Fe,Ni)S nanograins in the fine matrix changed to larger pseudo-hexagonal plates of pyrrhotite. The texture of the coarse fibrous phyllosilicates and dolomite grains (h in Fig. 14G) indicates that coarse phyllosilicates formed later than dolomite (Table 3). Olivine and low-Ca pyroxene with different Mg#s reacted with the aqueous solution to form objects composed of phyllosilicates having different brightness (from dark to bright green) without n(Fe,Ni)S (Fig. 4C, S4C, and S4D) as pseudomorphs. Some Fe-bearing

olivine or low-Ca pyroxene (e.g., Fo<sub>85</sub> or En<sub>75</sub>, Fig. 11B) precipitated later than dolomite, probably after the formation of coarse phyllosilicates due to later changes in aqueous alteration conditions with high Mg activities in the fluid although the cause is not clear.

Nakamura et al. (2023) calculated chemical equilibrium for the aqueous alteration and showed that the mineral assemblages in the different lithologies (least-altered, less-altered, and major strongly-altered) of Ryugu samples can be basically explained by this model with different water/rock ratios (W/R). However, equilibrium might not have been reached in the Ryugu samples as proposed by Nakamura et al. (2023), because the mineral assemblages in the Ryugu samples do not necessarily match those in the chemical equilibrium model, even with different W/R ratios. The kinetics may have controlled the precipitation sequence as discussed above. Since the difference between the three lithologies (least-altered, less-altered, and highly-altered) lies in W/R ratio, the precipitation sequence in the present highly-altered lithology cannot be directly applied to the least-altered and less-altered lithologies. However, it should be noted that apatite, dolomite, and breunnerite, which are the late-precipitated minerals in this model, are not found in the least-altered and less-altered lithologies (Nakamura et al., 2023).

Suttle et al. (2021) proposed a model for the aqueous alteration of CM chondrites, mainly based on the phases in the CM chondrite lithologies (CM2 and CM1). They assumed a theoretical CM3 lithology as the starting material for the alteration. This may correspond to the starting material of aqueous alteration in the Ryugu parent body (should be named theoretical CI3). Their mineral assemblages are almost the same, although the proportion of GEMS-like material to anhydrous silicates for CI3 is larger than that for CM3 because chondrules are rare to absent in the CIs and Ryugu samples. The evolution from CM3 to CM2 and CM1 corresponds to the evolution of the lithologies of Ryugu samples, from CI3 to least-altered (CI3/2?), less-altered (CI2?) and strongly altered major lithologies (CI1). As an analogy to the change in the mineral assemblage from CI3 to CI1, the change from CM3 to CM1 was not related to the precipitation sequence of minerals. The major difference between CM2 and CM3 from Ryugu samples is the presence of cronstedtite and tochilinite and the absence of saponite, which could be the result of aqueous alteration conditions (e.g., Brearley, 2006). However, a minor amount of tochilinite was present in the GEMS-like materials in Ryugu (Nakamura et al., 2023), suggesting that a CM-like condition was present at the beginning of aqueous alteration in the Ryugu parent body. The CM-like particles in the Ryugu samples (Fig. 13C) may be related, although the details are unknown.

## 5. Conclusions

Fine particles of Ryugu samples, 10–200 μm in size, were examined using X-ray nanotomography (XnCT). In this study, the 3D distribution of the mineral phases was obtained using combined dual-energy tomography (DET) and scanning-imaging X-ray microscopy (SIXM) (e.g., Matsumoto et al., 2022) with an effective spatial resolution of ~200 nm (Figs. 1 and 2). The mineralogy and petrology in 3D are consistent with those of previous studies on Ryugu samples (e.g., Yokoyama et al., 2022; Nakamura et al., 2022; Ito et al., 2022; Nakamura et al., 2023; Noguchi et al., 2023a) and similar to those of CI chondrites, where minerals such as pyrrhotite, magnetite, dolomite, breunnerite, and apatite are present in a matrix composed mainly of phyllosilicates (saponite and serpentine).

The 3D features of the constituents are as follows. (1) The matrix is heterogeneous (Figs. 3, 4, and S4) and roughly divided into two areas: fine phyllosilicates with abundant Fe(-Ni) sulfide nanograins and relatively coarse phyllosilicates with poor Fe(-Ni) sulfide nanograins, together with objects that appear to be pseudomorphs of anhydrous ferromagnesian minerals (e.g., olivine and low-Ca pyroxene) with different Fe/Mg ratios. These features are largely consistent with TEM observations (Matsumoto et al., 2024). (2) Almost all pyrrhotite crystals of 1–60 μm appear as pseudo-hexagonal plates (probably a combination of {100} and {001}) (Fig. 5A and Fig. S7). The Fe(-Ni) sulfide

nanograins in the matrix have irregular shapes. (3) Magnetite shows a large variety of morphologies from irregular shapes (spherulite, plaquette, and framboid) to regular shapes (equant ( $\{311\}$ ) and rod (elongated in  $\langle 100 \rangle$ )) (Fig. 6). Composite morphologies transitional from irregular to regular shapes were also observed. Magnetite whiskers (elongated in  $\langle 100 \rangle$ ) (Fig. 7) and fine-grained cubes (Fig. 6M) were also observed. (4) Dolomite ( $< \sim 60 \mu\text{m}$ ) (Fig. 8), breunnerite (30–60  $\mu\text{m}$ ) (Fig. 10), and apatite ( $< \sim 10 \mu\text{m}$ ) (Fig. 9) exhibit rhombohedral shapes (probably  $\{104\}$ ), more flattened rhombohedrons, and hexagonal prisms (combination of  $\{100\}$  and  $\{001\}$ ), respectively). Dolomite and apatite usually appear as aggregates of euhedral to subhedral crystals with facets. Apatite sometimes shows dendrite-like features, and a simple hexagonal prism is rare. (5) Unique objects were also observed. One is an Fe-enriched clast with irregular shapes ( $\sim 10 \mu\text{m}$ ), composed of relatively Fe-rich anhydrous silicate and probably fine grains of Fe(-Ni) sulfide (Fig. 1D, 3C (c), and 12A). The others are very porous objects with irregular shapes ( $\sim 5 \mu\text{m}$ ) (Fig. 12B), which might be similar to the ultra-porous lithology (UPL) in Acfer 094 (Matsumoto et al., 2019), and which experienced severe aqueous alteration. A relict of a barred olivine chondrule ( $\sim 30 \mu\text{m}$  in diameter) that underwent aqueous alteration has been observed as reported by Nakamura et al. (2023). Fe-rich glasses with vesicles, corresponding to melt splash on the particle surface, were also observed (e.g., Fig. 12C).

Mineral inclusions were observed in 3D (Table 3). The pyrrhotite crystals contained aqueous fluid inclusions (Nakamura et al., 2023), carbonaceous materials (possibly IOMs), pentlandite, and voids (Fig. 5). Dolomite (Fig. 8) has magnetite inclusions, breunnerite (Fig. 10) has magnetite, pyrrhotite and apatite inclusions, and apatite (Fig. 9) has pyrrhotite inclusions (Table 3). These minerals also contained carbonaceous materials and void inclusions. The textural relationships among the minerals, including magnetite morphology, were also examined in 3D (e.g., Fig. 14) and are summarized in Table 3. Based on these textural relationships, the precipitation sequence for the aqueous alteration was as follows: magnetite (spherulite  $\rightarrow$  plaquette/framboid  $\rightarrow$  equant/rod)  $\rightarrow$  (pentlandite  $\rightarrow$ ) pyrrhotite  $\rightarrow$  apatite  $\rightarrow$  dolomite  $\rightarrow$  breunnerite. A small dolomite grain surrounded by euhedral Fe-bearing olivine or low-Ca pyroxene ( $\text{Fo}_{85}$  or  $\text{En}_{75}$ , Fig. 11C) suggests that some Fe-bearing olivine or pyroxene crystallized after the dolomite.

Based on the precipitation sequence and the mineral morphologies examined in this study, together with observations of the least-altered lithology of Ryugu samples (Nakamura et al., 2023), a model for aqueous alteration in the Ryugu parent body was proposed (Fig. 15).

- (1)  $\text{CO}_2\text{-H}_2\text{O}$  ice, GEMS-like materials (relatively Fe-rich amorphous silicates with Fe(-Ni) sulfide nanoparticles), Fe(-Ni) sulfides, Fe-Ni metal, forsterite/enstatite, Fe, Ni-phosphide, and carbonaceous materials were aggregated to form the parent body of Ryugu.
- (2) The aqueous alteration was initiated by melting ice to form a  $\text{CO}_2$ -bearing aqueous liquid.
- (3) Amorphous silicates with extremely high reactivity, Fe(-Ni) sulfide nano-inclusions, and Fe-Ni metal quickly dissolve into the liquid to form a highly supersaturated aqueous solution of phyllosilicates and magnetite.
- (4) Magnesium silicate hydrate (M-S-H), a precursor of Mg-rich phyllosilicates, first precipitated from a highly supersaturated solution, followed by relatively Mg-rich fine-grained phyllosilicates and spherulitic magnetite.
- (5) The degree of supersaturation of magnetite decreased owing to precipitation, followed by plaquette/framboidal magnetites and the formation of coarse equant/rod magnetites. Relatively coarse-grained phyllosilicates also formed.
- (6) Fe(-Ni) sulfide was dissolved in the solution and pyrrhotite pseudo-hexagonal plates were reprecipitated under relatively low supersaturation.

- (7) At least some of pentlandite may be a pseudomorph after Fe-Ni phosphide and formed before pyrrhotite crystallization.
- (8) Subsequently, apatite, dolomite, and breunnerite precipitated in this order in response to decreasing supersaturation.
- (9) Phyllosilicate pseudomorphs after olivine and pyroxene formed. Coarse-grained phyllosilicates also formed.
- (10) Fe-bearing olivine or low-Ca pyroxene precipitated from an aqueous solution with high Mg activity in a later stage after dolomite precipitation.

The crystallization processes are largely affected by kinetics.

In addition to materials similar to CI chondrites, we observed two unique particles. One was an aggregate of calcite and  $\text{Al}_2\text{Si}_2\text{O}_5(\text{OH})_4$  (A0104-00001500) (Fig. 13B and Fig. S8). The other is an aggregate of  $\text{CaCO}_3$ , phyllosilicate, and tochilinite-cronstedtite intergrowth (TCI), embedded in the matrix of the carbonaceous materials (C0076-FO001) (Fig. 13C). These seem to be from Ryugu, although we cannot completely rule out the possibility of subsequent contamination. The former may be consistent with the CI mineralogy, while the latter corresponds to the CM2 mineralogy. However, we do not know their origin or relationship with the main CI or CI-like materials.

#### Data availability

Data are available through Mendeley Data at <https://data.mendeley.com/datasets/b2zg6dm5sm/1>.

#### CRediT authorship contribution statement

**Akira Tsuchiyama:** Writing – review & editing, Writing – original draft, Visualization, Validation, Project administration, Methodology, Investigation, Funding acquisition, Formal analysis, Data curation, Conceptualization. **Megumi Matsumoto:** Writing – review & editing, Writing – original draft, Methodology, Funding acquisition, Formal analysis, Data curation. **Junya Matsuno:** Software, Methodology, Funding acquisition, Formal analysis, Data curation. **Masahiro Yasutake:** Project administration. **Tomoki Nakamura:** Writing – original draft, Project administration, Formal analysis, Data curation. **Takaaki Noguchi:** Writing – original draft, Resources, Project administration, Data curation. **Akira Miyake:** Writing – review & editing, Writing – original draft, Visualization, Validation, Project administration, Methodology, Investigation, Funding acquisition, Formal analysis, Data curation, Conceptualization. **Kentaro Uesugi:** Software, Methodology, Formal analysis. **Akihisa Takeuchi:** Writing – original draft, Resources, Project administration, Data curation. **Shota Okumura:** Formal analysis. **Yuri Fujioka:** Formal analysis. **Mingqi Sun:** Investigation, Formal analysis. **Aki Takigawa:** Investigation, Formal analysis. **Toru Matsumoto:** Project administration. **Satomi Enju:** Formal analysis. **Itaru Mitsukawa:** Formal analysis. **Yuma Enokido:** Formal analysis. **Tatsuhiko Kawamoto:** Writing – original draft, Methodology, Investigation, Formal analysis. **Takeshi Mikouchi:** Investigation. **Tatsuhiko Michikami:** Investigation. **Tomoyo Morita:** Formal analysis. **Mizuha Kikuri:** Formal analysis. **Kana Amano:** Formal analysis. **Eiichi Kagawa:** Formal analysis. **Stefano Rubino:** Software, Funding acquisition, Formal analysis. **Zelia Dionnet:** Writing – original draft, Funding acquisition, Formal analysis. **Alice Aléon-Toppini:** Writing – original draft, Funding acquisition, Formal analysis. **Rosario Brunetto:** Writing – original draft, Resources, Funding acquisition, Formal analysis. **Michael E. Zolensky:** Writing – original draft, Funding acquisition. **Tsukasa Nakano:** Software, Methodology, Formal analysis. **Naoto Nakano:** Software. **Hisayoshi Yurimoto:** Project administration. **Ryuji Okazaki:** Project administration. **Hikaru Yabuta:** Project administration. **Hiroshi Naraoka:** Project administration, Conceptualization. **Kanako Sakamoto:** Project administration, Formal analysis. **Toru Yada:** Project administration. **Masahiro Nishimura:** Project administration. **Aiko Nakato:** Project administration, Formal analysis. **Akiko**

**Miyazaki:** Project administration. **Kasumi Yogata:** Project administration. **Masanao Abe:** Project administration. **Tatsuaki Okada:** Project administration. **Tomohiro Usui:** Project administration. **Makoto Yoshikawa:** Project administration. **Takanao Saiki:** Project administration. **Satoshi Tanaka:** Project administration. **Satoru Nakazawa:** Project administration. **Fuyuto Terui:** Writing – original draft, Resources, Project administration, Data curation. **Shogo Tachibana:** Writing – original draft, Project administration. **Sei-ichiro Watanabe:** Project administration. **Yuichi Tsuda:** Project administration.

### Declaration of competing interest

The authors declare that they have no known competing financial interests or personal relationships that could have appeared to influence the work reported in this paper.

### Acknowledgments

A. Tsuchiyama, M. Matsumoto and J. Matsuno were also supported by JSPS KAKENHI Grant Number 20H00205. A. Tsuchiyama was supported by Chinese Academy of Sciences President's International Fellowship Initiative, Grant No.2019VCA0004. J. Matsuno by JSPS KAKENHI Grant Numbers 13J01031. M. Zolensky was supported by the NASA Hayabusa2 Participating Scientist Program. S. Rubino, Z. Dionnet, A. Aléon-Toppani, and R. Brunetto were supported by CNES-France (Hayabusa2 mission). The X-nCT measurements were performed at beamtimes 2021A0166 and 2021B0188. The authors also thank Dr. Martin D. Suttle and the anonymous reviewers for their constructive comments during the review phase.

### Appendix A. Supplementary material

The supplementary material includes: (S1) Textural information in 3D by XCT compared with SEM, (S2) The relation between RID value and density and estimation of matrix density, (S3) Phase discrimination of selected objects in RGB-CT images, (S4) Phase maps and estimation modes of minerals, (S5) Textures of matrix and specific objects in matrix, (S6) Detailed texture of an object like olivine pseudomorph in C0103-FC005, (S7) Detailed texture of an fine dolomite aggregate in A0063-FC010, (S8) 3D shape features of pyrrhotite pseudo-hexagonal plates, (S9) Mineralogy of calcite- $\text{Al}_2\text{Si}_2\text{O}_5(\text{OH})_4$  aggregate as a unique sample particle in A0104-00001500, and (S10) Raman microscopy of a breunnerite grain in A0067-FC003. Supplementary material to this article can be found online at <https://doi.org/10.1016/j.gca.2024.03.032>.

### References

- Alfing, J., Patzek, M., Bischoff, A., 2019. Modal abundances of coarse-grained (>5  $\mu\text{m}$ ) components within CI-chondrites and their individual clasts – mixing of various lithologies on the CI parent body(ies). *Geochemistry* 79, 125532.
- Aquilano, D., Bruno, M., Rubbo, M., Massaro, F.R., Pastero, L., 2014. Low symmetry polymorph of hydroxyapatite: theoretical equilibrium morphology of the monoclinic  $\text{Ca}_5(\text{OH})(\text{PO}_4)_3$ . *Cryst. Growth Design* 14, 2846–2852.
- Bernard, E., Lothenbach, B., Rentsch, D., Pochard, I., Dauzères, A., 2017. Formation of magnesium silicate hydrates (M-S-H). *Phys. Chem. Earth, Parts a/b/c* 99, 142–157.
- Bland, P.A., Cressey, G., Menzies, O.N., 2004. Modal mineralogy of carbonaceous chondrites by X-ray diffraction and mössbauer spectroscopy. *Meteor. Planet. Sci.* 39, 3–16.
- Bradley, J.P., 1994. Chemically anomalous, preaccretionally irradiated grains in Interplanetary dust from comets. *Science* 265, 925–929.
- Bradley, J.P., Brownlee, D.E., Veblen, D.R., 1983. Pyroxene whiskers and platelets in interplanetary dust: evidence of vapour phase growth. *Nature* 301, 473–477.
- Brearely, A.J., 2006. The action of water. In: Lauretta, D.S., McSween, H.Y. (Eds.), *Meteorites and the Early Solar System II*. University of Arizona Press, pp. 587–624.
- Brearely A.J. and Jones R.H. (1998) "Chondritic meteorites" in *Planetary Materials* (ed. J.J. Papike), 3-01~3-398, *Reviews in Mineralogy Vol.36*. Mineralogical Society in America, Washington, D. C.
- Brunetto, R., Lantz, C., Fukuda, Y., Aléon-Toppani, A., Nakamura, T., Dionnet, Z., Baklouti, D., Borondics, F., Djouadi, Z., Rubino, S., Amano, K., Matsumoto, M., Fujioka, Y., Morita, T., Kukuiri, M., Kagawa, E., Matsuoka, M., Milliken, R., Yurimoto, H., Noguchi, T., Okazaki, R., Yabuta, H., Naraoka, H., Sakamoto, K., Tachibana, S., Yada, T., Nishimura, M., Nakato, A., Miyazaki, A., Yogata, K., Abe, M.,

- Okada, T., Usui, T., Yoshikawa, M., Saiki, T., Tanaka, S., Terui, F., Nakazawa, S., Watanabe, S., Tsuda, Y., 2023. Ryugu's anhydrous ingredients and their spectral link to primitive dust from the outer solar system. *The Astrophys. J. Lett.* 951, L33.
- Bruno, M., Massaro, F.R., Pastero, L., Costa, E., Rubbo, M., Prencipe, M., Aquilano, D., 2013. New estimates of the free energy of calcite/water interfaces for evaluating the equilibrium shape and nucleation mechanisms. *Cryst. Growth Design* 13, 1170–1179.
- Bullock, E.S., Gounelle, M., Lauretta, D.S., Grady, M.M., Russell, S.S., 2005. Mineralogy and texture of Fe-Ni sulfides in CI1 chondrites: clues to the extent of aqueous alteration on the CI1 parent body. *Geochim. Cosmochim. Acta* 69 (10), 2687–2700.
- Chan, T.F., Vese, L.A., 2001. Active contours without edges. *IEEE Trans. Image Process.* 10, 266–277.
- Chan, Q.H.S., Zolensky, M.E., Martinez, J.E., Tsuchiyama, A., Miyake, A., 2016. Magnetite plaquettes are naturally asymmetric materials in meteorites. *Am. Min.* 101, 2041–2050.
- Che, S., Brearely, A.J., 2021. The formation and alteration history of a forsterite-bearing type C CAI from allende: evidence for a type B CAI precursor, and implications for fluid-assisted metasomatism on the CV chondrite parent body. *Geochim. Cosmochim. Acta* 293, 277–307.
- Consolmagno, S.J., Britt, G.J., 1998. The density and porosity of meteorites from the vatican collection. *Meteor. Planet. Science* 33, 1231–1241.
- Delbo, M., Libourel, G., Wilkerson, J., Murdoch, N., Michel, P., Ramesh, K.T., Ganino, C., Verati, C., Marchi, S., 2014. Thermal fatigue as the origin of regolith on small asteroids. *Nature* 508 (7495), 233–236.
- Dionnet, Z., Brunetto, R., Aléon-Toppani, A., Rubino, S., Baklouti, D., Borondics, F., Buellet, A.-C., Djouadi, Z., King, A., Nakamura, T., Rotundi, A., Sandt, C., Troadec, D., Tsuchiyama, A., 2020. Combining IR and X-ray microtomography data sets: application to itokawa particles and to Paris meteorite. *Meteor. Planet. Science* 55, 1645–1664.
- Dionnet, Z., Rubino, S., Aléon-Toppani, A., Brunetto, R., Tsuchiyama, A., Lantz, C., Djouadi, Z., Baklouti, D., Nakamura, T., Borondics, F., Sandt, C., Heripre, E., Troadec, D., Mivumbi, O., Aléon, J., Ternier, T., Matsumoto, M., Amano, K., Morita, T., Yurimoto, H., Noguchi, T., Okazaki, R., Yabuta, H., Naraoka, H., Sakamoto, K., Tachibana, S., Yada, T., Nishimura, M., Nakato, A., Miyazaki, A., Yogata, K., Abe, M., Okada, T., Usui, T., Yoshikawa, M., Saiki, T., Tanaka, S., Terui, F., Nakazawa, S., Watanabe, S., Tsuda, Y., 2023. Three-dimensional multiscale assembly of phyllosilicates, organics, and carbonates in small ryugu fragments. *Meteorit. Planet. Sci.*
- Dobrică, E., Oglione, R.C., Engrand, C., Nagashima, K., Brearely, A.J., 2019. Mineralogy and oxygen isotope systematics of magnetite grains and a magnetite-dolomite assemblage in hydrated fine-grained Antarctic micrometeorites. *Meteor. Planet. Sci.* 54, 1973–1989.
- Dobrică, E., Ishii, H.A., Bradley, J.P., Ohtaki, K., Brearely, A.J., Noguchi, T., Matsumoto, T., Miyake, A., Igami, Y., Haruta, M., Saito, H., Hata, S., Seto, Y., Miyahara, M., Tomioka, N., Leroux, H., Le Guillou, C., Jacob, D., de la Peña, F., Lafort, S., Marinova, M., Langenhorst, F., Harries, D., Beck, P., Phan, T.H.V., Rebois, R., Abreu, N.M., Gray, J., Zega, T., Zanetta, P.-M., Thompson, M.S., Stroud, R., Burgess, K., Cymes, B.A., Bridges, J.C., Hicks, L., Lee, M.R., Daly, L., Blaud, P.A., Zolensky, M.E., Frank, D.R., Martinez, J., Tsuchiyama, A., Yasutake, M., Matsuno, J., Okumura, S., Mitsukawa, I., Uesugi, K., Uesugi, M., Takeuchi, A., Sun, M., Enju, S., Takigawa, A., Michikami, T., Nakamura, T., Matsumoto, M., Nakauchi, Y., Yurimoto, H., Okazaki, R., Yabuta, H., Naraoka, H., Sakamoto, K., Tachibana, S., Yada, T., Nishimura, M., Nakato, A., Miyazaki, A., Yogata, K., Abe, M., Okada, T., Usui, T., Yoshikawa, M., Saiki, T., Tanaka, S., Terui, F., Nakazawa, S., Watanabe, S.-I., Tsuda, Y., 2023. Nonequilibrium spherulitic magnetite in the ryugu samples. *Geochim. Cosmochim. Acta* 346, 65–75.
- Endreß, M., Bischoff, A., 1996. Carbonates in CI chondrites: clues to parent body evolution. *Geochim. Cosmochim. Acta* 60, 489–507.
- Fernandez, R., Moisy, C., 2020. FijiYama: a registration tool for 3D multimodal time-lapse imaging. *Bioinformatics* 37, 1482–1484.
- Frank, D.R., Huss, G.R., Zolensky, M.E., Nagashima, K., Le, L., 2023. Calcium-aluminum-rich inclusion found in the ivuna CI chondrite: are CI chondrites a good proxy for the bulk composition of the solar system? *Meteorit. Planet. Sci.* 58 (10), 1495–1511.
- Fujiya W., Kawasaki N., Nagashima K., Sakamoto N., O'D. Alexander C. M., Kita N. T., Kitajima K., Abe Y., Aléon J., Amari S., Amelin Y., Bajo K.-i., Bizzarro M., Bouvier A., Carlson R. W., Chaussidon M., Choi B.-G., Dauphas N., Davis A. M., Di Rocco T., Fukai R., Gautam I., Haba M. K., Hibiy Y., Hidaka H., Homma H., Hoppe P., Huss G. R., Ichida K., Iizuka T., Ireland T. R., Ishikawa A., Itoh S., Kleine T., Komatani S., Krot A. N., Liu M.-C., Masuda Y., McKeegan K. D., Morita M., Motomura K., Moynier F., Nakai I., Nguyen A., Nittler L., Onose M., Pack A., Park C., Piani L., Qin L., Russell S. S., Schönabächer M., Tafla L., Tang H., Terada K., Terada Y., Usui T., Wada S., Wadhwa M., Walker R. J., Yamashita K., Yin Q.-Z., Yokoyama T., Yoneda S., Young E. D., Yui H., Zhang A.-C., Nakamura T., Naraoka H., Noguchi T., Okazaki R., Sakamoto K., Yabuta H., Abe M., Miyazaki A., Nakato A., Nishimura M., Okada T., Yada T., Yogata K., Nakazawa S., Saiki T., Tanaka S., Terui F., Tsuda Y., Watanabe S.-i., Yoshikawa M., Tachibana S. and Yurimoto H. (2023) Carbonate record of temporal change in oxygen fugacity and gaseous species in asteroid Ryugu. *Nature Geosci.* 16, 675–682.
- Gounelle, M., Zolensky, M.E., 2001. A terrestrial origin for sulfate veins in CI1 chondrites. *Meteor. Planet. Sci.* 36, 1321–1329.
- Hildebrand, A.R., McCausland, P.J.A., Brown, P.G., Longstaffe, F.J., Russell, S.D.J., Tagliaferri, E., Wacker, J.F., Mazur, M.J., 2006. The fall and recovery of the tagish Lake meteorite. *Meteor. Planet. Sci.* 41, 407–431.
- Hua, X., Buseck, P.R., 1998. Unusual forms of magnetite in the orgueil carbonaceous chondrite. *Meteor. Planet. Sci.* 33, A215–A220.

- Igami, Y., Tsuchiyama, A., Yamazaki, T., Matsumoto, M., Kimura, Y., 2021. In-situ water-immersion experiments on amorphous silicates in the MgO–SiO<sub>2</sub> system: implications for the onset of aqueous alteration in primitive meteorites. *Geochim. Cosmochim. Acta* 293, 86–102.
- Ito, M., Tomioka, N., Uesugi, M., Yamaguchi, A., Shirai, N., Ohigashi, T., Liu, M.-C., Greenwood, R.C., Kimura, M., Imae, N., Uesugi, K., Nakato, A., Yogata, K., Yuzawa, H., Kodama, Y., Tsuchiyama, A., Yasutake, M., Findlay, R., Franchi, I.A., Malley, J.A., McCain, K.A., Matsuda, N., McKeegan, K.D., Hirahara, K., Takeuchi, A., Sekimoto, S., Sakurai, I., Okada, I., Karouji, Y., Arakawa, M., Fujii, A., Fujimoto, M., Hayakawa, M., Hirata, N., Hirata, N., Honda, R., Honda, C., Hosoda, S., Iijima, Y., Ikeda, H., Ishiguro, M., Ishihara, Y., Iwata, T., Kawahara, K., Kikuchi, S., Kitazato, K., Matsumoto, K., Matsuoka, M., Michikami, T., Mimasu, Y., Miura, A., Mori, O., Morota, T., Nakazawa, S., Namiki, N., Noda, H., Noguchi, R., Ogawa, N., Ogawa, K., Okada, T., Okamoto, C., Ono, G., Ozaki, M., Saiki, T., Sakatani, N., Sawada, H., Senshu, H., Shimaki, Y., Shirai, K., Sugita, S., Takei, Y., Takeuchi, H., Tanaka, S., Tatsumi, E., Terui, F., Tsukizaki, R., Wada, K., Yamada, M., Yamada, T., Yamamoto, Y., Yano, H., Yokota, Y., Yoshihara, K., Yoshikawa, M., Yoshikawa, K., Fukai, R., Furuya, S., Hatakeda, K., Hayashi, T., Hitomi, Y., Kumagai, K., Miyazaki, A., Nishimura, M., Soejima, H., Iwamae, A., Yamamoto, D., Yoshitake, M., Yada, T., Abe, M., Usui, T., Watanabe, S., Tsuda, Y., 2022. A pristine record of outer solar system materials from asteroid ryugu's returned sample. *Nature Astron.* 6, 1163–1171.
- King, A.J., Schofield, P.F., Howard, K.T., Russell, S.S., 2015. Modal mineralogy of CI and CI-like chondrites by X-ray diffraction. *Geochim. Cosmochim. Acta* 165, 148–160.
- Kita, N.T., Kitajima, K., Nagashima, K., Kawasaki, N., Sakamoto, N., Fujiya, W., Abe, Y., Aléon, J., Alexander, C.M.O'D., Amari, S., Amelin, Y., Bajo, K., Bizzarro, M., Bouvier, A., Carlson, R.W., Chaussidon, M., Choi, B.-G., Dauphas, N., Davis, A.M., Di Rocco, T., Fukai, R., Gautam, I., Haba, M.K., Hibiyu, Y., Hidaka, H., Homma, H., Hoppe, P., Huss, G.R., Ichida, K., Iizuka, T., Ireland, T.R., Ishikawa, A., Itoh, S., Kleine, T., Komatani, S., Krot, A.N., Liu, M.-C., Masuda, Y., McKeegan, K.D., Morita, M., Motomura, K., Moynier, F., Nakai, I., Nguyen, A., Nittler, L., Onose, M., Pack, A., Park, C., Piani, L., Qin, L., Russell, S.S., Schönbacher, M., Tafla, L., Tang, H., Terada, K., Terada, Y., Usui, T., Wada, S., Wadhwa, M., Walker, R.J., Yamashita, K., Yin, Q.-Z., Yokoyama, T., Yoneda, S., Young, E.D., Yui, H., Zhang, A.-C., Nakamura, T., Naraoka, H., Noguchi, T., Okazaki, R., Sakamoto, K., Yabuta, H., Abe, M., Miyazaki, A., Nakato, A., Nishimura, M., Okada, T., Yada, T., Yogata, K., Nakazawa, S., Saiki, T., Tanaka, S., Terui, F., Tsuda, Y., Watanabe, S., Yoshikawa, M., Shogo Tachibana, S., Yurimoto, H., 2024. Disequilibrium oxygen isotope distribution among aqueously altered minerals in Ryugu asteroid returned samples. Submitted to *Meteor. Planet. Sci.* <https://doi.org/10.1111/maps.14163>.
- Krot, A.N., Brearley, A.J., Petaev, M.I., Kallemeyn, G.W., Sears, D.W.G., Benoit, P.H., Hutchon, I.D., Zolensky, M.E., Keil, K., 2000. Evidence for low-temperature growth of fayalite and hedenbergite in MacAlpine Hills98107, an ungrouped carbonaceous chondrite related to the CM-CO clan. *Meteorit. Planet. Sci.* 35 (6), 1365–1386.
- Krot, A.N., Doyle, P.M., Nagashima, K., Dobricá, E., Petaev, M.I., 2022. Mineralogy, petrology, and oxygen-isotope compositions of magnetite ± fayalite assemblages in CO<sub>3</sub>, CV<sub>3</sub>, and LL<sub>3</sub> chondrites. *Meteorit. Planet. Sci.* 57 (2), 392–428.
- Kruijer, T.S., Burkhardt, C., Budde, G., Kleine, T., 2017. Age of Jupiter inferred from the distinct genetics and formation times of meteorites. *Proc. Nat. Acad. Sci.* 114, 6712–6716.
- Leshin, L.A., Rubin, A.E., McKeegan, K.D., 1997. The oxygen isotopic composition of olivine and pyroxene from CI chondrites. *Geochim. Cosmochim. Acta* 61, 835–845.
- Levison, H.F., Bottke, W.F., Gounelle, M., Morbidelli, A., Nesvorný, D., Tsiganis, K., 2009. Contamination of the asteroid belt by primordial trans-neptunian objects. *Nature* 460, 364–366.
- Longhi, J., 2005. Phase equilibria in the system CO<sub>2</sub>-H<sub>2</sub>O I: new equilibrium relations at low temperatures. *Geochim. Cosmochim. Acta* 69, 529–539.
- Marrocchi, Y., Piralla, M., Tissot, F.L.H., 2023. Iron isotope constraints on the structure of the early solar system. *The Astrophys. J. Lett.* 954, L27.
- Matsumoto, M., Tsuchiyama, A., Nakato, A., Matsuno, J., Miyake, A., Kataoka, A., Ito, M., Tomioka, N., Kodama, Y., Uesugi, K., Takeuchi, A., Nakano, T., Vaccaro, E., 2019. Discovery of fossil asteroidal ice in primitive meteorite acfer 094. *Science Adv.* 5, eaax5078.
- Matsumoto, M., Tsuchiyama, A., Miyake, A., Ito, M., Matsuno, J., Uesugi, K., Takeuchi, A., Kodama, Y., Yasutake, M., Vaccaro, E., 2022. Three-dimensional microstructure and mineralogy of a cosmic symplectite in the acfer 094 carbonaceous chondrite: implication for its origin. *Geochim. Cosmochim. Acta* 323, 220–241.
- Matsumoto, M., Matsuno, J., Tsuchiyama, A., Nakamura, T., Enokido, Y., Kikuri, M., Nakato, A., Yasutake, M., Uesugi, K., Takeuchi, A., Enju, S., Okumura, S., Mitsukawa, I., Sun, M., Miyake, A., Haruta, M., Igami, Y., Yurimoto, H., Noguchi, T., Okazaki, R., Yabuta, H., Naraoka, H., Sakamoto, K., Tachibana, S., Zolensky, M., Yada, T., Nishimura, M., Miyazaki, A., Yogata, K., Abe, M., Okada, T., Usui, T., Yoshikawa, M., Saiki, T., Tanaka, S., Terui, F., Nakazawa, S., Watanabe, S.-I., Tsuda, Y., 2024. Microstructural and chemical features of impact melts on ryugu particle surfaces: records of interplanetary dust hit on asteroid ryugu. *science*. *Advances* 10 (3), eadi7203.
- Miyazaki, A., Yada, T., Yogata, K., Hatakeda, K., Nakato, A., Nishimura, M., Nagashima, K., Kumagai, K., Hitomi, Y., Soejima, H., Tahara, R., Kanemaru, R., Nakano, A., Yoshitake, M., Iwamae, A., Furuya, S., Tsuchiyama, A., Tachibana, S., Michikami, T., Okada, T., Abe, M., Usui, T., 2023. A newly revised estimation of bulk densities and examination of the shape of individual ryugu grains. *Earth Planet. Space* 75, 171–188.
- Morlok, A., Bischoff, A., Stephan, T., Floss, C., Zinner, E., Jessberger, E.K., 2006. Brecciation and chemical heterogeneities of CI chondrites. *Geochim. Cosmochim. Acta* 70, 5371–5394.
- Mullins, W.W., Seckerka, R.F., 2004. Morphological stability of a Particle growing by diffusion or heat flow. *J. Appl. Phys.* 34, 323–329.
- Nakamura, E., Kobayashi, K., Tanaka, R., Kunihiro, T., Kitagawa, H., Potiszil, C., Ota, T., Sakaguchi, C., Yamanaka, M., Ratnayake, D.M., Tripathi, H., Kumar, R., Avramescu, M.-L., Tsuchida, H., Yachi, Y., Miura, H., Abe, M., Fukai, R., Furuya, S., Hatakeda, K., Hayashi, T., Hitomi, Y., Kumagai, K., Miyazaki, A., Nakato, A., Nishimura, M., Okada, T., Soejima, H., Sugita, S., Suzuki, A., Usui, T., Yada, T., Yamamoto, D., Yogata, K., Yoshitake, M., Arakawa, M., Fujii, A., Hayakawa, M., Hirata, N., Hirata, N., Honda, R., Honda, C., Hosoda, S., Iijima, Y.-I., Ikeda, H., Ishiguro, M., Ishihara, Y., Iwata, T., Kawahara, K., Kikuchi, S., Kitazato, K., Matsumoto, K., Matsuoka, M., Michikami, T., Mimasu, Y., Miura, A., Morota, T., Nakazawa, S., Namiki, N., Noda, H., Noguchi, R., Ogawa, N., Ogawa, K., Okamoto, C., Ono, G., Ozaki, M., Saiki, T., Sakatani, N., Sawada, H., Senshu, H., Shimaki, Y., Shirai, K., Takei, Y., Takeuchi, H., Tanaka, S., Tatsumi, E., Terui, F., Tsukizaki, R., Wada, K., Yamada, M., Yamada, T., Yamamoto, Y., Yano, H., Yokota, Y., Yoshihara, K., Yoshikawa, M., Yoshikawa, K., Fujimoto, M., Watanabe, S.-I., Tsuda, Y., 2022. On the origin and evolution of the asteroid ryugu: a comprehensive geochemical perspective. *Proc. Jap. Acad Series B* 98, 227–282.
- Nakamura, T., Matsumoto, M., Amano, K., Enokido, Y., Zolensky, M.E., Mikouchi, T., Genda, H., Tanaka, S., Zolotov, M.Y., Kurosawa, K., Wakita, S., Hyodo, R., Nagano, H., Nakashima, D., Takahashi, Y., Fujioka, Y., Kikuri, M., Kagawa, E., Matsuoka, M., Brearley, A.J., Tsuchiyama, A., Uesugi, M., Matsuno, J., Kimura, Y., Sato, M., Milliken, R.E., Tatsumi, E., Sugita, S., Hiroi, T., Kitazato, K., Brownlee, D., Joswiak, D.J., Takahashi, M., Ninomiya, K., Takahashi, T., Osawa, T., Terada, K., Brenker, F.E., Tkalcic, B.J., Vincze, L., Brunetto, R., Aléon-Toppiani, A., Chan, Q.H.S., Roskosz, M., Viennet, J.-C., Beck, P., Alp, E.E., Michikami, T., Nagaashi, Y., Tsuji, T., Ino, Y., Martinez, J., Han, J., Dolocan, A., Bodnar, R.J., Tanaka, M., Yoshida, H., Sugiyama, K., King, A.J., Fukushi, K., Suga, H., Yamashita, S., Kawai, T., Inoue, K., Nakato, A., Noguchi, T., Vilas, F., Hendrix, A.R., Jaramillo-Correa, C., Domingue, D.L., Dominguez, G., Gainsforth, Z., Engrand, C., Duprat, J., Russell, S.S., Bonato, E., Ma, C., Kawamoto, T., Wada, T., Watanabe, S., Endo, R., Enju, S., Riu, L., Rubino, S., Tack, P., Takeshita, S., Takeichi, Y., Takeuchi, A., Takigawa, A., Takir, D., Tanigaki, T., Taniguchi, A., Tsukamoto, K., Yagi, T., Yamada, S., Yamamoto, K., Yamashita, Y., Yasutake, M., Uesugi, K., Umegaki, I., Chiu, I., Ishizaki, T., Okumura, S., Palomba, E., Pílorget, C., Potin, S.M., Alasli, A., Anada, S., Araki, Y., Sakatani, N., Schultz, C., Sekizawa, O., Sitzman, S.D., Sugiura, K., Sun, M., Dartois, E., De Pauw, E., Dionnet, Z., Djouadi, Z., Falkenberg, G., Fujita, R., Fukuma, T., Gearba, I.R., Hagiya, K., Hu, M.Y., Kato, T., Kawamura, T., Kimura, M., Kubo, M.K., Langenhorst, F., Lantz, C., Lavina, B., Lindner, M., Zhao, J., Vekemans, B., Baklouti, D., Bazi, B., Borondics, F., Nagasawa, S., Nishiyama, G., Nitta, K., Mathurin, J., Matsumoto, T., Mitsukawa, I., Miura, H., Miyake, A., Miyake, Y., Yurimoto, H., Okazaki, R., Yabuta, H., Naraoka, H., Sakamoto, K., Tachibana, S., Connolly, H.C., Lauretta, D.S., Yoshitake, M., Yoshikawa, M., Yoshikawa, K., Yoshihara, K., Yokota, Y., Yogata, K., Yano, H., Yamamoto, Y., Yamamoto, D., Yamada, M., Yamada, T., Yada, T., Wada, K., Usui, T., Tsukizaki, R., Terui, F., Takeuchi, H., Takei, Y., Iwamae, A., Soejima, H., Shirai, K., Shimaki, Y., Senshu, H., Sawada, H., Saiki, T., Ozaki, M., Ono, G., Okada, T., Ogawa, N., Ogawa, K., Noguchi, R., Noda, H., Nishimura, M., Namiki, N., Nakazawa, S., Morota, T., Miyazaki, A., Miura, A., Mimasu, Y., Matsumoto, K., Kumagai, K., Kouyama, T., Kikuchi, S., Kawahara, K., Kameda, S., Iwata, T., Ishihara, Y., Ishiguro, M., Ikeda, H., Hosoda, S., Honda, R., Honda, C., Hitomi, Y., Hirata, N., Hirata, N., Hayashi, T., Hayakawa, M., Hatakeda, K., Furuya, S., Fukai, R., Fujii, A., Cho, Y., Arakawa, M., Abe, M., Watanabe, S., Tsuda, Y., 2023. Formation and evolution of carbonaceous asteroid ryugu: direct evidence from returned samples. *Science* 379, eabn8671.
- Nakano T., Tsuchiyama A., Uesugi K., Uesugi M. and Shinohara K. (2006) "Slice" -Software for basic 3-D analysis- Slice Home Page (web), <http://www-bl20.spring8.or.jp/slice/>.
- Nakashima, D., Nakamura, T., Zhang, M., Kita, N.T., Mikouchi, T., Yoshida, H., Enokido, Y., Morita, T., Kikuri, M., Amano, K., Kagawa, E., Yada, T., Nishimura, M., Nakato, A., Miyazaki, A., Yogata, K., Abe, M., Okada, T., Usui, T., Yoshikawa, M., Saiki, T., Tanaka, S., Nakazawa, S., Terui, F., Yurimoto, H., Noguchi, T., Yabuta, H., Naraoka, H., Okazaki, R., Sakamoto, K., Watanabe, S.-I., Tachibana, S., Tsuda, Y., 2023. Chondrule-like objects and Ca-al-rich inclusions in ryugu may potentially be the oldest solar system materials. *Nature Comm.* 14, 532.
- Nakato, A., Inada, S., Furuya, S., Nishimura, M., Yada, T., Abe, M., Usui, T., Yoshida, H., Mikouchi, T., Sakamoto, K., Yano, H., Miura, Y.N., Takano, Y., Yamanouchi, S., Okazaki, R., Sawada, H., Tachibana, S., 2022. Ryugu particles found outside the Hayabusa2 sample container. *Geochem. J.* 56, 197–222.
- Naraoka, H., Takano, Y., Dworkin, J.P., Oba, Y., Hamase, K., Furusho, A., Ogawa, N.O., Hashiguchi, M., Fukushima, K., Aoki, D., Schmitt-Kopplin, P., Aponte, J.C., Parker, E.T., Glavin, D.P., McLain, H.L., Elsila, J.E., Graham, H.V., Eiler, J.M., Orthous-Daunay, F.-R., Wolters, C., Isa, J., Vuitton, V., Thissen, R., Sakai, S., Yoshimura, T., Koga, T., Ohkouchi, N., Chikaraishi, Y., Sugahara, H., Mita, H., Furukawa, Y., Hertzorn, N., Ruf, A., Yurimoto, H., Nakamura, T., Noguchi, T., Okazaki, R., Yabuta, H., Sakamoto, K., Tachibana, S., Connolly, H.C., Lauretta, D.S., Abe, M., Yada, T., Nishimura, M., Yogata, K., Nakato, A., Yoshitake, M., Suzuki, A., Miyazaki, A., Furuya, S., Hatakeda, K., Soejima, H., Hitomi, Y., Kumagai, K., Usui, T., Hayashi, T., Yamamoto, D., Fukai, R., Kitazato, K., Sugita, S., Namiki, N., Arakawa, M., Ikeda, H., Ishiguro, M., Hirata, N., Wada, K., Ishihara, Y., Noguchi, R., Morota, T., Sakatani, N., Matsumoto, K., Senshu, H., Honda, R., Tatsumi, E., Yokota, Y., Honda, C., Michikami, T., Matsuoka, M., Miura, A., Noda, H., Yamada, T., Yoshihara, K., Kawahara, K., Ozaki, M., Iijima, Y.-I., Yano, H., Hayakawa, M., Iwata, T., Tsukizaki, R., Sawada, H., Hosoda, S., Ogawa, K., Okamoto, C., Hirata, N., Shirai, K., Shimaki, Y., Yamada, M., Okada, T., Yamamoto, Y., Takeuchi, H., Fujii, A., Takei, Y., Yoshikawa, K., Mimasu, Y., Ono, G.,

- Ogawa, N., Kikuchi, S., Nakazawa, S., Terui, F., Tanaka, S., Saiki, T., Yoshikawa, M., Watanabe, S., Tsuda, Y., 2023. Soluble organic molecules in samples of the carbonaceous asteroid (162173) ryugu. *Science* 379, eabn9033.
- Noguchi T., Matsumoto T., Miyake A., Igami Y., Haruta M., Saito H., Hata S., Seto Y., Miyahara M., Tomioka N., Ishii H., A., Bradley J. P., Ohtaki K. K., Dobricá E., Leroux H., Le Guillou C., Jacob D., de la Peña F., Laforet S., Marinova M., Langenhorst F., Harries D., Beck P., Phan T. H. V., Rebois R., Abreu N. M., Gray J., Zega T., Zanetta P.-M., Thompson M. S., Stroud R., Burgess K., Cymes B. A., Bridges J. C., Hicks L., Lee M. R., Daly L., Bland P. A., Zolensky M. E., Frank D. R., Martinez J., Tsuchiyama A., Yasutake M., Matsuno J., Okumura S., Mitsukawa I., Uesugi K., Uesugi M., Takeuchi A., Sun M., Enju S., Takigawa A., Michikami T., Nakamura T., Matsumoto M., Nakauchi Y., Abe M., Arakawa M., Fujii A., Hayakawa M., Hirata N., Hirata N., Honda R., Honda C., Hosoda S., Iijima Y.-i., Ikeda H., Ishiguro M., Ishihara Y., Iwata T., Kawahara K., Kikuchi S., Kitazato K., Matsumoto K., Matsuoka M., Mimasu Y., Miura A., Morota T., Nakazawa S., Namiki N., Noda H., Noguchi R., Ogawa N., Ogawa K., Okada T., Okamoto C., Ono G., Ozaki M., Saiki T., Sakatani N., Sawada H., Senshu H., Shimaki Y., Shirai K., Sugita S., Takei Y., Takeuchi H., Tanaka S., Tatsumi E., Terui F., Tsukizaki R., Wada K., Yamada M., Yamada T., Yamamoto Y., Yano H., Yokota Y., Yoshihara K., Yoshikawa M., Yoshikawa K., Fukai R., Furuya S., Hatahaka K., Hayashi T., Hitomi Y., Kumagai K., Miyazaki A., Nakato A., Nishimura M., Soejima H., Suzuki A., Usui T., Yada T., Yamamoto D., Yogata K., Yoshitake M., Connolly H. C., Lauretta D. S., Yurimoto H., Nagashima K., Kawasaki N., Sakamoto N., Okazaki R., Yabuta H., Naraoka H., Sakamoto K., Tachibana S., Watanabe S. and Tsuda Y. (2023a) A dehydrated space-weathered skin cloaking the hydrated interior of Ryugu. *Nature Astron.* 7, 170–181.
- Noguchi T., Matsumoto T., Miyake A., Igami Y., Haruta M., Saito H., Hata S., Seto Y., Miyahara M., Tomioka N., Ishii H. A., Bradley J. P., Ohtaki K. K., Dobricá E., Leroux H., Le Guillou C., Jacob D., de la Peña F., Laforet S., Mouloud B., Marinova M., Langenhorst F., Harries D., Beck P., Phan T. H. V., Rebois R., Abreu N. M., Gray J., Zega T., Zanetta P.-M., Thompson M. S., Stroud R., Burgess K., Cymes B. A., Bridges J. C., Hicks L., Lee M. R., Daly L., Bland P. A., Smith W. A., McFadzean S., Martin P.-E., Bagot P. A. J., Fougerouse D., Saxey D. W., Reddy S., Rickard W. D. A., Zolensky M. E., Frank D. R., Martinez J., Tsuchiyama A., Yasutake M., Matsuno J., Okumura S., Mitsukawa I., Uesugi K., Uesugi M., Takeuchi A., Sun M., Enju S., Takigawa A., Michikami T., Nakamura T., Matsumoto M., Nakauchi Y., Abe M., Nakazawa S., Okada T., Saiki T., Tanaka S., Terui F., Yoshikawa M., Miyazaki A., Nakato A., Nishimura M., Usui T., Yada T., Yurimoto H., Nagashima K., Kawasaki N., Sakamoto N., Hoppe P., Okazaki R., Yabuta H., Naraoka H., Sakamoto K., Tachibana S., Watanabe S., Tsuda Y. (2023b) Mineralogy and petrology of fine-grained samples recovered from the asteroid (162173) Ryugu. *Meteor. Planet. Sci.*, DOI: 10.1038/s41550-022-01841-6.
- Nozawa, J., Tsukamoto, K., van Enckevort, W., Nakamura, T., Kimura, Y., Miura, H., Satoh, H., Nagashima, K., Konoto, M., 2011. Magnetite 3D colloidal crystals formed in the early solar system 4.6 billion years ago. *J. Am. Chem. Soc.* 133, 8782–8785.
- Okazaki, R., Marty, B., Busemann, H., Hashizume, K., Gilmour, J.D., Meshik, A., et al. (2023) Noble gases and nitrogen in samples of asteroid Ryugu record its volatile sources and recent surface evolution. *Science* 379, eabo0431.
- Rietmeijer, F., Mackinnon, I., 1985. Layer silicates in a chondritic porous interplanetary dust particle. *J. Geophys. Res.* 90, D149–D155.
- Roos, C., Grangeon, S., Blanc, P., Montouillout, V., Lothenbach, B., Henocq, P., Giffaut, E., Vieillard, P., Gaboreau, S., 2015. Crystal structure of magnesium silicate hydrates (M-S-H): the relation with 2:1 Mg-Si phyllosilicates. *Cement Concrete Res.* 73, 228–237.
- Rowe, M.W., Clayton, R.N., Mayeda, T.K., 1994. Oxygen isotopes in separated components of CI and CM meteorites. *Geochim. Cosmochim. Acta* 58, 5341–5347.
- Seto, Y., Ohtsuka, M., 2022. ReciPro: free and open-source multipurpose crystallographic software integrating a crystal model database and viewer, diffraction and microscopy simulators, and diffraction data analysis tools. *J. Appl. Cryst.* 55, 397–410.
- Suttle, M.D., King, A.J., Schofield, P.F., Bates, H., Russell, S.S., 2021. The aqueous alteration of CM chondrites, a review. *Geochim. Cosmochim. Acta* 299, 219–256.
- Tachibana, S., Sawada, H., Okazaki, R., Takano, Y., Sakamoto, K., Miura, Y.N., Okamoto, C., Yano, H., Yamanouchi, S., Michel, P., Zhang, Y., Schwartz, S., Thuillet, F., Yurimoto, H., Nakamura, T., Noguchi, T., Yabuta, H., Naraoka, H., Tsuchiyama, A., Imae, N., Kurosawa, K., Nakamura, A.M., Ogawa, K., Sugita, S., Morota, T., Honda, R., Kameda, S., Tatsumi, E., Cho, Y., Yoshioka, K., Yokota, Y., Hayakawa, M., Matsuoka, M., Sakatani, N., Yamada, M., Kouyama, T., Suzuki, H., Honda, C., Yoshimitsu, T., Kubota, T., Demura, H., Yada, T., Nishimura, M., Yogata, K., Nakato, A., Yoshitake, M., Suzuki, A.L., Furuya, S., Hatahaka, K., Miyazaki, A., Kumagai, K., Okada, T., Abe, M., Usui, T., Ireland, T.R., Fujimoto, M., Yamada, T., Arakawa, M., Connolly, H.C., Fujii, A., Hasegawa, S., Hirata, N., Hirata, N., Hirose, C., Hosoda, S., Iijima, Y., Ikeda, H., Ishiguro, M., Ishihara, Y., Iwata, T., Kikuchi, S., Kitazato, K., Lauretta, D.S., Libourel, G., Marty, B., Matsumoto, K., Michikami, T., Mimasu, Y., Miura, A., Mori, O., Nakamura-Messenger, K., Namiki, N., Nguyen, A.N., Nittler, L.R., Noda, H., Noguchi, R., Ogawa, N., Ono, G., Ozaki, M., Senshu, H., Shimada, T., Shimaki, Y., Shirai, K., Soldini, S., Takahashi, T., Takei, Y., Takeuchi, H., Tsukizaki, R., Wada, K., Yamamoto, Y., Yoshikawa, K., Yumoto, K., Zolensky, M.E., Nakazawa, S., Terui, F., Tanaka, S., Saiki, T., Yoshikawa, M., Watanabe, S., Tsuda, Y., 2022. Pebbles and sand on asteroid (162173) ryugu: in situ observation and particles returned to Earth. *Science* 375, 1011–1016.
- Takeuchi, A., Uesugi, K., Suzuki, Y., 2013. Three-dimensional phase-contrast X-ray microtomography with scanning-imaging X-ray microscope optics. *J. Synchr. Rad.* 20, 793–800.
- Tomeoka, K., Buseck, P.R., 1988. Matrix mineralogy of the orgueil CI carbonaceous chondrite. *Geochim. Cosmochim. Acta* 52, 1627–1640.
- Tsuchiyama, A., Uesugi, M., Matsushima, T., Michikami, T., Kadono, T., Nakamura, T., Uesugi, K., Nakano, T., Sandford, S.A., Noguchi, R., Matsumoto, T., Matsuno, J., Nagano, T., Imai, Y., Takeuchi, A., Suzuki, Y., Ogami, T., Katagiri, J., Ebihara, M., Ireland, T.R., Kitajima, F., Nagao, K., Naraoka, H., Noguchi, T., Okazaki, R., Yurimoto, H., Zolensky, M.E., Mukai, T., Abe, M., Yada, T., Fujimura, A., Yoshikawa, M., Kawaguchi, J., 2011. Three-dimensional structure of hayabusa samples: origin and evolution of itokawa regolith. *Science* 333, 1125–1128.
- Tsuchiyama, A., Nakano, T., Uesugi, K., Uesugi, M., Takeuchi, A., Suzuki, Y., Noguchi, R., Matsumoto, T., Matsuno, J., Nagano, T., Imai, Y., Nakamura, T., Ogami, T., Noguchi, T., Abe, M., Yada, T., Fujimura, A., 2013. Analytical dual-energy microtomography: a new method for obtaining three-dimensional mineral phase images and its application to hayabusa samples. *Geochim. Cosmochim. Acta* 116, 5–16.
- Viennet, J.-C., Roskosz, M., Nakamura, T., Beck, P., Baptiste, B., Lavina, B., Alp, E.E., Hu, M.Y., Zhao, J., Gounelle, M., Brunetto, R., Yurimoto, H., Noguchi, T., Okazaki, R., Yabuta, H., Naraoka, H., Sakamoto, K., Tachibana, S., Yada, T., Nishimura, M., Nakato, A., Miyazaki, A., Yogata, K., Abe, M., Okada, T., Usui, T., Yoshikawa, M., Saiki, T., Tanaka, S., Terui, F., Nakazawa, S., Watanabe, S.-I., Tsuda, Y., 2023. Interaction between clay minerals and organics in asteroid ryugu. *Geochem. Persp. Lett.* 25, 8–12.
- Walsh, K.J., Morbidelli, A., Raymond, S.N., O'Brien, D.P., Mandell, A.M., 2012a. Populating the asteroid belt from two parent source regions due to the migration of giant planets—"The grand tack". *Meteor. Planet. Sci.* 47, 1941–1947.
- Walsh, K.J., Morbidelli, A., Raymond, S.N., Öbrien, D.P., Mandell, A.M., 2012b. Populating the asteroid belt from two parent source regions due to the migration of giant planets—"The grand tack". *Meteor. Planet. Sci.* 47, 1941–1947.
- Warren, P.H., 2011. Stable-isotopic anomalies and the accretionary assemblage of the Earth and Mars: a subordinate role for carbonaceous chondrites. *Earth Planet. Sci. Lett.* 311, 93–100.
- Yabuta, H., Cody, G.D., Engrand, C., Kebukawa, Y., De Gregorio, B., Bonal, L., Remusat, L., Stroud, R., Quirico, E., Nittler, L., Hashiguchi, M., Komatsu, M., Okumura, T., Mathurin, J., Dartois, E., Duprat, J., Takahashi, Y., Takeichi, Y., Kilcoyne, D., Yamashita, S., Dazzi, A., Deniset-Besseau, A., Sandford, S., Martins, Z., Tamenori, Y., Ohigashi, T., Suga, H., Wakabayashi, D., Verdier-Paoletti, M., Mostefaoui, S., Montagnac, G., Barosch, J., Kamide, K., Shigenaka, M., Bejach, L., Matsumoto, M., Enokido, Y., Noguchi, T., Yurimoto, H., Nakamura, T., Okazaki, R., Naraoka, H., Sakamoto, K., Connolly, H., 2023. Macromolecular organic matter in samples of the asteroid (162173) ryugu. *Science* 379, eabn9057.
- Yada, T., Abe, M., Okada, T., Nakato, A., Yogata, K., Miyazaki, A., Hatahaka, K., Kumagai, K., Nishimura, M., Hitomi, Y., Soejima, H., Yoshitake, M., Iwama, A., Furuya, S., Uesugi, M., Karouji, Y., Usui, T., Hayashi, T., Yamamoto, D., Fukai, R., Sugita, S., Cho, Y., Yumoto, K., Yabe, Y., Bibring, J.-P., Piloget, C., Hamm, V., Brunetto, R., Riu, L., Lourit, L., Loizeau, D., Lequertier, G., Moussi-Soffys, A., Tachibana, S., Sawada, H., Okazaki, R., Takano, Y., Sakamoto, K., Miura, Y.N., Yano, H., Ireland, T.R., Yamada, T., Fujimoto, M., Kitazato, K., Namiki, N., Arakawa, M., Hirata, N., Yurimoto, H., Nakamura, T., Noguchi, T., Yabuta, H., Naraoka, H., Ito, M., Nakamura, E., Uesugi, K., Kobayashi, K., Michikami, T., Kikuchi, H., Hirata, N., Ishihara, Y., Matsumoto, K., Noda, H., Noguchi, R., Shimaki, Y., Shirai, K., Ogawa, K., Wada, K., Senshu, H., Yamamoto, Y., Morota, T., Honda, R., Honda, C., Yokota, Y., Matsuoka, M., Sakatani, N., Tatsumi, E., Miura, A., Yamada, M., Fujii, A., Hirose, C., Hosoda, S., Ikeda, H., Iwata, T., Kikuchi, S., Mimasu, Y., Mori, O., Ogawa, N., Ono, G., Shimada, T., Soldini, S., Takahashi, T., Takei, Y., Takeuchi, H., Tsukizaki, R., Yoshikawa, K., Terui, F., Nakazawa, S., Tanaka, S., Saiki, T., Yoshikawa, M., Watanabe, S.-i., Tsuda, Y., 2022. Preliminary analysis of the Hayabusa2 samples returned from C-type asteroid Ryugu. *Nat. Astron.* 6 (2), 214–220.
- Yokoyama, T., Nagashima, K., Nakai, I., Young, E.D., Abe, Y., Aléon, J., Alexander, C.M. O.D., Amari, S., Amelin, Y., Bajó, K., Bizzarro, M., Bouvier, A., Carlson, R.W., Chaussidon, M., Choi, B.-G., Dauphas, N., Davis, A.M., Di Rocco, T., Fujiya, W., Fukai, R., Gautam, I., Haba, M.K., Hibiya, Y., Hidaka, H., Homma, H., Hoppe, P., Huss, G.R., Ichida, K., Iizuka, T., Ireland, T.R., Ishikawa, A., Ito, M., Itoh, S., Kawasaki, N., Kita, N.T., Kitajima, K., Kleine, T., Komatani, S., Krot, A.N., Liu, M.-C., Masuda, Y., McKeegan, K.D., Morita, M., Motomura, K., Moynier, F., Nguyen, A., Nittler, L., Onose, M., Pack, A., Park, C., Piani, L., Qin, L., Russell, S.S., Sakamoto, N., Schönbachler, M., Tafla, L., Tang, H., Terada, K., Terada, Y., Usui, T., Wada, S., Wadhwa, M., Walker, R.J., Yamashita, K., Yin, Q.-Z., Yoneda, S., Yui, H., Zhang, A.-C., Connolly, H.C., Lauretta, D.S., Nakamura, T., Naraoka, H., Noguchi, T., Okazaki, R., Sakamoto, K., Yabuta, H., Abe, M., Arakawa, M., Fujii, A., Hayakawa, M., Hirata, N., Hirata, N., Honda, R., Honda, C., Hosoda, S., Iijima, Y., Ikeda, H., Ishiguro, M., Ishihara, Y., Iwata, T., Kawahara, K., Kikuchi, S., Kitazato, K., Matsumoto, K., Matsuoka, M., Michikami, T., Mimasu, Y., Miura, A., Morota, T., Nakazawa, S., Namiki, N., Noda, H., Noguchi, R., Ogawa, N., Ogawa, K., Okada, T., Okamoto, C., Ono, G., Ozaki, M., Saiki, T., Sakatani, N., Sawada, H., Senshu, H., Shimaki, Y., Shirai, K., Sugita, S., Takei, Y., Takeuchi, H., Tanaka, S., Tatsumi, E., Terui, F., Tsuda, Y., Tsukizaki, R., Wada, K., Watanabe, S., Yamada, M., Yamada, T., Yamamoto, Y., Yano, H., Yokota, Y., Yoshihara, K., Yoshikawa, M., Yoshikawa, K., Furuya, S., Hatahaka, K., Hayashi, T., Hitomi, Y., Kumagai, K., Miyazaki, A., Nakato, A., Nishimura, M., Soejima, H., Suzuki, A., Yada, T., Yamamoto, D., Yogata, K., Yoshitake, M., Tachibana, S., Yurimoto, H., 2022. Samples returned from the asteroid ryugu are similar to ivuna-type carbonaceous meteorites. *Science* 379, eabn7850.
- Zolensky, M.E., Barrett, R.A., Browning, L., 1993. Mineralogy and composition of matrix and chondrule rims in carbonaceous chondrites. *Geochim. Cosmochim. Acta* 57, 3123–3148.